TOPOLOGY OPTIMIZATION OF ELECTRIC MOTORS BASED ON FINITE ELEMENT COMPUTATION

WU HUIHUAN

PhD

The Hong Kong Polytechnic University

2023

The Hong Kong Polytechnic University
Department of Electrical Engineering

Topology Optimization of Electric Motors Based on Finite Element Computation

Wu Huihuan

A thesis submitted in partial fulfillment of the requirements for
the degree of Doctor of Philosophy
August 2022

CERTIFICATE OF ORIGINALITY

I hereby declare that this thesis is my own work and that, to the best of my knowledge and belief, it reproduces no material previously published or written, nor material that has been accepted for the award of any other degree or diploma, except where due acknowledgment has been made in the text.

Signature: _____

Name of Student: Wu Huihuan

Abstract

Topology Optimization (TO) is a powerful tool for engineers to help them explore suitable structures. More importantly, it can find the topologies of electric motors that never existed before. This thesis work is oriented toward the TO of electric motors by developing various aspects of the subject. First, an optimization framework for TO is developed and tested. Since a complete optimization process for an electric motor requires a motor performance evaluator and an optimization algorithm working together, a coupling is done using both. Furthermore, a TO methodology is developed and tested based on the binary encoded genetic algorithm (GA) and filtering process. A well-known synchronous reluctance motor (SynRM) test case is used to accomplish the tests and validate the tools and methodology. Afterward, the methodology is applied to an asymmetric rotor interior permanent magnet (AIPM) motor, representing a more realistic test case. A high-resolution interpolation and edge-smoothing method are employed to increase modeling accuracy. An asymmetric rotor pole is presented for different problem formulations. Finally, deep learning (DL) and physics-informed generative adversarial network (PIGAN) are investigated for faster magnetic field approximation for the simulation of coaxial magnetic gear (CMG) and permanent magnet linear synchronous motor (PMLSM). These examples allow us to experience

the feasibility and efficiency of employing DL algorithms for the performance evaluation of electric motors, which can significantly benefit the optimization work.

Publications arising from the thesis

[1] **H. Wu**, S. Niu, and W. Fu, "Optimal Design of Asymmetric Rotor Pole for Interior Permanent Magnet Synchronous Motor Using Topology Optimization," Energies, vol. 15, no. 21, p. 8254, 2022.

[2] **H. Wu**, S. Niu, Y. Zhang, and W. Fu, "Physics-Informed Generative Adversarial Network-Based Modeling and Simulation of Linear Electric Machines," Applied Sciences, vol. 12, no. 20, p. 10426, 2022.

[3] **H. Wu**, S. Niu, Y. Zhang, X. Zhao, and W. Fu, "Fast Magnetic Field Approximation Method for Simulation of Coaxial Magnetic Gears using AI," *IEEE Journal of Emerging and Selected Topics in Industrial Electronics*, pp. 1–9, 2022, doi: 10.1109/JESTIE.2022.3185558.

[4] **H. Wu**, Y. Zhang, W. Fu, C. Zhang, and S. Niu, "A Novel Pre-processing Method for Neural Network-Based Magnetic Field Approximation," *IEEE Transactions on Magnetics*, 2021.

[5] Q. Lin, S. Niu, **H. Wu**, and W. Fu, "Design and Optimisation of a Bidirectional Flux Modulation Machine for AC and DC Power Supplies," *IET Renewable Power Generation*, 2021.

[6] Y. Zhang, X. Yang, **H. Wu**, D. Shao, and W. Fu, "Adaptive Degrees-of-Freedom Finite-Element Analysis of 3-D Transient Magnetic Problems," *IEEE Transactions on Magnetics*, vol. 57, no. 2, pp. 1–5, 2020.

[7] Y. Zhang, X. Liu, **H. Wu**, S.-L. Ho, and W. Fu, "3-D Transient Magneto-Thermal Field Analysis Using Adaptive Degrees-of-Freedom Finite-Element Method," *IEEE Transactions on Magnetics*, vol. 56, no. 3, pp. 1–4, 2020.

[8] Y. Zhang, S.-L. Ho, W. Fu, X. Yang, and **H. Wu**, "Numerical Study on Natural Convective Heat Transfer of Nanofluids in Disc-type Transformer Windings," *IEEE Access*, vol. 7, pp. 51267–51275, 2019.

[9] Y. Zhang, S.-L. Ho, W. Fu, X. Yang, **H. Wu**, H. Yang, and Y. Jie, "Numerical Study on Nanofluids Natural Convection Heat Transfer Inside Power Transformer Windings," *AIP Advances*, vol. 9, no. 12, p. 125343, 2019.

[10] Y. Zhang, S.-L. Ho, W. Fu, and **H. Wu**, "An Adaptive Degrees-of-Freedom Finite Element Method for 3-D Nonlinear Magneto-Thermal Field Analysis," *Numerical Heat Transfer, Part A: Applications*, vol. 75, no. 8, pp. 523–532, 2019.

Acknowledgements

My research would have been impossible without the aid and support of dozens of remarkable individuals I would like to acknowledge.

First and foremost, I would like to express my sincere gratitude to my supervisor, Dr. Shuangxia Niu, and co-supervisor, Prof. Weinong Fu, who guided me throughout this thesis. Special thanks for providing me with opportunities and freedom during my research period.

Secondly, I would like to thank all the group members, Dr. Xing Zhao, Dr. Hongjian Lin, Sigao Wang, Yuanxi Chen, Zhenghao Li, Jifu Jiang, Liang Li, and Weiyu Wang, for their valuable inspiration and suggestions.

Furthermore, I wish to acknowledge the help provided by the technical and support staff in the EE department of Hong Kong Polytechnic University.

Finally, I would like to thank my family for supporting me spiritually throughout my study and life.

Table of Contents

List of Figures

List of Tables

List of Abbreviations

Abbreviation	Full Form
2-D	2-Dimensional
3-D	3-Dimensional
AI	Artificial Intelligence
cGAN	Conditional Generative Adversarial Network
CMG	Coaxial Magnetic Gear
DL	Deep Learning
EV	Electric Vehicle
FD	Finite Difference
FE	Finite Element
GA	Genetic Algorithm
GAN	Generative Adversarial Network
IPM	Interior Permanent Magnet
MO	Multi-Objective
MG	Magnetic Gear
NN	Neural Network
NSGA	Non-dominate Sorting Genetic Algorithm
PIGAN	Physics-Informed Generative Adversarial Network
PM	Permanent Magnet

PMSM	Permanent Magnet Synchronous Motor
SIMP	Solid Isotropic Material with Penalization
SPEA	Strength Pareto Evolutionary Algorithm
TO	Topology Optimization

Chapter 1. Introduction

In recent years, developing high-performance motors has become important for realizing high-efficiency electric vehicles (EV). Electric motors need a more complex topological structure for EV to satisfy higher standards and constraints in different fields like structural stress, thermal, noise, vibration, and harshness (NVH). For this reason, topology optimization (TO) has become an efficient way for designers to explore the distribution of materials of electric motors.

This chapter begins by providing the background of this research, followed by the research objectives and contributions, and finally, an overview of the thesis.

1.1 Background

We live in an era of rapid electric vehicle (EVs) development. Electricity has become the mainstream power due to its high efficiency and controllability in transportation. The transportation industry accounts for a quarter of global carbon emissions, which has become the protagonist of a new round of electrification change [1]. Electric motors have many advantages compared to the traditional internal combustion engine (ICE). Commonly, the energy efficiency of the conventional ICE can only reach 40%.

In comparison, an electric motor can convert at least 85% of electric energy into mechanical energy, and the energy conversion process is clean and pollution-free. Moreover, compared with the complex structures of an ICE, electric motors with simple structures are also overwhelming for the manufacturing process. Power density, torque density, efficiency, reliability, production costs, and speed range make the ICE itself has no advantage over the electric motor. Furthermore, with the development of many battery-related studies [2], [3], the only shortage of electric machine energy density of the power supply will be overcome without any doubt. Therefore, various countries and regions have begun formulating relevant laws and regulations to promote EVs. For example, Europe and Japan plan to ban the sale of vehicles powered by internal combustion engines (ICEs) starting in 2035 [4], [5].

1.2 Motivation and Objective of this thesis

1.2.1 Motivations

Although the existing EVs are equipped with many high-performance motors, these motors are optimized and designed using parametric models. Restricted parameters and constraints limit these parametric motor models based on size optimization; hence the optimized solution cannot reach the limit of the design domain in terms of performance and efficiency.

On the other hand, additive manufacturing (AM) technology has become a hot topic and has much research in motor manufacturing [6]–[8]. Although additive manufacturing systems are slower and less reliable than traditional production methods, they can produce topology-optimized structures, which opens up another route for the development of the manufacture of electric motors. Therefore, the development of AM makes the topology optimization for electric motors more practical and feasible.

In this study, both algorithms and frameworks will be developed to find optimized topologies of electric motor designs. The whole system will be based on numerical tools and methods that help electrical engineers resolve complex electric motor design problems in a computationally efficient manner.

1.2.2 Aim & Objectives

The aim is to design a high-performance electric motor through topology optimization in a limited time.

The first objective is to develop a universal framework for optimizing electric motors. The performance evaluator can be based on either open-source or commercial software for solving FE numerical models. Multi-Objective Evolutionary Algorithms are selected for solving optimization problems. A coupling of both will have to be done to create an efficient optimization framework. For this purpose, a universal evolutionary optimization framework will be developed based on a scripting programming language.

The second objective is to develop an efficient methodology for topology optimization. A one-material topology optimization case will be used to evaluate the effectiveness of the proposed method.

Furthermore, the third objective is to develop a vectorized model for TO. The high-resolution vectorized model will be extended to apply the proposed optimization framework and methodology to a more complex model: an IPM motor. The new model should be composed of isotropic and anisotropic materials, thus making the optimized model easy to manufacture.

Finally, the fourth objective of this thesis is to develop an ultra-fast, physics-informed magnetic field approximation method to reduce the computing time during the simulation of electric machines; meanwhile, the nonlinear behavior is considered. A 2-D coaxial magnetic gear (CMG) and a permanent magnet linear synchronous machine (PMLSM) will be used to represent a more realistic test case and, hence, a more reasonable assessment.

1.3 Thesis Outline

The manuscript is divided into seven chapters:

Chapter 2: A state-of-the-art of the various existing TO methods is done. The technique used to complement the proposed methodology of this thesis work is justified. The conventional FE analysis, DL-based magnetic field approximation, and

optimization frameworks are elaborated, as they will further be used to compose the TO tool developed.

Chapter 3: The development of the optimization framework is introduced. A parametric and topology optimization methodology based on the existing methods is proposed. The multi-objective TO of the rotor top of the synchronous reluctance motor (SynRM) is presented using FE computation and binary-encoded multi-objective genetic algorithm. The proposed topological filter, two-stage simulation, and hand-made TO framework are verified on the SynRM model.

Chapter 4: Since the binary-encoded topology will bring jagged boundary for the optimized rotor, multi-objective TO of the asymmetric rotor of the IPM motor is investigated based on high-resolution interpolation and edge-smoothing method using FE computation. The proposed method generates vectorized CAD model, which significantly improves the edge quality. The objective functions are maximizing the torque and minimizing the torque ripple. In addition, the vectorized model makes the optimized solution easy to manufacture.

Chapter 5: The topology optimization based on genetic algorithm is time-consuming duo to the objective function evaluation method is FE computation. A novel magnetic field approximation method for electric machines using AI is proposed to reduce topology optimization's computation time. Proposed AI model verifies a coaxial

magnetic gear model with different pole-pair combinations. The approximation time of the magnetic field is 30-times faster than that of the FE method.

Chapter 6 proposes a novel magnetic field approximation method for electric machines using a physics-informed generative adversarial network (PIGAN). The magnetic field can be visually estimated and governed by Maxwell's equations. The magnetic field calculation time is significantly reduced while the accuracy is close to the FE computation.

Chapter 7 concludes the thesis, and perspectives and scopes for future works are given.

Chapter 2. Literature review

2.1 Introduction

A comprehensive overview of the state-of-art theory relating to the topics in this thesis and limitations in literature is given in this chapter. Section 2.2 provides an overview of the development of TO, while the optimization framework, as a core part of the process of TO, is discussed in Section 2.3. Finally, the numerical tools for TO are discussed in Section 2.4.

2.1.1 Optimal design of structures

A problem of optimal design (material, shape, and topology optimization) of structures is defined by three ingredients [9]:

(a) a model (typically a partial differential equation) to evaluate (or analyze) the mechanical behavior of a structure,

(b) an objective function that must be minimized or maximized, or sometimes several objectives (also called cost functions or criteria),

(c) a set of admissible designs defines the optimization variables, including possible constraints.

The kind of optimal design problems which we focus on in this thesis can be roughly divided into three categories, from the easiest to the most difficult one:

1. **Parametric or sizing optimization**, for which designs are parametrized by a few variables (for example, changing the size variables such as the cross-sectional dimensions of slots or the thicknesses of magnets.), implying that the set of admissible designs is considerably simplified. The parametric optimization changes the sizes of geometric or other properties' parameters in a candidate design. This is the easiest and earliest approach to improving structural performance. The optimization process of size optimization is shown in Fig. 2-1.

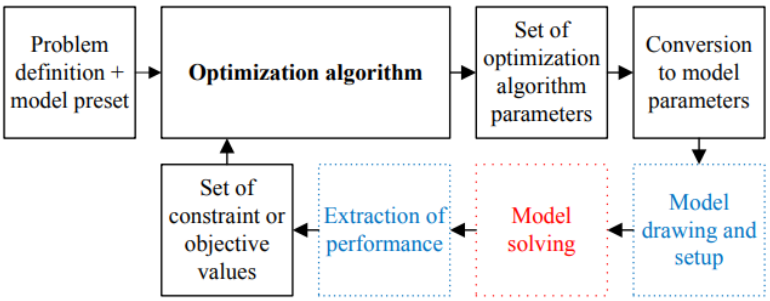

Fig. 2-1. Workflow for FEA-based size optimization.

2. **Shape optimization** is mainly performed on continuum structures by modifying the predetermined boundaries to achieve the optimal designs. For example, for a bread-shaped magnet, the location of nodes is defined as design variables. A permanent magnet synchronous motor model with bread-shape permanent magnets is shown in Fig. 2-2. The number of nodes in the boundary of the permanent magnet is twenty-two, as is shown in Fig. 2-3. The accuracy will be reduced if the number of nodes is reduced.

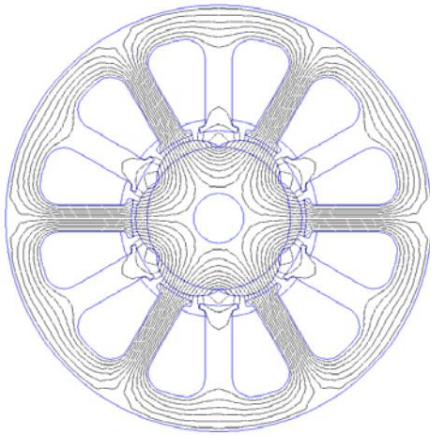

Fig. 2-2 Model of permanent magnet synchronous motor with bread shape permanent magnets

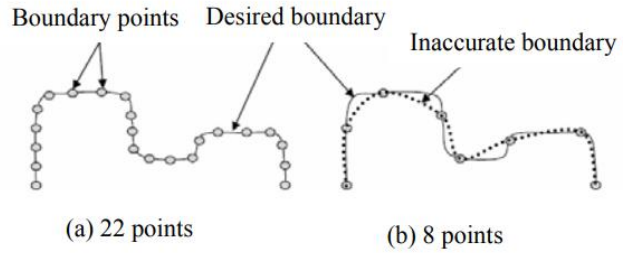

Fig. 2-3 Boundary definition of the permanent magnet.

3. **Topology optimization (TO),** where the shape and topology of the admissible designs can vary without explicit or implicit restrictions. TO for discrete structures of electric motors, such as flux barriers, is to search for the optimal spatial order and connectivity of the empty region. Fig. 2-4 demonstrates topology optimization of a synchronous reluctance motor using the density method.

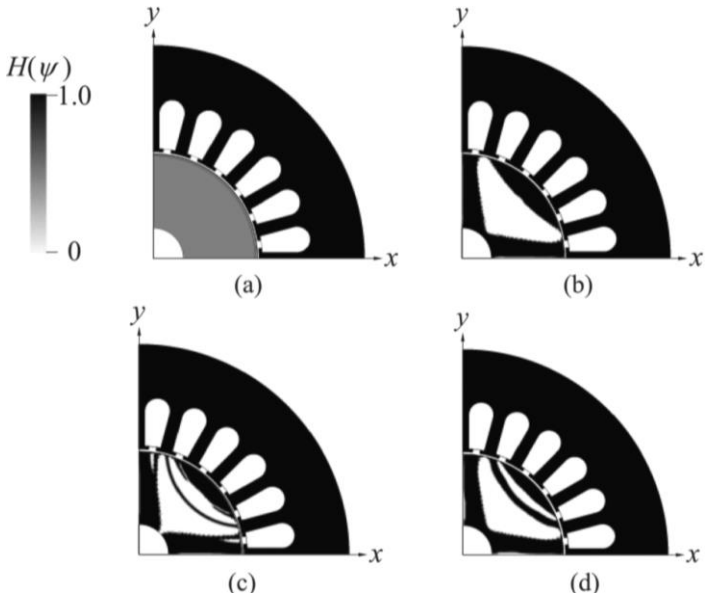

Fig. 2-4. A demonstration of topology optimization of the rotor of a synchronous reluctance motor. [10]

2.1.2 Definition of Topology

In the design process, the topology is usually considered a sub-field of geometry. The first work related to topology was the Konigsberg bridge problem proposed by Euler. This was entitled "The solution of a problem relating to the geometry of position," which indicated that the distance was irrelevant. Etymologically, the word is derived from the Greek noun "*topos"* which means location, place, space, or domain. In mathematics, topology concerns an object that can be deformed, twisted, or stretched arbitrarily. If two things have the same topology properties, they are said to be homomorphic.

Optimize a topology, i.e., to arrange materials or position structures properly and make the objective reaches its global optimal. Therefore, topology optimization differs

from shape optimization, where only the shape of the boundary or an interface of an object can be modified. It also allows for the introduction of structures, therefore, appropriately changing the topology. This work will be concerned with topology optimization.

Traditionally, it can be divided into two approaches, micro-structure topology optimization and macro-structure optimization [11], [12].

2.1.2.1 Micro-Structure

In microstructure approaches, the design domain is defined by a fixed lattice mesh. Typically, the mesh is uniformly and rectangular distributed in space, and the optimization is to determine whether the element of mesh is filled with materials or not. It is the density method if a density is applied to represent the material. If it only has a Boolean value, i.e., 0 or 1, it is the ON/OFF method [13].

2.1.2.2 Marco-Structure

Unlike the microstructure approach, the macrostructure approach does not work with a fixed finite element mesh. Instead, it changes with the variation of boundaries of the design.

Meanwhile, the topology of design can be changed by adding degenerating material or inserting specific geometric shapes in the solid body. The very beginning

work related to adding or removing material in macro-structure design was developed by Rodriguez and Seireg [14].

Another primary method of macro-structure topology optimization is to insert holes at specific points in the design domain iteratively, called the "bubble" method. It starts with a finely designed initial model for a pre-defined design domain. Then a shape optimization is applied to develop a most fitting structure within the given boundaries and constraints of variables. Detailed work was demonstrated in [13].

2.1.3 Topology for Electric Motors

For automotive traction, it seems that the IPM machine and its variations will be favored over the SPM machine in the foreseeable future due to the essential advantages of the reluctance torque. The reluctance torque generated by the IPM design also means that the rotor design is critical to machine performance. The rotor design of these machines has progressed from basic flat magnets through various configurations of U-, V-, W-shaped magnets and double V-shaped, and several others, including variations in magnet sizes from pole to pole. Fig. 2-5 shows the rotor design of IPM machines of recent production vehicles, where it can be noted, for example, the progression of the Toyota Prius from a single V in 2010 to a double V in 2017. Correspondingly, with double V and multiple Vs, the magnet volume per Nm of torque has also progressively increased. For comparison, [15] estimates that single V motors use less than 4 g/Nm versus 4 to 7 g/Nm for double Vs. Since nearly all the traction machines in surveyed in

this study use high strength rare earth magnets, this upward trend of magnet consumption is quite disconcerting.

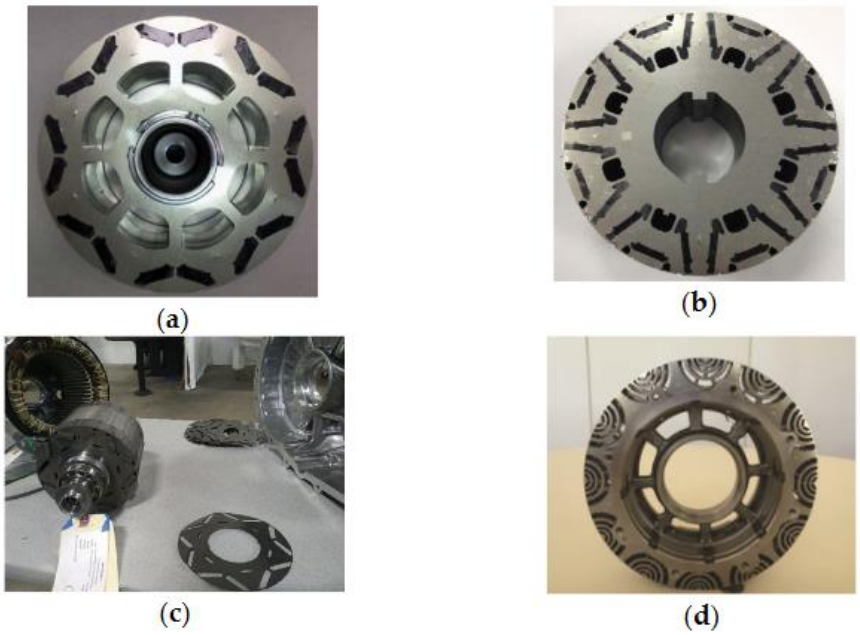

Fig. 2-5. Rotor design of the interior permanent magnet (IPM) machine of production traction motors: (a) 2010 Prius [16] V-shaped rotor; (b) 2017 Prius double U rotor [17]. (c) 2017 Tesla Model 3 IPM V rotor [18], (d) 2016 Chevy Volt IPM rotor [19].

Two important machine topologies that operate on the reluctance principle to produce torque are the synchronous reluctance (SynRM) machine and switched reluctance machine (SRM). Both machines have simple construction of a rotor composed of only thin steel laminations with no windings or magnets, the difference between the rotors being that SRM has salient pole construction. At the same time, the SynRM is typically non-salient, even though it can be designed with saliency. Fig. 2-6 shows the evolution of the SynRM over the years since its invention in the 1920s [41]. Another difference between the construction of the machines is that the stator of the

SRM is salient and wound with concentrated coils around each pole. At the same time, that of the SynRM typically has a distributed winding. SynRMs are appealing in terms of their robustness, high efficiency, low torque ripple, and simplicity (low cost) of control. These machines have only recently been commercially available for industrial applications as they are seen as a great alternative to variable speed-controlled induction machines. However, SynRMs have a disadvantage with low power factor, which affects their operational performance and the power converter sizing. Concerning automotive applications, SynRMs have been investigated for traction drive systems [27–28], with some recent prototypes built and tested for these applications [42]. For traction drives, SynRMs have relatively low CPSR.

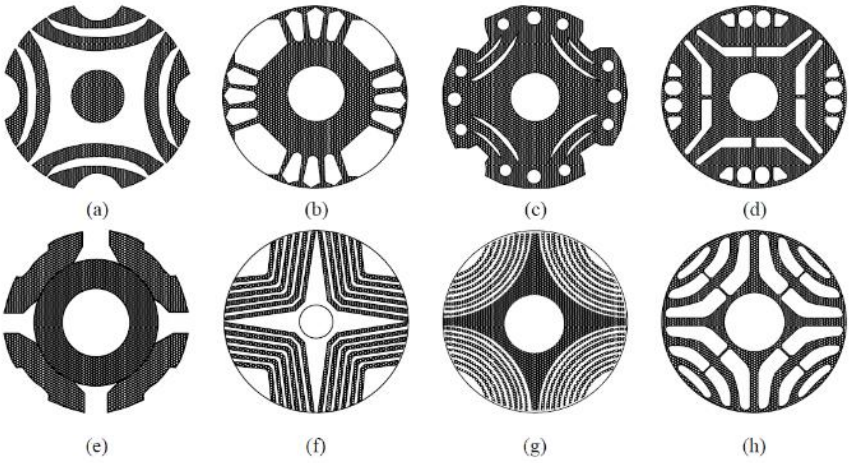

Fig. 2-6. Evolution of synchronous reluctance machines (SynRMs) showing different rotor designs [20] (a) the original Kostko rotor; (b) rotor adapted from an induction motor rotor; (c) rotor with multiple barriers; (d) rotor with saturable bridges; (e) segmented rotor; (f) axially laminated V rotor (g) axially laminated U-rotor; (h) modern transverse laminated rotor.

2.2 The Development of Topology Optimization

2.2.1 Homogenization Method

The homogenization method (HM) is the earliest topology optimization solution, first introduced in the 1980s. In 1988, Bendsøe and Kikuchi proposed a Homogenization approach based on the homogenization theory and numerical methods, which is a big step for TO [21]. After that, Bendsøe introduced the Direct approach [22] based on the HM, but more straightforward in the application and more engineer oriented.

Due to the use of structured grids in HM, and the large size of the grid, this greatly limits the number of algorithms that can be selected. Most of the work on HM uses gradient-based optimization algorithms. The more common are sequential linear programming (SLP) [23], [24], and the moving asymptote method (MMA) [25].

The HM, primarily derived for mechanical/structural designs, has been chiefly applied to the topology optimization of cantilever beams, bridges, and trusses. Its application to electromagnetic problems is quite rare and is dreaded due to a large number of variables. One of the few works presented on TO using HM was [26] in 2000. The model and optimal solution are given in Fig. 2-7

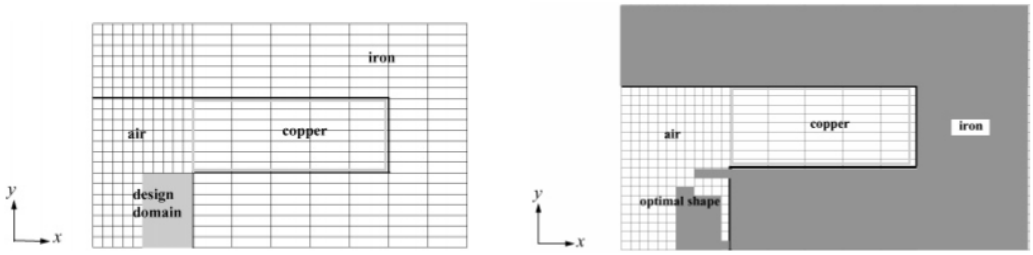

(a) (b)

Fig. 2-7. The quarter model cutting view of an H-magnet. (a) The design domain for the TO. (b) The optimal solution.[26]

Another work that proposed a novel interpolation method based on HM is presented in [27] in 2008. The authors proposed a novel interpolation method for HM to obtain more stable solutions. The optimal results show that the proposed interpolation method has improved performance compared with the previous method. The initial model and optimal solutions of this work are given in Fig. 2-8.

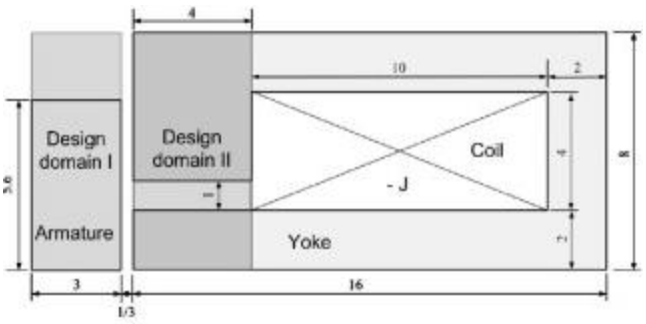

(a)

(b)

Fig. 2-8. Modified asymmetric magnetic actuator model and FEA result: (a) geometry of the initial model (unit: mm) and (b) Optimization result. [27]

2.2.2 Density-based Method

The density-based approach is derived from the homogenization approach, an essential branch in the TO for electric motors. The density-based method is mainly used for structural optimization design. Especially, Solid Anisotropic Materials with Penalty (SIMP) is a very efficient topology optimization method. The material distribution in its design domain is represented by a scalar field, the relative density of each element in the discrete domain. The magnetic permeability for the SIMP method cells is often defined as in (2-1), in which p is the penalty factor, that generally takes values between 3 and 5.

$$\mu_r = \left(\mu_{Fe}(B) - \mu_{air}(B)\right)\rho^p + \mu_{air} \qquad (2\text{-}1)$$

Where ρ = 1 means solid and ρ = 0 means the void.

Like HM, the SIMP method also uses the Moving Asymptote Method (MMA) optimizer. Its techniques are not usually combined with evolutionary algorithms because of the high computational cost associated with having multiple intermediate material states [28]. Compared to binary mesh cell densities (either 0 or 1), the consideration of intermediate material states vastly increases the complexity of the model. Therefore, SIMP approaches are generally coupled with gradient-based procedures, with adjoint variable methods [29], [30] being the most widespread, as they can significantly reduce the computation time of derivatives compared to FD or FE method.

Based on the previous works, the gradient-based optimization algorithm is the most popular optimization algorithm used with the density-based method. The method of moving asymptotes (MMAs) and its branch, the globally convergent version of MMA (GCMMA), are the most selected algorithm applied to mathematical programming owing to their faster convergence [10], [31]–[35].

The SIMP method has numerous applications in the topology optimization of electromagnetic equipment.

[33] proposes a simultaneous magnetic and structural topology optimization of a SynRM rotor using a SIMP-based method with the GCMMA. In [10], torque is enhanced by using SIMP and MMA. In [36], a structurally stable rotor is developed using the density-

based method, and a prototype is manufactured (c.f. Fig. 2-9). In [30], combined topology optimization and control are considered. The results can be found in Fig. 2-10.

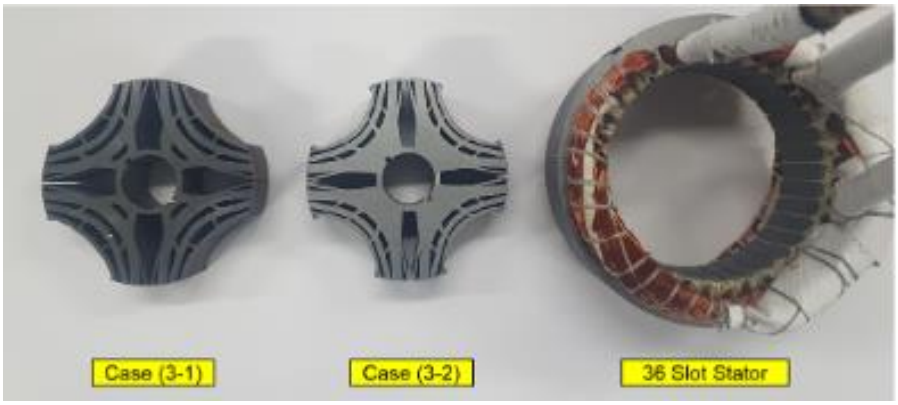

Fig. 2-9. Manufactured SynRMs considering structural stress and electromagnetic torque.

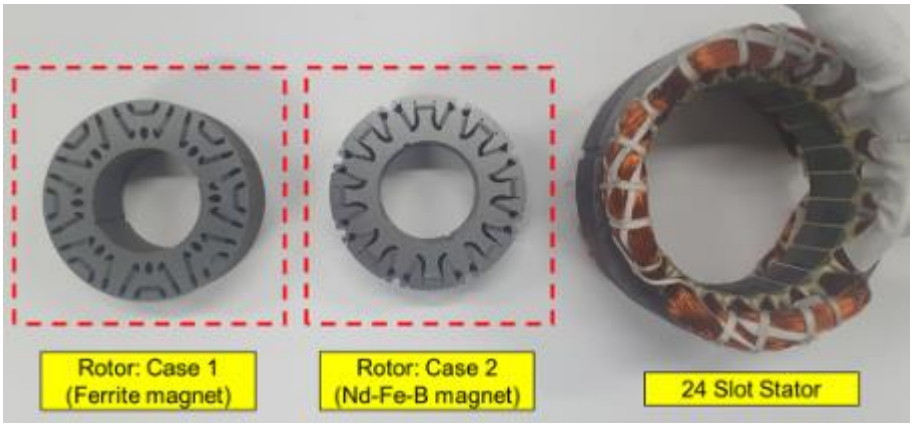

Fig. 2-10. Manufactured prototypes considering structure-safety and control strategy.

2.2.3 Level-set Method

Osher and Sethian developed the modern concept of the level-set method in 1988 [37]. The original purpose for the level-set method was to approximate the multi-phase flows [37], [38] and to segment the images [39]–[41]. The level-set method is not generally used in the optimal design of electromagnetic devices. In [42], a hybrid ON/OFF and level-set method is proposed. The authors employ a two-stage operation

during the optimization, in which the global search is performed by the ON/OFF method, and the local search is carried out by the level-set method. Fig. 2-16 shows the comparative results of the hybrid method after optimization. In [43], the shape and topology optimization of the rotor of SynRM using the adaptive level set method and the continuum sensitivity analysis is implemented. Using the adaptive level set method, the material properties are distributed clearly, and meshing is efficient. In [44], the design shape of a synchronous reluctance motor is efficiently and easily represented by the level set function. The shape sensitivity procedure is employed for the velocity field of the level set method. The results show that level set method is feasible and effective for optimal design of SynRM.

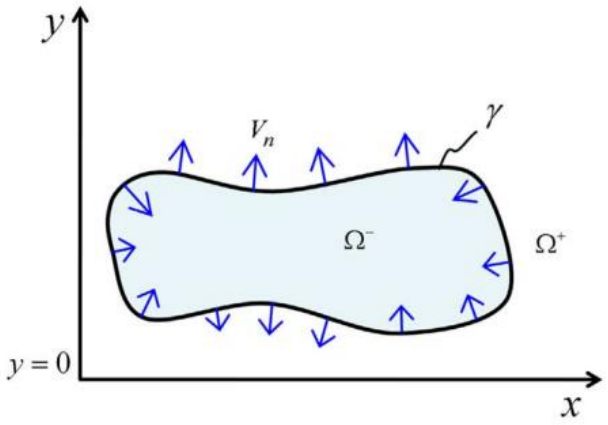

Fig. 2-11 Normal velocity field on the boundary. Its value determines the boundary shape.

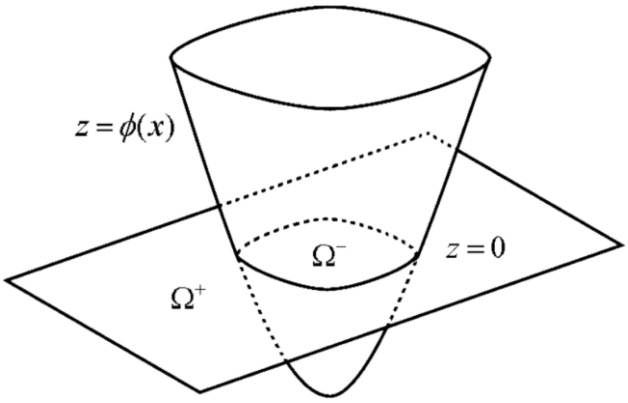

Fig. 2-12 The boundary is defined by the value of level set function $\phi(x) = 0$

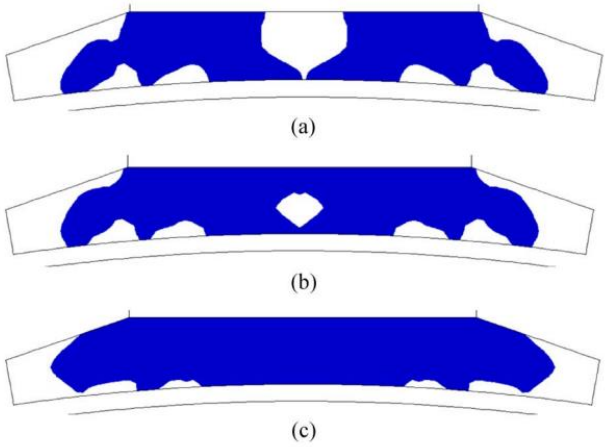

Fig. 2-13. The different solutions of stator teeth obtained by TO.

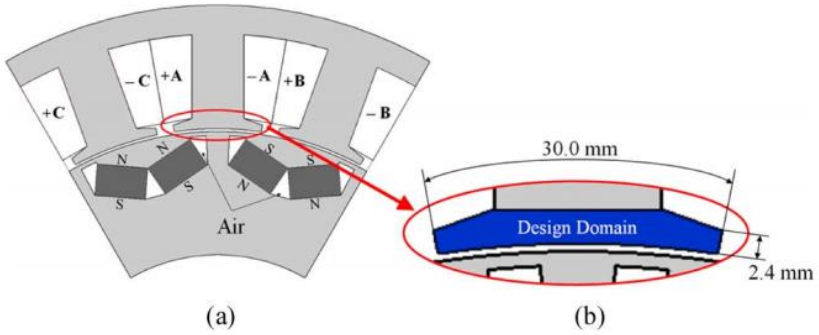

Fig. 2-14. The design domain of stator teeth for TO using level-set method.

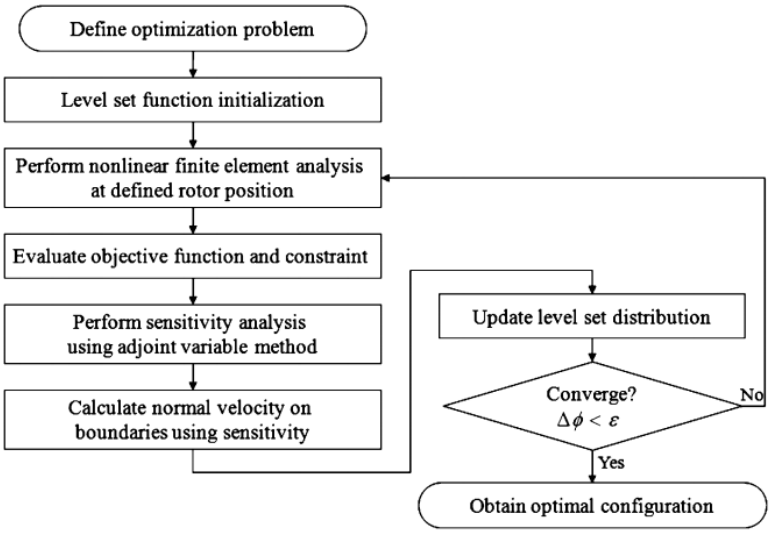

Fig. 2-15 Optimization process using the level set approach.

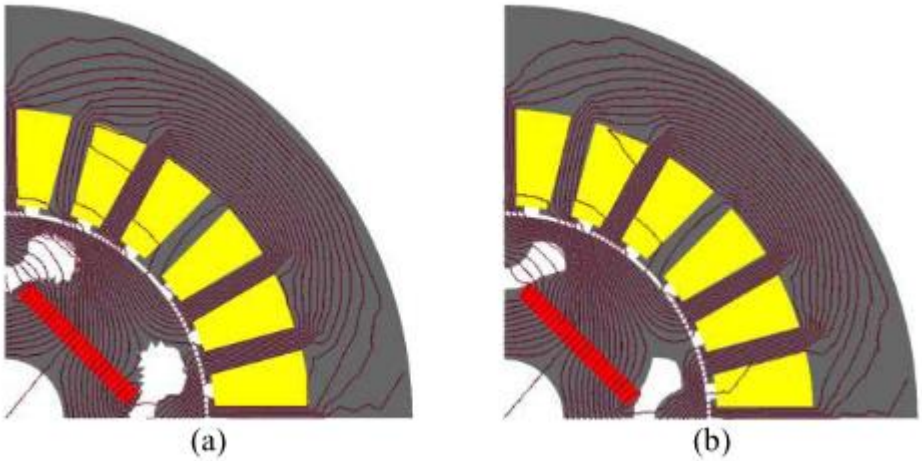

Fig. 2-16. Optimized shape using hybrid level-set method. (a) conventional ON/OFF, (b) hybrid method (ON/OFF + Level-Set method). [42]

2.2.4 ON/OFF Method

The ON/OFF method uses discretized grid in topology optimization for electromagnetic devices. However, each cell in the grid only has 0 or 1 value, while density-based methods commonly use continuous value.

Therefore, ON/OFF method can take advantage of the evolutionary algorithm in the TO process.

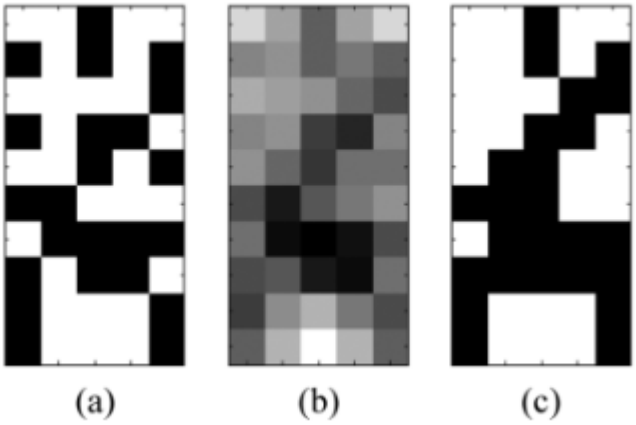

Fig. 2-17. Blurring technique for ON/OFF method. [27]

Genetic Algorithms (GA) are often used [45]–[51], and they could combine with other local search methods. In [52], the authors propose using a hybrid GA with the ON/OFF method to optimize the shape of a rotor pole to reduce the cogging torque. In [45], sensitivity analysis and GA are performed to optimize the magnetic actuator's yoke. In [53], different rotor topologies are explored using GA with the On/Off method based on the normalized Gaussian network. In [54], The ON/OFF method is extended by the unstructured mesh and immune algorithm, improving the toque performance.

2.3 Optimization Frameworks

The optimal design of electric motors is a nonlinear optimization problem. Typical objectives, such as highest efficiency, lowest cost, and minimum weight of active

materials, must be simultaneously met by a process in which the electromagnetic problem is solved considering the mechanical, thermal, and material aspects.

This section reviews the recent development of optimization algorithms and the optimal design of electric motors, mainly focusing on the search algorithm, which leads to the global optimum with minimum computational efforts.

2.3.1 Deterministic Optimization Frameworks

Deterministic optimization refers to optimization with only one scalar objective, which means the optimum set only has one solution. Many deterministic methods are applied for electric machine design optimization problems, and the gradient-based optimization framework is the most common algorithm for HM, density-based method, and LSM in TO. The most commonly used deterministic optimization algorithm in TO is MMA, which is based on MATLAB and Python [55].

2.3.2 Stochastic Optimization Frameworks

Stochastic optimization methods are procedures for maximizing or minimizing objective functions when stochastic problems are considered. Stochastic methods are not computationally efficient for TO and need more evaluations than gradient-based deterministic optimization algorithms like MMA. However, they can fully use parallel computing during optimization. The stochastic optimization framework can have lots of algorithms inside, including genetic algorithm (GA), particle swarm optimization

(PSO), simulated annealing (SA), and differential evolution. Table 2-1 lists the most popular evolutionary optimization frameworks, tools, and libraries.

Table 2-1 Evolutionary Computation Frameworks, Tools, and Libraries.

Library	**PL**	**Year**	**Algorithm**	**Description**
GALib**[56]**	C++	1996	GA	GALib was developed over UNIX operating system. The library was utilized in parallel systems and employed within distributed computing. It is built on platforms and is implemented to support distributed/parallel environments.
PISA**[57]**	C++	2003	Most EAs and simulated annealing	PISA was used to solve multi-objective problems for optimizing more than one conflicting criterion.
JMetal**[58]**	Java	2011	Many metaheuristic algorithms	Employs the object-oriented architecture, multi-objective algorithms, and parallel algorithms
Opt4J**[59]**	Java	2011	DE, PSO, and SA	It provides SPEA2 and NSGA2 multi-objective algorithms; it supports knapsack problems and has module-based implementation with GUI.
DEAP**[60]**	Python	2012	GA, GP, ES, PSO, DE	It supports parallelism and supply benchmarks which contain different test functions that could be utilized for evaluation
PyGMO and PyKEP**[61]**	Python and C++	2012	Adaptive version of differential evolution (jDE)	Support scripting for massively parallel optimization of aerospace-related problems (interplanetary trajectory optimization)
MOEA Framework**[62]**	Java	2015	MOEAs and other general-purpose MO optimization algorithms	It is extensible with custom algorithms, problems, and operators and provides tools for building and statistically testing new optimization algorithms.
Inspyred**[63]**	Python	2015	EA, swarm intelligence, and immune computing	It provides easy-to-use canonical versions of many bio-inspired algorithms for users who do not need much customization.
PlatEMO**[64]**	MATLAB	2017	MOEAs	Open-source tool supported by graphical user interface. It includes many MOEAs and test problems.

Platypus [65](our foundation)	Python	2018	MOEAs	It differs from existing optimization libraries, including PyGMO, Inspyred, and DEAP, by providing **customizable** templates for optimization algorithms and analysis tools for multi-objective optimization.

2.3.3 The framework of multi-objective optimal design

In the typical electric machine design stage, the analytical electric machine model will be designed first. If the analytical electric machine model is accurate enough, the design optimization can provide reliable parameters that can accurately predict the machine performance. However, compared with the FE model, the nonlinearity of the material leads to less accuracy in the analytical model. In addition, the increased complexity of electric machine topologies makes modeling even harder, resulting in more effort to achieve an accurate analytical model. Although the analytical electric machine model still plays an essential role in the design phase, there is a general relationship between host parameters and details of machine performance. Therefore, FE simulations are still need engineers and research to verify their final design. Due to the complexity of design optimization with multiple variables, finding an optimal design that meets the design goals is more practical.

The specifications of electric machine design are usually conflicting, for example, between high power density and low magnet volume. Highly coupled electric machine parameters affect generally the final performance of the machine at the same time. This makes it difficult to distinguish the sensitivity of parameters that leads to the design of

the electric machine that meets all the requirements. As described in (2-2) to (2-5), electric machine design usually belongs to a class of nonlinear multi-objective optimization problems with multiple constraints. [14]

Design Parameters:

$$\vec{x} = [x_1, x_2, x_3, \ldots, x_D], \vec{x} \in R^D \quad (2\text{-}2)$$

Design restrictions:

$$g_j(\vec{x}) \leq 0, j = 1,2,3,\ldots,m \quad (2\text{-}3)$$

Parameters boundaries:

$$x_i^L < x_i < x_i^U, i = 1,2,\ldots,D \quad (2\text{-}4)$$

Objective function set:

$$f(\vec{x}) = [f_1(\vec{x}), f_2(\vec{x}), \ldots, f_k(\vec{x})] \quad (2\text{-}5)$$

Duan and Ionel [66] reported that the metaheuristic methods have been widely used in optimal electric machine design, and evolutionary algorithms and simulated annealing are typical modern heuristic methods based on biological metaphors and thermodynamics correspondingly. In this project, evolutionary strategies will play an important role among these methods due to the nonlinearity of the optimization problem.

Generally, compared with the traditional gradient-based optimization method, the evolutionary method has the following differences: variables encoding rather than the variables themselves; operates on populations of solutions rather than on individual solutions; uses objective function values rather than derivatives. Nevertheless, it must be noted that the steady-state evolutionary algorithm uses random numbers when doing genetic operation, so the result cannot be repeated. Also, convergence and computational inefficiency are two main issues of evolutionary algorithms. In this proposal, a modified NSGA-II algorithm will be selected for optimization. The algorithm was initially proposed by Deb, Pratap, Agarwal, and Meyarivan [67], and modified by Durillo and Nebro[58]. It uses the Differential Evolution (DE) algorithm introduced by Storn and Price as a mutation operation, and the algorithm structure is illustrated in Fig. 2-18.

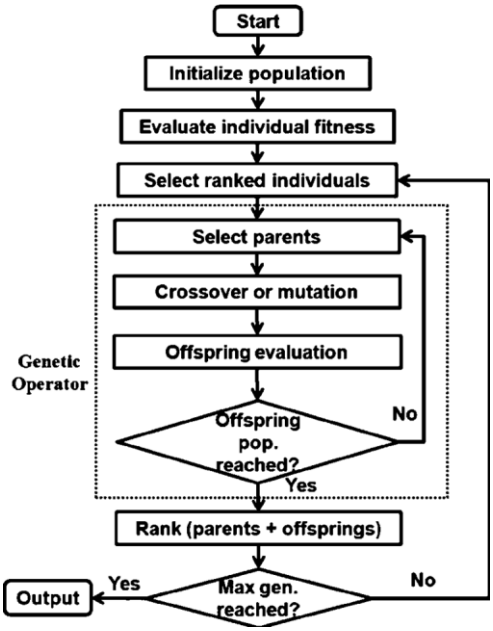

Fig. 2-18 Optimization process of NSGA-II.

Due to the complexity of the electric machine topology, it is not obvious how to locate the proper design parameters at the very beginning. Initial design of electric machines can be given by a knowledge-based electric machine design system. By generating the crossover and mutation operations in iterations, the generating set of electric machines migrates from the initial knowledge-based electric machine design system generated set to the set of solutions constrained by the user-defined limitations. The result of the optimal solutions is a group of solutions that belong to the Pareto optimal set.

2.4 Numerical Tools

Apart from the appropriate optimization method, a suitable choice of numerical tools is the key for successful TO. Faster numerical methods for magnetic fields can reduce the computational cost for traditional closed-form equations. The optimization algorithm can be of any type, i.e., local search, global search, or hybridized, and the modeling tool can be with FE, Neural Networks (NN). The FE method is usually preferred for precise modeling and accurate electromagnetic modeling and analysis results.

A lot of free and open-source FE tools and solver are available online, for example, Elmer [68], Fenics Project [69], GetDP [70], FreeFEM [71], OpenFOAM [72], deal. II [73], CalculiX [74]. Most solvers have a very long development history and can be

somewhat versatile. For example, Elmer, Fenics, and GetDP can solve multi-physics field problems. In addition, these solver libraries also support scripting languages.

In terms of commercial FE tools, Ansys Maxwell was selected as the motor topology optimization tool due to its powerful scripting system and motor performance calculation capabilities.

In addition, artificial intelligence (AI), machine learning (ML), and neural network (NN) will also be utilized to accelerate electromagnetic field analysis. These advanced technologies can significantly improve the speed of TO and make TO more valuable. The following sections briefly describe how each tool works.

2.4.1 Magnetic Field Approximation using FE Method

FE calculations are essentially based on the resolution of Maxwell's equations to solve electromagnetic problems in magnetostatic and magneto dynamic situations. Both linear and nonlinear materials can be utilized for calculations. In addition, linear translation or rotational motion can be specified for solving motor transient problems.

2.4.1.1 Boundary Conditions

Boundary conditions define the behavior of the electric or magnetic field at object interfaces or edges of the problem region (Fig. 2-12). They are always necessary to ensure the uniqueness of the electromagnetic field calculation. Different boundary conditions can be used to solve different partial differential equations. Currently,

boundary conditions include Dirichlet Boundary Condition, Neumann Boundary Condition, Robin Boundary Condition, Mixed Boundary Condition, and Cauchy Boundary Condition [75], [76].

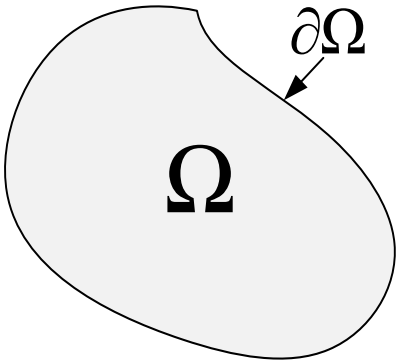

Fig. 2-19. Resolution domain and boundary

They can also be used to:

1. Simulate magnetically isolated, electrically insulated, or electrically isolated structures.

2. Set the electric or magnetic potential at a surface to a constant value or a function of position to define the behavior of the electric or magnetic field on that surface

3. Simulate the existing field patterns in a structure while modeling only part of it. To do this, you can define planes of symmetry where electric or magnetic fields are either tangential to or normal to the surface. Additionally, you can define planes of symmetry where the field on one surface matches the field's magnitude and direction (or opposite direction) on another surface.

4. Simulate the field patterns produced by thin resistive layers on conductors (DC conduction solver) or eddy currents with tiny skin depths in conductors (eddy current

solver), without explicitly drawing, assign materials to, or solve for fields inside the objects in question.

2.4.1.2 Magnetostatic Field Simulation

The magnetostatic field is conducted in this section since the eddy current is not covered in the TO of electric motors. Static magnetic fields from DC currents and other sources like permanent magnets and external magnetic fields can be computed. Magnetic fields in both linear and nonlinear materials can be simulated. The general magnetostatic field solution verifies the following two Maxwell's equations:

$$\nabla \times H = J \tag{2-6}$$

$$\nabla \cdot B = 0 \tag{2-7}$$

with the following constitutive (material) relationship being also applicable:

$$B = \mu(H + M) \tag{2-8}$$

In a 2-D problem, the magnetic vector potential, $A_z(x, y)$ in this field equation is:

$$J_z(x, y) = \nabla \times \left(\frac{1}{\mu_0 \mu_r} \left(\nabla \times A_z(x, y) \right) \right) \tag{2-9}$$

where $A_z(x, y)$ is the z component of the magnetic vector potential, $J_z(x, y)$ is the given current density field flowing in the direction of transmission, μ_r is the relative permeability of each material, μ_0 is the permeability of free space. Given $J_z(x, y)$ as

an excitation, the magnetic vector potential $A_z(x, y)$ at all points in space can be calculated. The finite element (FE) method is the most commonly used in electromagnetism for solving this PDE.

2.4.1.3 Finite Element Method

The finite element (FE) method is an advanced tool for approximating magnetic fields. It views the solution domain as consisting of many small, interconnected subdomains called finite elements, assumes a suitable (simpler) approximate solution for each unit, and then derives a solution to the problem by solving the total satisfying conditions of this domain (e.g., the equilibrium conditions of the structure).

The basic steps of finite element analysis are listed as follows.

Step 1 Pre-processing. Define the solution model according to the actual problem, including the following aspects:

(1) Define the geometric region of the problem: The physical properties and geometric region of the solution domain are approximated according to the actual problem.

(2) Defining the cell type:

(3) Define the material properties of the cell:

(4) Define the geometrical properties of the unit, such as length and area.

(5) Define the connectivity of the cell:

(6) Define the basic functions of the cell;

(7) Define the boundary conditions:

(8) Define the load.

Step 2 Assembly solution: Assembly of cells into a total matrix equation (joint system of equations) for the entire discrete domain. The assembly is performed at the nodes of adjacent cells. The continuity of state variables and their derivatives (if possible) is established at the nodes. Direct and iterative methods can do the solution of the joint system of equations. The result of the solution is an approximation of the state variables at the cell nodes.

Step 3 Post-processing: The solved solution is analyzed and evaluated according to the relevant criteria. Post-processing allows the user to extract information and understand the calculation results.

2.4.1.4 Force and Torque

The force and torque can be calculated based on Maxwell Stress Tensor Method and Virtual Work (VW) Method. In this study, the VW method is employed in FE analysis.

In the equation shown below, the force on the plate in the direction of the displacement, s, is given by the following relationship (c.f. (2-2)). The motion is performed at constant flux [77]. A similar expression can be deduced from the variations of the co-energy W' at constant current i, with the co-energy W' calculated

using integration over a volume v inside a domain D' of the induction B and the magnetic field H.

$$Fs = \frac{\partial W'}{\partial s}|i = const., \quad with\, W' = \int_{D'} \int_{0}^{h} B\, dH\, dv \qquad (2\text{-}10)$$

Different techniques can then be used to compute such forces:

The first method requires two solutions to the problem, one for each position. Then, the force can be deduced from both energy values using (2-10). Even if a very fine mesh is not needed for this method, numerical errors can appear if the displacement step (for calculating the derivate) is too high.

The second method is only to perform one computation of the problem. Given the different fields on each element, the magnetic energy is calculated for two positions of an object.

The third method involves taking an air layer surrounding an object. The nodes of the layer are then virtually displaced. The energy is calculated for each deformation.

In commercial FEM software, the VW method is performed using volume integration of 3-D meshes or surface integration of 2-D meshes.

2.4.2 Deep Learning-based Magnetic Field Approximation

Although the FE method is accurate enough for magnetic field approximation in TO, a relatively long computation time is an inevitable weakness when the number of mesh is large. In recent years, with the development of AI technology, the AI-based

field approximation offers an alternative approach to improving magnetic gears' performance. AI is commonly used for classification and regression, especially in computational visual processing. It has been gradually used for complex data fitting with the continuous development of data-driven methods [78]–[83]. Both supervised, and unsupervised learning approaches have been applied to magnetic field approximation [14], [84]–[87].

So far, a series of AI and DL concepts have been proposed, including deep neural networks with fully connected networks (FCN), convolutional networks (CNN), and generative adversarial networks (GAN) [14], [88], [89].

These preliminary results show that deep neural networks can learn the relationship between structural geometry and magnetic field distribution. Still, they also highlight critical challenges to the approach [90]. One challenge is that the computation cost of creating the training data set itself can be huge. A simple, fully connected dense network described by a few geometric parameters requires tens of thousands to hundreds of thousands of samples for training. Promising results are derived with these networks, but the training of these models relies on sufficient data, the generation of which is extremely time-consuming. In this regard, GAN-based technology can reduce the number of training samples and obtain better generalization capabilities among many neural networks [21].

Besides, deep learning (DL) has been studied extensively in the field of TO. In the field of TO for electric machines, Doi et al. investigate the capability of employing DL in the multi-objective topology optimization of rotating machines [87]. Sasaki and Igarashi developed a new topology optimization of IPM motor using GA and DL [91], [92]. Transfer learning [93] and reinforcement learning [94] are also introduced in topology optimization to reduce computing costs significantly.

In this section, the DL-based magnetic field approximation method is discussed.

2.4.2.1 Existing Physics-based Datasets

Existing physics-based datasets can be broadly classified into three categories:

1) Parameter-level models. These datasets are the parameters collected using sensors or calculated based on conventional data, including the electric motor control parameter dataset [95], [96], and electric motor temperature dataset [97].

2) Particle-level models. These datasets are usually collected by short-range depth scanners, such as FlareNet[98].

3) Field-level models. The majority of these datasets are generated explicitly for physics-based field approximation such as StreeNet [99], electromagnetic field dataset [100]–[102], and flow dataset [103], [104]

2.4.2.2 Electromagnetic Field Approximation

Recently, the development of machine learning-based field approximation shows a promising solution to this problem. Machine learning is commonly used for classification and regression, especially in computational vision processing. It has gradually been used for complex data fitting with the continuous development of data-driven methods [78]–[82], [105]. Both supervised, and unsupervised learning approaches have been applied to the magnetic field approximation [78], [84]–[86], [106]. Most studies are based on supervised training with parameters since it is very difficult to obtain more high- dimensional data, such as obtaining the 2-D or 3-D flux density distribution of a magnetic field in the real world. And if we use simulated data, it also costs considerable computation time for simulation.

So far, a series of machine learning concepts have been proposed, including deep neural networks with fully connected networks (FCN), convolutional networks (CNN), and generative adversarial networks (GAN)[78], [88], [89].

These initial demonstrations show that neural networks can learn the relationship between structural geometry and magnetic field distribution. Still, they also highlight critical challenges to the approach [90]. One challenge is that the computational cost of creating the training data set can be huge. A simple, fully connected dense network described by a few geometric parameters requires tens of thousands to hundreds of thousands of samples for training. Promising results are derived with these networks,

but the training of these models relies on sufficient data, the generation of which is exceedingly time-consuming. In this regard, GAN-based technology can reduce the number of training samples and obtain better generalization capabilities among many neural networks [85].

2.4.2.3 Force and Torque

In this study, the magnetic force and torque calculated by Python and NumPy [107] are done using the Maxwell Stress Tensor (MST) Method [108]–[111] and was implemented based on the works of [112].

In terms of MST method, the following tensor is calculated:

$$T_{ij} = \mu_0\left(H_i H_j - 1/2\delta_{ij}H^2\right) \qquad \text{with} \qquad i,j = x,y,z \tag{2-11}$$

where H is the magnetic field given by its components in the Cartesian frame (x, y, z), δ_{ij} is the Kronecker sign ($\delta_{ij} = 1$ if $i = j$ otherwise $\delta_{ij} = 0$).

For the MST method, the force can be calculated using a surface integration on surface Γ', over a domain D'. Then the force is calculated using the divergence of the MST[113]:

$$F = \int_D div\boldsymbol{T}dv = \oint_\Gamma \mu_0\left((\boldsymbol{H}\cdot\boldsymbol{n})H - 1/2|\boldsymbol{H}|^2\boldsymbol{n}\right)ds \tag{2-12}$$

where the vector $\boldsymbol{n}$ is the normal on the surface Γ'. The classical formulation detailed in (2-12) induces the permeability to be equal to the constant air permeability. So, the

force calculation has to be performed in an air region surrounding the studied part. The MST presents several advantages. Indeed, linear or nonlinear cases can be evaluated, and only the meshed part of the surface integration is concerned, which is easy to get the results from the magnetic field solution obtained by AI.

However, MST method is susceptible to the mesh quality and density of the region where the surface integration is taken. It is preferable to have enough air layers on the D' domain surrounding the parts on which the forces have to be calculated. This is particularly the case in the air-gap areas, where high field changes usually occur. It is suggested that acceptable results can be obtained with at least three air layers [111].

2.5 Summary

This chapter conducts a comprehensive review of TO, i.e., the requirement of the material distribution methods, the tools for FE modeling, and optimization. We can now proceed with tests of new methodologies and their application to electromagnetic devices to find new topologies. Table 2-2 summarizes the tools chosen from the literature review for further use.

Table 2-2. Recap of Tool and Frameworks Chosen

Tool	Choice	Main reason
FE analysis	Ansys Maxwell	Full functional FE software for electric motors with a powerful python script toolbox
Optimization Framework	Platypus	Multi-objective evolutionary

		optimization framework written in python with many powerful parallel computing libraries. Modification accessible.
Material Distribution Method	Bitmap + Level-Set	Compatible with the FE software and optimization framework.

Regarding the optimization algorithm, we will use binary-encoded NSGA-II in most cases.

A novel topology optimization framework based on evolutionary algorithms and parallel computing is presented in Chapter 3. Topology optimization of the symmetric and asymmetric rotor of a SynRM is conducted. The feasibility of the framework is verified.

Besides, the method for accelerating the speed of numerical methods using AI is presented in Chapter 5 and Chapter 6.

Chapter 3. Topology Optimization of SynRM using Bit-Array Encoded Genetic Algorithm

3.1 Introduction

In this section, an optimal synchronous reluctance motor (SynRM) design using the evolutionary approach-based topology optimization method is carried out. This study aims to design multiple flux barriers applied to the rotor to reduce the torque ripple. A multi-objective optimization framework for electric motors to obtain a possible topology is presented. In general, the TO using gradient algorithms with material optimization like the ON/OFF method often produces complex shapes that are very hard to create in prototyping. In addition, lattice meshes were required for the ON/OFF method.

For this reason, it results in poor expression ability for curved surfaces and restriction of mesh generation and increases the algorithm's complexity. To solve this problem, the optimization algorithm uses steps in a polar coordination system instead of meshes in a rectangular coordination system. The present method is applied to concurrent structural and material optimization of synchronous motors, and optimization results show that feasible shapes are obtained, and two objective functions (torque and torque ripple property) are improved.

3.2 Optimization Framework

3.2.1 The Architecture of Scalable Multi-Objective Genetic Algorithm Framework

Population-based metaheuristic optimization for multi-objective optimization problems (MOPs), such as Non-dominated Sorting Genetic Algorithm II (NSGA-II) and strength Pareto evolutionary algorithm (SPEA2), has been widely practiced in design optimization [114], [115]. However, the limitation of computational resources in the local host prevents these algorithms from working as efficiently as expected. The computational time highly relies on the performance of local computers when doing the evaluation process, and the actual time consumption can be far more than expected because sometimes designs have errors, and solutions cannot be obtained.

In this section, an efficient, robust, and scalable multi-objective genetic algorithm framework for a cloud computing environment is proposed for searching the solution of electromagnetic device design.

Three levels, consisting of GA Manager, Task Manager, and Resource Allocator, are designed in this framework to achieve robustness, scalability, and efficiency. Each module is interconnected, as described in Fig. 3-1.

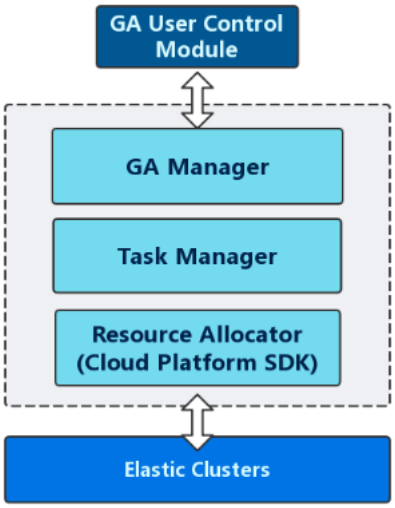

Fig. 3-1. Architecture of proposed GA Framework.

3.2.2 On-Demand Computing Resource Allocation

Benefitting from the development of virtualization technology, cloud computing can bring great convenience and advantages in electromagnetic device design optimization. While evaluating the performance of an electromagnetic device, some models may have errors, such as intersection, and lead FE solver stops unexpectedly. In this case, no valid solution can be obtained. A checking algorithm is proposed to validate the solution. If the checking algorithm finds any abnormal solution, a new task with a new design will be added to the task queue to repeat the evaluation process. For the traditional architecture of the local computing environment, when a new task is added, not all CPU cores can be fully used. The unused computing resources will be wasted waiting for the newly added task to finish. However, cloud computing has taken advantage of the efficiency and agility realized by virtualization. In a cloud computing

environment, the idle clusters can be released through the API command; hence costs can be reduced when evaluating the newly added task.

3.3 Methodology for Topology Optimization

Checkerboard is an unstable structure in topology optimization; therefore, filter or smooth operators are introduced to reduce these structures, especially in the boundary design. Fig. 3-2 shows a typical checkerboard structure.

Filters are inspired by image-processing approaches. The filter can be formulated as follows:

$$\Psi(x) = F \times G = \int_{R^2} F(x)G(x-y)dy \qquad (3\text{-}1)$$

where G satisfies the law of energy conservation.

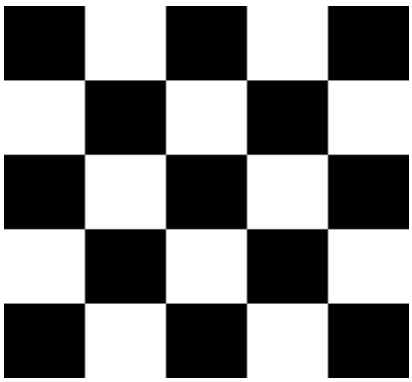

Fig. 3-2 Example of Checkerboard

In this study, a Gaussian filter is applied. The Gaussian filter is an image-blurring filter that uses a Gaussian function (which also expresses the normal distribution in

statistics, c.f. (3-2)) for calculating the transformation to apply to each pixel in the image.

$$G(x,y) = \frac{1}{2\pi\sigma^2} e^{-\frac{x^2+y^2}{2\sigma^2}} \qquad (3\text{-}2)$$

Fig. 3-3 in the following indicates a sample matrix produced by sampling the Gaussian filter kernel (with σ = 1) at the midpoints of each pixel and then normalizing. Note that the center element (at [2, 2]) has the biggest value, decreasing symmetrically from the center.

	0	1	2	3	4
0	0.0029690167439504977	0.013306209891013656	0.021938231279714646	0.013306209891013656	0.0029690167439504977
1	0.013306209891013656	0.05963429543618016	0.0983203313488458	0.05963429543618016	0.013306209891013656
2	0.021938231279714646	0.0983203313488458	0.1621028216371267	0.0983203313488458	0.021938231279714646
3	0.013306209891013656	0.05963429543618016	0.0983203313488458	0.05963429543618016	0.013306209891013656
4	0.0029690167439504977	0.013306209891013656	0.021938231279714646	0.013306209891013656	0.0029690167439504977

Fig. 3-3 The 5*5 Gaussian filter kernel.

Fig. 3-4 shows how the filter works and the influence of filtering on encoded topology data. The number of checkerboard structures is filtered significantly, and they gradually form several holes in the topology as the number of filtering increases.

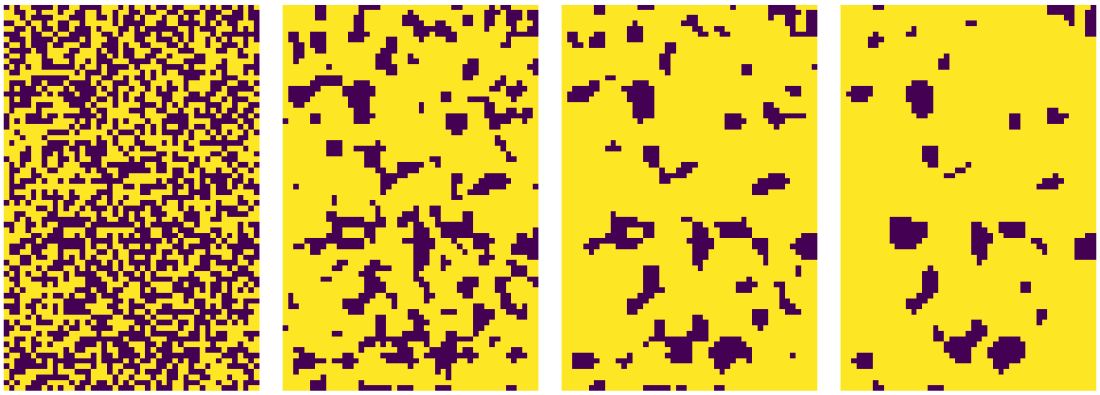

(a) (b) (c) (d)

Fig. 3-4 Unfiltered and filtered encoded data. (a) is unfiltered encoded data, (b) is filtered once, (c) is filtered twice, (d) is filtered three times.

3.4 Experiments and Results

Two case study are investigated to realize the proposed topology optimization techniques.

Fig. 3-5 shows the optimization model of the Synchronous Reluctance Motor. The motor consists of twenty-four slots and four poles. There are two layers in each slot, and the coil pitch is one. Three-phase current source $\mathrm{i_u(t)}$, $\mathrm{i_v(t)}$ and $\mathrm{i_w(t)}$ are applied to the coils, they are defined as follows:

$$i_u(t) = I_m sin(\omega t + \pi/4) \quad (3\text{-}3)$$

$$i_v(t) = I_m sin(\omega t - 2\pi/3 + \pi/4) \quad (3\text{-}4)$$

$$i_w(t) = I_m sin(\omega t - 4\pi/3 + \pi/4) \quad (3\text{-}5)$$

where I_m is the maximum amplitude of the input current (10A * 26 turns), the rotor works at the rated speed of 3600 rpm, and the current phase angle is fixed as $+\pi/4$ when working at the rated speed.

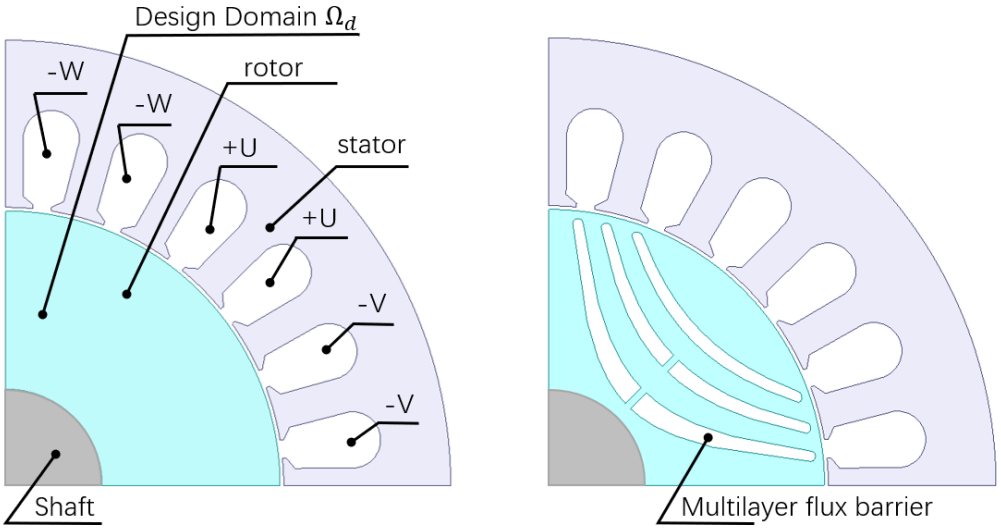

(a) (b)

Fig. 3-5 Synchronous Reluctance Motor Model. (a) Optimization model. (b) Reference Model.

The control circuit is not considered in topology optimization because the magnetic source is derived from the current source. The nonlinear material of stator and rotor is M19-29G, one of the most prevalent silicon steels. The mechanical rotating pitch of the rotor is 7.5 degrees, and the rotation of a 30-degree mechanical angle evaluates the torque. The air gap length is set to 0.5 mm, and the air gap region is not included in the design domain for topology optimization. The analysis region is spatially discretized into quadrilateral first-order elements. The number of elements is 3337 (23*71).

Table 3-1. Specification of reluctance motor

Property	**Value**
Number of Slots	24
Number of Poles	4

Type	Reluctance Motor
Design Domain Materials	Iron or Air
Speed	3600 RPM
Air Gap Length	0.5 mm
Excitation Source	Ideal Current Source

The design goal is to improve the average torque and minimize the torque ripple. Hence, the optimization problem can be formulated as follows:

$$\left.\begin{aligned} &\min_{\rho} : F = F(\mathbf{u}(\rho), \rho) = \int_{\Omega} f(\mathbf{u}(\rho), \rho) dV \\ &s.t. : G_{0(\rho)} = \int_{\Omega} \rho(\mathbf{x}) dV - V_0 \leq 0 \\ &\quad : G_j(\mathbf{u}(\rho), \rho) \leq 0, j = 1, \ldots, M \\ &\quad : \rho(\mathbf{x}) = 0 \; or \; 1, \forall \, \mathbf{x} \in \Omega \end{aligned}\right\} \quad (3\text{-}6)$$

The two objective functions are defined as

$$\begin{cases} \mathrm{F}_1 = -\mathrm{T}_\mathrm{a} \\ \mathrm{F}_2 = \mathrm{T}_\mathrm{max} - \mathrm{T}_\mathrm{avg} \end{cases} \quad (3\text{-}7)$$

where T_a is the average torque, T_max is the maximum Torque and T_avg is the average torque. The torque-time curve is evaluated by the FE software using the VW method.

3.4.1 Case of Design Domain with Symmetric Rotor Part

Three-phase current source $\mathrm{i}_\mathrm{u}(\mathrm{t})$, $\mathrm{i}_\mathrm{v}(\mathrm{t})$ and $\mathrm{i}_\mathrm{w}(\mathrm{t})$ is applied to the coils. The structure of the rotor is shown in Fig. 3-6. The size of the rotor is equivalent to the symmetric rotor, but the degree of freedom was increased. The total mesh number is 1633, as shown in Fig. 3-6. In addition, a mirror operation is adopted in drawing the topology process, as shown in Fig. 3-6(a). The winding layout is slightly changed

from an asymmetric position to a symmetric position. This modification makes the topology symmetric.

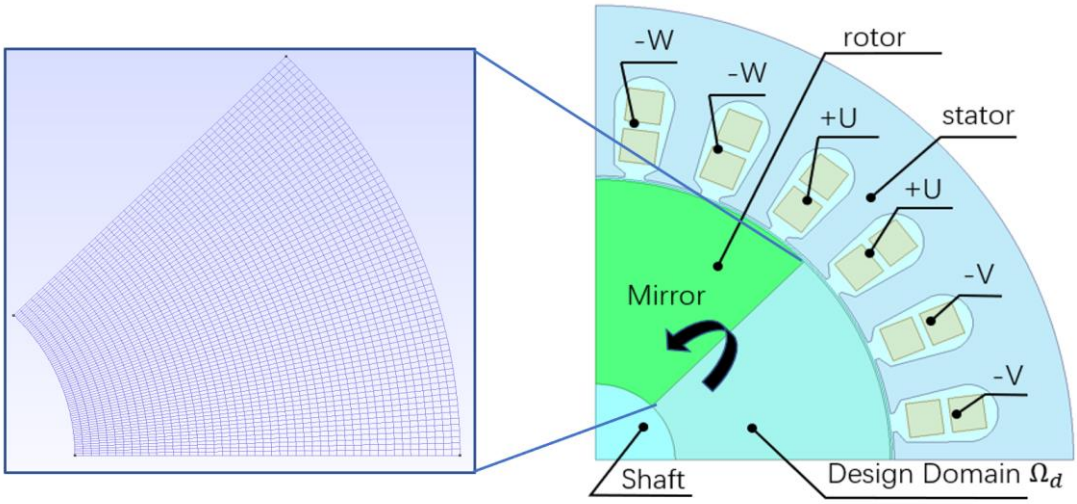

(a) (b)

Fig. 3-6 (a) is the mesh structure in the design domain and (b) is the winding layout of symmetric rotor SynRM.

The total evaluation number is 4000, and it costs 20 hours to obtain the solution set after 100 iterations. The results show that the non-gradient evolutionary algorithm is practical without sensitivity calculation. However, the efficiency of ES is relatively low compared with other works. For example, a SIMP-based optimization process of similar size SynRM only costs around 12 to 17 hours. The efficiency of the proposed algorithm should be improved in the future.

Fig. 3-7 is the Pareto-front of the optimization, and an optimized solution from the turning point of the Pareto-front is selected.

Table 3-2 lists the torque and ripple comparison between the selected optimized model and the reference model. The optimized rotor forms a salient pole (c.f. Fig. 3-8

and Fig. 3-9), and flux line distribution is getting close to the reference model, as shown in Fig. 3-10. However, the jagged edge in the rotor could introduce more harmonics in the flux density in the air gap, which enlarges the detent torque.

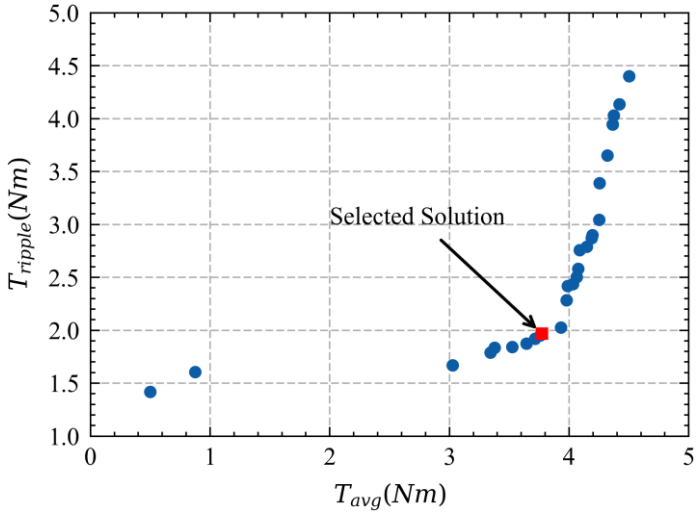

Fig. 3-7 Pareto Front of Solution of Symmetric Rotor

Table 3-2 Optimization Results with Symmetric Rotor Part

Model	**T_a[Nm]**	**T_r[Nm]**	**Elapsed time[h]**
Reference	6.44	0.48	-
Symmetric Rotor	3.77	1.97	8

CPU: AMD Ryzen 1700X @ 3.4GHz & 32GB Memory

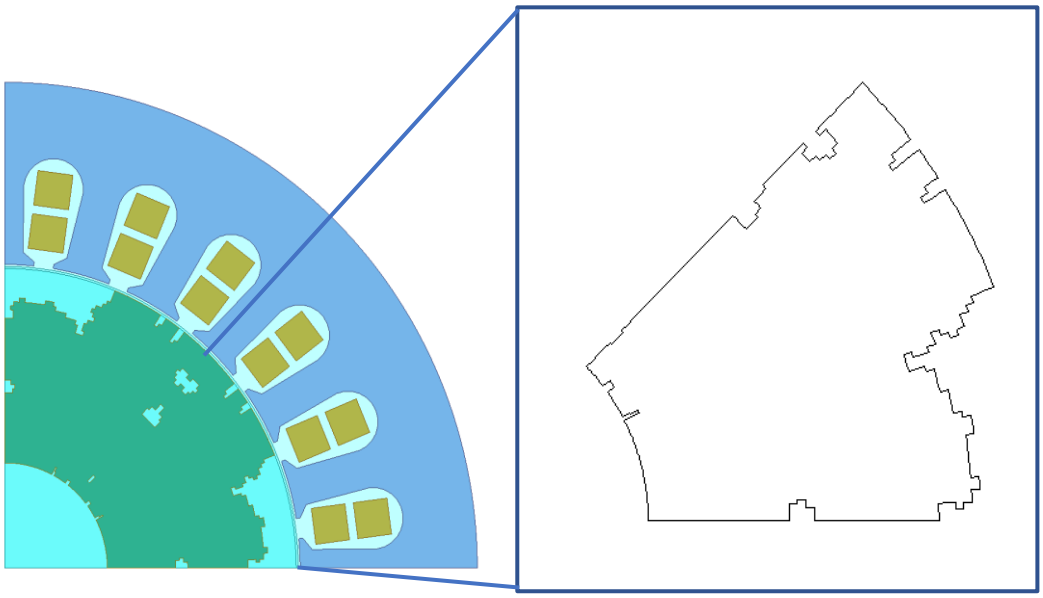

Fig. 3-8 Encoded Topology of symmetrical rotor pole.

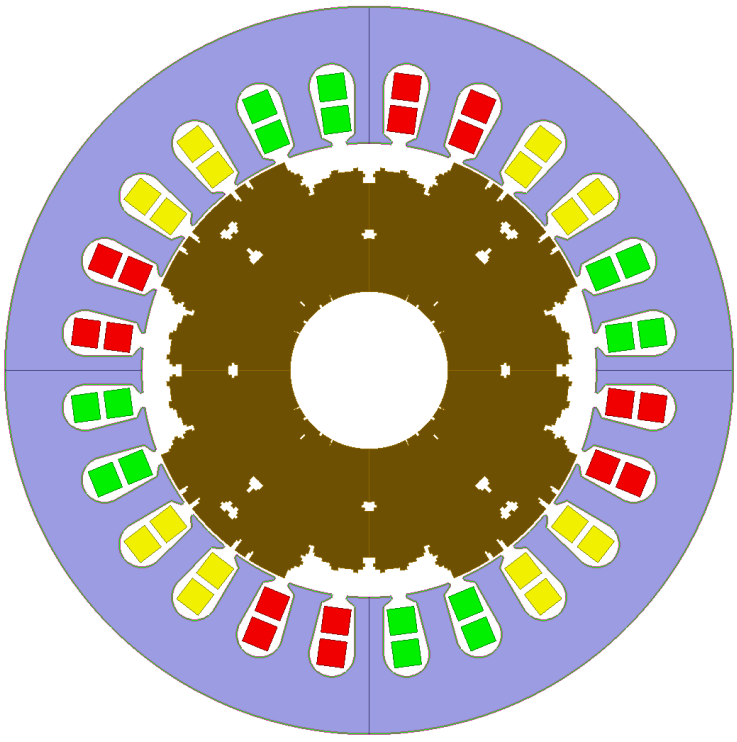

Fig. 3-9 Full model and winding layout of symmetric rotor pole.

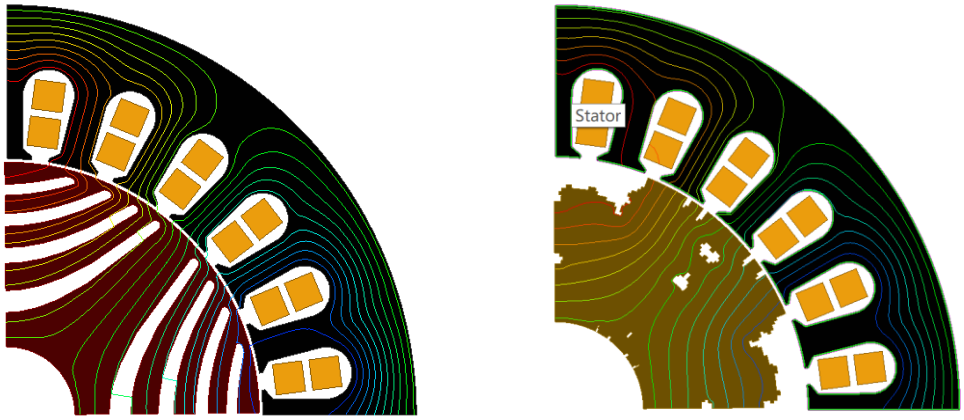

(a) (b)

Fig. 3-10 Flux line distribution. (a) is the reference model, and (b) is the optimized symmetric rotor model.

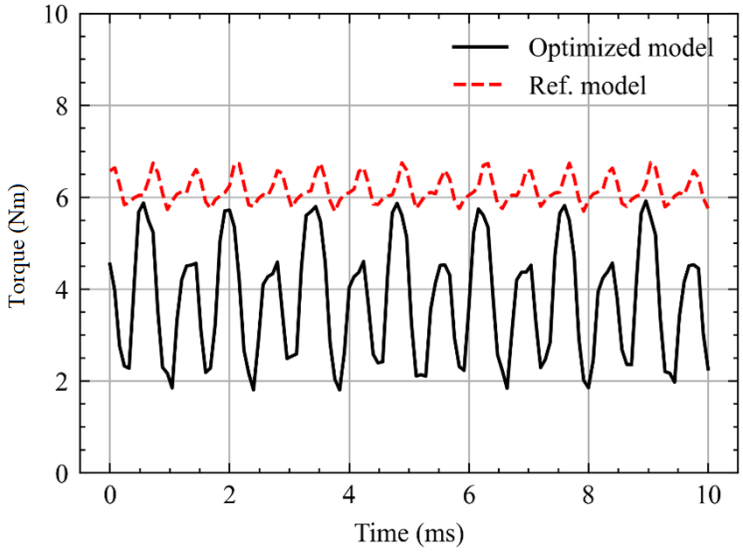

Fig. 3-11 Torque characteristics derived from the design domain with symmetric rotor part.

3.4.2 Case of Design Domain with Asymmetric Rotor Part

The asymmetric synchronous reluctance motor is presented in this section. The design domain is shown in Fig. 3-12. The total number of evaluations is 6000, and the iteration number k_{opt} is 200. The optimization time consumption is 25 hours.

Fig. 3-13 is the Pareto-front of the results obtained from TO of asymmetric SynRM, and an optimized solution from the turning point of the Pareto-front is selected.

Compared with the reference model, the optimized model forms a 4-pole structure, and it has a similar torque and torque ripple value to the reference model, while the topology is different. Moreover, the resolution of structure is relatively low in the design domain Ω_d, as is shown in Fig. 3-14 and Fig. 3-15.

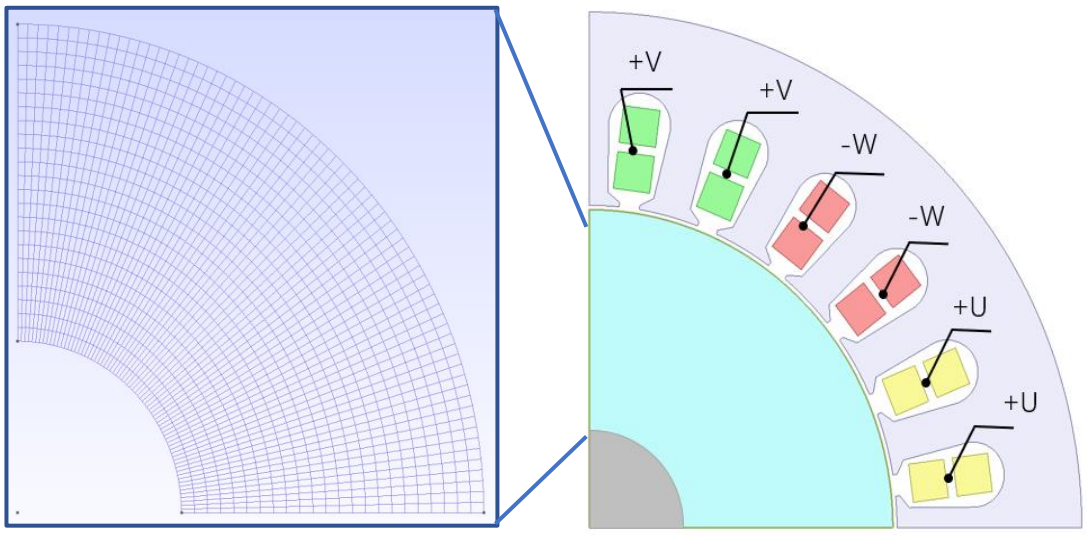

Fig. 3-12 Design domain and winding configuration of a 24-slot 4-pole asymmetric rotor IPM motor.

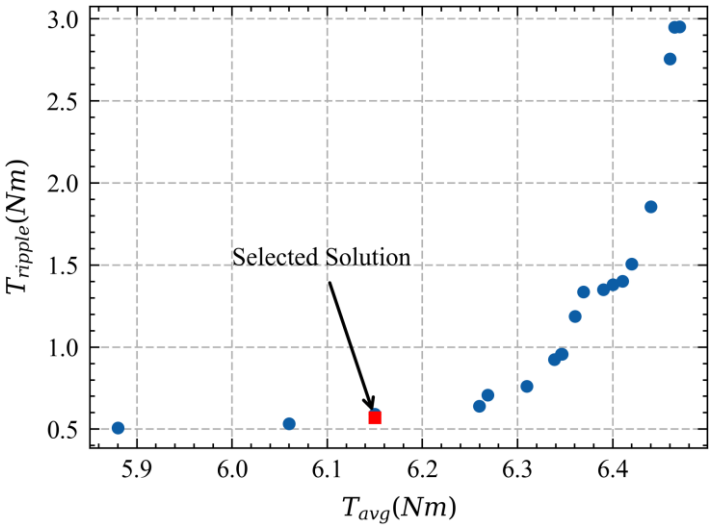

Fig. 3-13 Pareto Front of Solution of asymmetric SynRM.

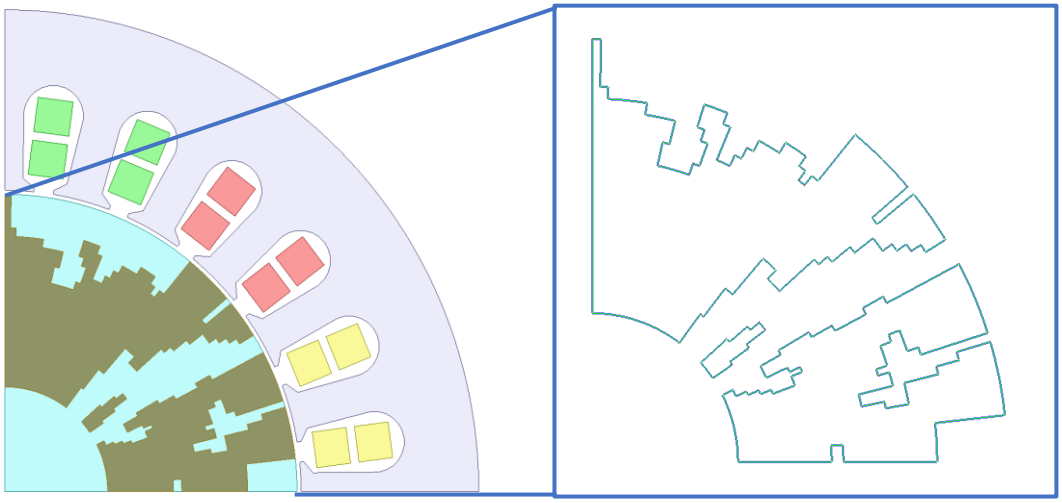

Fig. 3-14 Encoded Topology of the optimal solution of AIPM motor.

Table 3-3 Optimization Results with Asymmetric Rotor Part

Model	$\mathbf{T_a}[Nm]$	$\mathbf{T_r}[Nm]$	**Elapsed time[h]**
Reference	6.17	0.48	-
Asymmetric Rotor	6.15	0.57	25

CPU: AMD Ryzen 1700X @ 3.4GHz & 32GB Memory

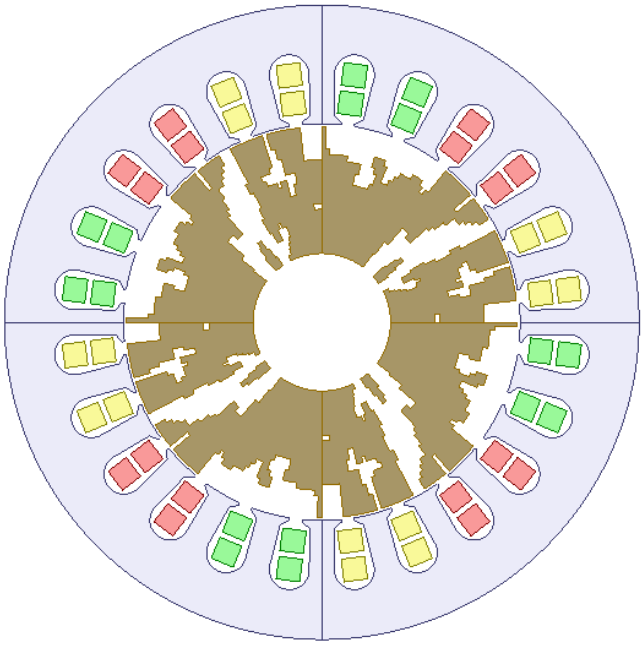

Fig. 3-15 Full structure and winding layout of the asymmetric rotor (Minimum torque ripple)

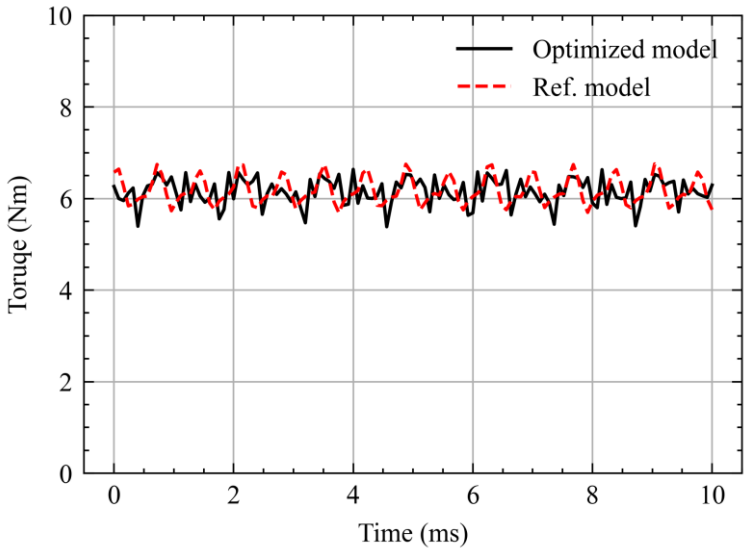

Fig. 3-16 Torque characteristics derived from the design domain with asymmetric rotor part

3.5 Summary

This section presents the multi-objective topology optimization of PMSM based on binary-encoded GA. Gaussian filter is employed to avoid checkboard problems. Both the symmetric and asymmetric rotor of the SynRM model is tested in simulation. The obtained results verify the feasibility and effectiveness of the proposed method.

However, the sharp and jagged edge in the optimized solution may bring a higher torque ripple. In the next chapter, a high-resolution edge-smoothing method will be proposed to bring a smooth rotor edge.

Regarding multi-objective evolutionary optimization, NSGA-II is a good choice for its elitism and easiness. The optimization method helps eliminate the meshing process and uses randomness to reduce the time consumption of topology change operations. However, it also has many issues, like a jagged or irregular shape, which is unsuitable for manufacturing; the performance of local search in shape remains terrible. At the same time, this algorithm requires a complete filter to determine if the generated model is viable, and we can use machine learning methods for preliminary screening and prediction. In addition, the FE calculation takes a lot of time. On the one hand, this method can be replaced with machine learning.

Chapter 4. Multi-Objective Topology Optimization of Asymmetric IPM motor using High-Resolution Interpolation and Edge-Smoothing Method

4.1 Introduction

Asymmetric interior-PM (AIPM) motors have been of increasing research interest in the last decade, which are recognized as promising candidates for aircraft and traction applications due to a low manufacturing cost, less use of rare earth, and high thermal resistance. However, the AIPMs have disadvantages such as high ripple and low average torque. Designing a high-performance AIPM through parametric optimization is challenging since the limited parameters prevent the optimization algorithm from finding the design space that contains the global optimum.

In this chapter, a three-phase AIPM has four rotor poles, and twenty-four stator slots will be optimized (c.f. Fig. 4-1) using TO. The iron core of the rotor and stator consists of laminated and stacked non-oriented silicon steel. During the TO of the AIPM motor, maximum torque per Ampere (MTPA) is employed as a control strategy, and the rated current i0 and its phase angle γ_{MTPA} vary jointly when the topology and shape of

stator and rotor change, which would normally require several FE simulations to acquire accurate torque.

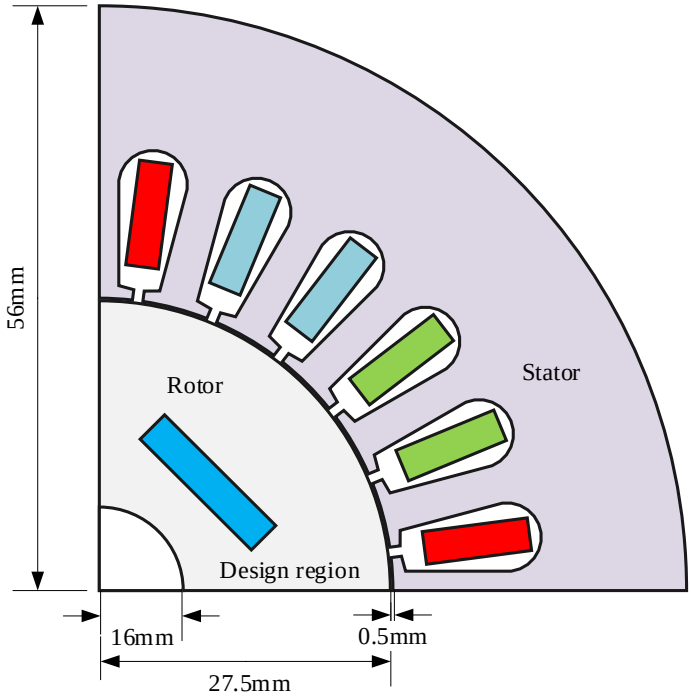

Fig. 4-1. Definition of a candidate model.

.

4.2 Two-stage Simulation

Two-stage simulation is proposed to acquire the accurate torque angle for rotors with PM inside like IPM motor and PM-assisted SynRM.

The output torque of an interior permanent magnet (IPM) motor is composed of two components, namely the PM torque and the reluctance torque. The output torque can be expressed as:

$$T_{syn} = T_{pm} + T_{rel} = \frac{3p}{2}\left[\psi_{pm} i_s \cos\beta + \frac{1}{2}(L_q - L_d) {i_s}^2 \sin 2\beta\right] \quad (4\text{-}1)$$

where, T_{syn}, T_{pm}, and T_{rel} are the synthetic torque, the PM torque and the reluctance torque, respectively; p is the pole-pair number; Ψ_{pm} is the PM flux linkage; i_s is the amplitude of phase current; β is the current advancing angle; and L_d and L_q are d- and q-axis inductances, respectively.

As clearly shown in (4-1), the frequencies of the PM torque and the reluctance torque waveform are different, where the frequency of reluctance torque is twice that of the PM torque, as shown in Fig. 4-2. The synthetic torque represents the actual output torque of the IPM motor. The maximum value of synthetic torque occurs at a current advancing angle between the maximum values of the PM torque and the reluctance torque.

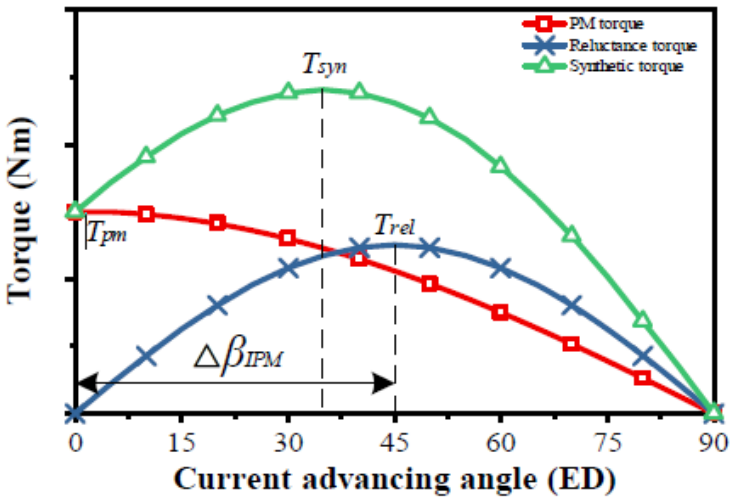

Fig. 4-2. The torque waveform of IPM motors when the rotor is locked [116].

As the current advancing angle of the maximum value of synthetic torque of an IPM motor is uncertain due to the variation of machine topology and the initial rotor position, it is important to perform the simulation of machine performance in two steps. The initial current advancing angle of maximum synthetic torque is captured in the first step, and the full-load simulation is conducted to obtain the average torque and torque ripple in a subsequent step. In the following sections, the principle of MTPA control strategy is introduced at first, and the detailed operation method of obtaining the maximum value of average torque and minimum value of torque ripple in the full-load operation of an IPM motor is described in a later section.

4.2.1.1 MTPA control strategy

In the IPM machine system, the transformation of coordination systems is usually performed to convert the static three-phase coordination system to the rotational two-phase coordination system. Clarke transformation and Park transformation are applied in this process. As a result, the three-phase armature currents can be decoupled to d- and q-axis currents, and a Vector Control (VC) can be realized.

MTPA is the abbreviation of Maximum Torque Per Ampere, which is a common control strategy in IPM motors. Compared to the I_d=0 control strategy, MTPA is suitable for electric machines with a notable difference between d- and q-axis inductances, including IPM machines, PM-assisted synchronous reluctance machines (PMA-SynRM), and so on. With a suitable distribution of d-axis and q-axis currents, the output

torque over the unit armature current can be maximized. Fig. 4-3 presents the current-torque characteristics of PMSM machines. The MTPA curve is obtained by connecting the closest point to the origin of the constant torque curves.

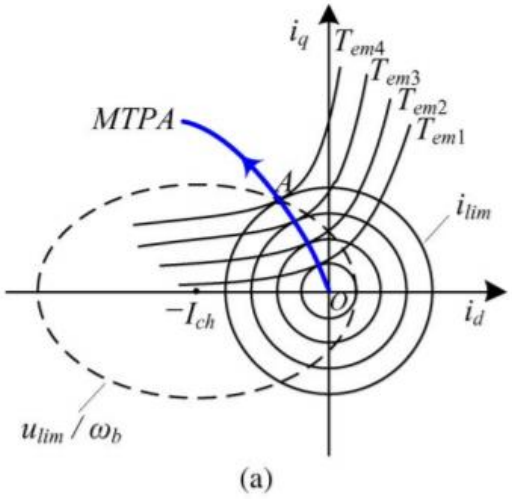

Fig. 4-3 The current-torque characteristics of MTPA control strategy [117]

The MTPA curve can also be obtained by using the concept of the current limit circle as shown in (4-2)-(4-5):

$$\mathbf{i_s} = \sqrt{i_d^{\,2} + i_q^{\,2}} \tag{4-2}$$

$$\beta = \arctan(i_d / i_q) \tag{4-3}$$

$$\frac{dT_{syn}}{d\beta} = 0 \tag{4-4}$$

$$\frac{d^2T_{syn}}{d\beta^2} < 0 \tag{4-5}$$

where, $\mathbf{i_s}$ is the vector expression of stator current. When the magnitude of $\mathbf{i_s}$ remains constant, the MTPA control strategy can realize a maximum output torque. Meanwhile, the MTPA control strategy can improve the system's dynamic response and overall efficiency.

4.2.2 Realization of MTPA in the simulation of AIPM machines

As stated in previous sections, the MTPA control strategy is suitable for IPM machines to generate the largest torque with stator armature currents with a constant magnitude. In the machine optimization process, the maximum value of output torque and minimum value of torque ripple are usually taken as the objectives. Therefore, it is necessary to perform the simulation in two steps. Fig. 4-4 shows the workflow for two-stage simulation during the MOGA.

4.2.2.1 Simulation of output torque when the rotor is locked

In the first simulation, the rotational speed of the IPM rotor is set to be zero, and the armature current is input as normal three-phase currents for the generation of a rotational magnetic field as shown in (4-6) - (4-8).

$$i_a = i_s \sin(2\pi ft) \tag{4-6}$$

$$i_b = i_s \sin(2\pi ft - 2\pi/3) \tag{4-7}$$

$$i_c = i_s \sin(2\pi ft + 2\pi/3) \quad (4\text{-}8)$$

where, i_s is the amplitude of stator phase currents and f is the electric frequency of armature currents. The maximum output torque of the machine occurs at a certain electric angle between the magnetic fields generated by the armature currents on the stator and the excitation PM on the rotor, which is the initial current advancing angle we would like to capture in this step. Ansys Maxwell is used in the simulation process. The initial current advancing angle is obtained as a value of the initial time t_0 of the current phase, where the initial current advancing angle β_0 can be obtained by $\beta_0 = 2\pi f t_0$. The output torque at the initial current advancing angle β_0 is the maximum torque that can be generated at a stator current with a constant magnitude, which conforms to the working principle of the MTPA control strategy.

4.2.2.2 Simulation of output torque in full-load operation

As the initial current angle β_0 is obtained in the previous step, and the full-load simulation of output torque is conducted in the subsequent step. The initial phase of the current angle is modified by inserting the time t_0 into the expression of phase currents as shown in (4-9) - (4-11):

$$i_a = i_s \sin(2\pi f(t + t_0)) \quad (4\text{-}9)$$

$$i_b = i_s \sin(2\pi f(t+t_0) - 2\pi/3) \quad (4\text{-}10)$$

$$i_c = i_s \sin(2\pi f(t+t_0) + 2\pi/3) \quad (4\text{-}11)$$

Meanwhile, the machine's rotor is set to rotate at the rated operation speed. With a corresponding frequency of the armature three-phase currents, the rotor excitation field and the stator armature field are coupled, and stable output torque is produced. The machine's average torque and torque ripple are obtained in this second step simulation process, and the optimization is proceeded according to the results of machine performance.

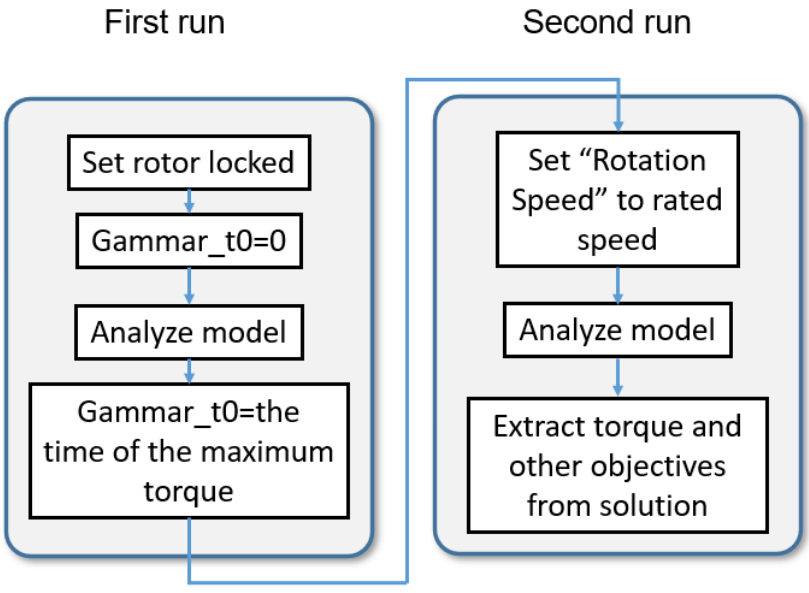

Fig. 4-4. Workflow of two-stage simulation to get the accurate degree of torque angle for symmetric and asymmetric IPM motor.

4.3 High-Resolution Encoding in Two-Dimension

Since the genetic algorithm (GA) is employed as the optimization algorithm in this study, a novel high-resolution encoding in 2-D as the chromosomes of GA and the detailed definition and implementation is described in the following subsections.

4.3.1 Two-Dimension Encoding and Interpolation

The linear bit string encoding is the symbolic feature of GAs, and most of the state-of-art GAs have been designed based on linear encoding.

The offspring variables are encoded into one-dimensional(1-D) chromosomes to fit the linear strings, as shown in Fig. 4-5. However, for the distribution of material, such as topology, the connection of specified features will be truncated.

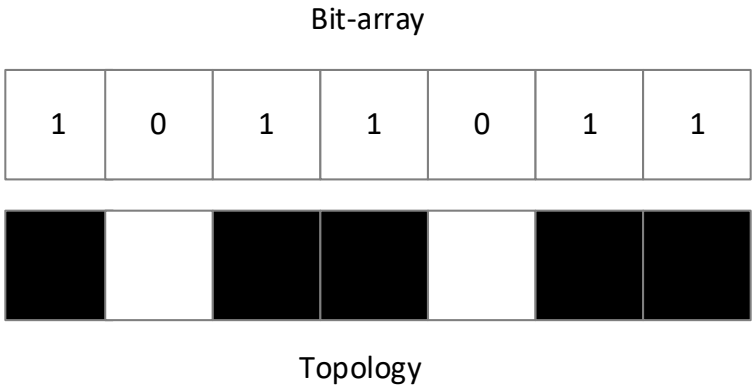

Fig. 4-5. 1-D encoding bit-array and equivalent topology.

The broken feature only has part of the useful features and could lead to poor convergence characteristics. Therefore, 2-D encoding became an alternative solution for certain problems. A demonstration of 2-D encoded topology is shown in Fig. 4-6.

The bitmap matrix (Fig. 4-6 (b)) only has 0 and 1 values, which is a binary-encoded bitmap.

Cohoon and Paris first proposed 2-D encodings and demonstrated moderate success in solving such a problem [118]. This approach led to the development of various crossover methods, which will be described in the following subsection.

Topology

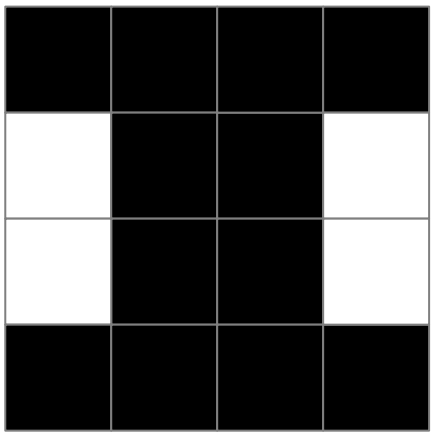

Bitmap

1	**1**	**1**	**1**
0	**1**	**1**	**0**
0	**1**	**1**	**0**
1	**1**	**1**	**1**

(a) (b)

Fig. 4-6. An example of topology bitmap representation (1–filled, 0–void)

4.3.2 Two-dimension Genetic Operation

Compared with one-dimension encoding, 2-D encoding consists of more graphic information [52], [118], [119]. In this study, 2-D binary crossover and mutation are proposed.

A crossover operator conventionally exchanges some information between two chromosomes with probability P_c. For 2-D binary crossover, the input is two binary-

encoded chromosomes c_{p1} and c_{p2}. The output is two-binary encoded chromosomes c_{o1} and c_{o2}. The 2-D crossover is described as follows.

Step 1: Generate a random number R representing the 2-D crossover probability.

Step 2: If R<P_c, skip the crossover operation; otherwise, perform a 2-D binary crossover.

Step 3: Generate four random integer numbers x, y, d_x, d_y to represent the start position (x,y) in c_{p1} and c_{p2}, and the horizontal and vertical distance of a small rectangular mask (d_x, d_y).

Step 4: The masked 2-D rectangle will make a copy but only swap the masked area. Detailed operation can be found in Fig. 4-7, the $(x,y) = (6,1)$, (d_x, d_y) = (2,7), and the masked area size is 14.

Step 5: The content inside the masked area (inside the red box) will be interchanged; the interchanged outputs are Co_1 and Co_2.

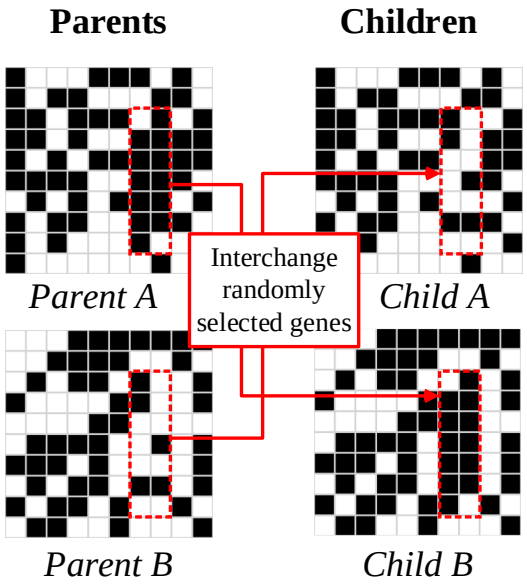

Fig. 4-7. Illustration of 2-D binary crossover.

The mutation is a genetic operator used to maintain the genetic diversity of a population of chromosomes between generations with the probability P_m. For 2-D binary mutation, the input is one binary-encoded chromosome c_p. The output is one binary encoded chromosome c_o. The 2-D mutation is described as follows.

Step 1: Generate a random number R representing the 2-D mutation probability.

Step 2: If R<P_m, skip the mutation operation; otherwise, perform a 2-D binary mutation.

Step 3: Generate four random integer numbers x, y, d_x, d_y to represent the start position (x,y) in c_{p1} and c_{p2}, and the horizontal and vertical distance of a small rectangular mask (d_x, d_y).

Step 4: The masked 2-D rectangle will make a copy, the new copy is the unprocessed output Co. Detailed operation can be found in Fig. 4-8, the $(x,y) = (5,2)$, (d_x, d_y) = (3,4), and the masked area size is 12.

Step 5: The content inside the masked area (inside the red box) will be flipped in Co, and the interchanged output is the flipped Co.

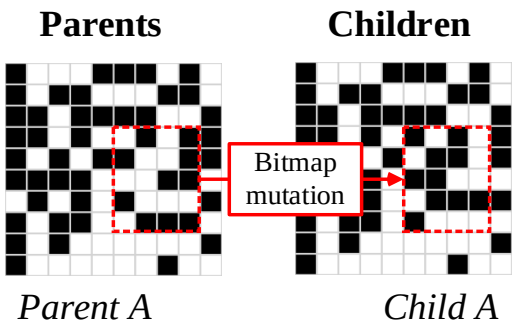

Fig. 4-8. Illustration of 2-D binary mutation.

4.3.3 High-Resolution Interpolation

Although 2-D encoding could solve real problems, Sigmund points out that for non-gradient topology optimization (NGTO) problems, coarse elements in the design domain cannot correctly represent the underlying physical problems [28]. Moreover, the coarse element will not cover optimal solutions with fine scale. However, in TO for electric motors, the number of holes inside the rotor is relatively small. Therefore, though fine mesh with additional elements is needed for the TO of electric motors, the topology is simpler than mechanical TO. The binary-encoded GA can be a potential solution for TO.

This section uses an interpolation method to make the bitmap, i.e., the 2-D coarse topology, into a high-resolution topology. The interpolation method is B-spline interpolation with a smoothing factor of zero. Fig. 4-9 shows a demonstration of 2-D topology interpolation.

The level of the interpolated topology is determined by a constant c.

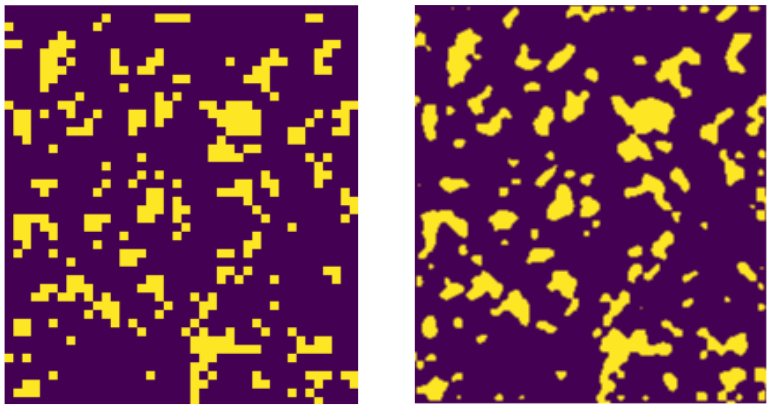

(a) (b)

Fig. 4-9. A demonstration of a bitmap using 2-D interpolation with the contour parameter c=0.5. (a) original topology (40*46), (b) interpolated topology (200*230).

4.4 Convert CAD Model using Edge Smoothing Method

Most topology results obtained using density-based methods are described in matrix-based elemental densities during topology optimization. Since the 2-D matrix-based topology describing the finite element model is based on a constructed mesh, this introduces a jagged shape that leads to inaccurate results, making it difficult to evaluate some critical properties of the motor, such as cogging torque, with this approach.

Therefore, manual interventions are required to process the topology optimization results to produce accurate computer-aided design (CAD) models. The density threshold method is the most widely used; in this method, the contours of the density matrix are used to extract the boundaries.

However, this method requires a suitable density threshold to obtain valid results. Moreover, if this method is used to obtain CAD models of complex structures, fragile

parts, rough surfaces, and disconnected structural components (isolated islands) may appear.

This section proposes an automatic process of converting bitmap topologies into DXF models. After the generated topologies, the small size of topologies volumes is sieved, and the large ones are kept. This method is described as follows.

Step 1: Find the boundaries of the topologies.

Step 2: Extract the boundary points and use a cubic uniform B-spline curve to obtain the fitting curves of the topology.

Step 3: Identifying the small features. Find the small, closed, disconnected structural topologies and remove them based on the predefined threshold.

Step 4: Approximate B-spline curve using a two-point line to reduce model complexity when generating mesh in finite element analysis.

The whole process can be found in Fig. 4-10.

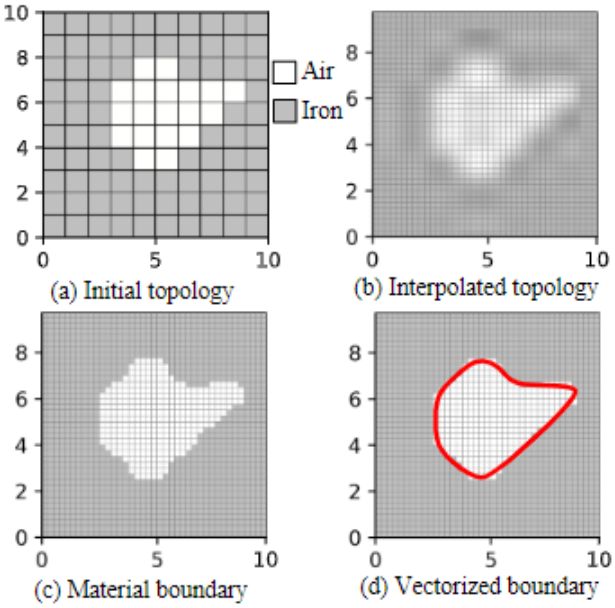

Fig. 4-10. The overall process of high-resolution interpolation and edge smoothing method. (a) is binary encoded topology (10*10) for genetic algorithm, (b) is interpolated bitmap topology (50*50), (c) is smoothed edge based on using suitable density threshold, i.e., 0.5 in this figure, and (d) is the vectorized boundary for FE model.

4.5 Experiment Verification

4.5.1 Machine configuration

The design object is the rotor of a 24-slot 4-pole AIPM. The motor characteristics are as follows; the stator outer diameter is 112mm, the stator inner diameter is 56 mm, the stator stack length is 50 mm, outer rotor diameter is 55 mm, the inner diameter of rotor lamination is 16 mm, lamination thickness is 0.35 mm. The number of stator slots is twenty-four. The design region is not one-eighth but one-fourth of the rotor region, as shown in Fig. 4-12, because we assume that the rotor shape is asymmetric in one

pole region. At the first iteration we will design the distribution of the material in 1840 cells, composed of 46 by 40 parts.

This optimization aims to maximize the torque average and minimize the torque ripple of the IPM motor.

The two objective functions are defined by

$$\begin{cases} F_1 = -T_{avg} \\ F_2 = T_{max} - T_{avg} \end{cases} \tag{4-12}$$

F1 and F2 are minimized, which are the average torque and torque ripple.

This study applies a modified non-dominated sorting genetic algorithm II (NSGA-II) method with a two-stage torque angle evaluation process. Two objective functions, including maximizing average torque (F1) and minimizing torque ripple (F2), are evaluated using finite element analysis (FEA).

The population with a high ranking is reproduced in the next generation. We adopted 2-D binary crossover and 2-D binary mutation to produce a diversified population. The numbers of populations and generations are 40 and 250, respectively. The crossover factor is 0.9, and the mutation factor is 0.1. The optimization process is shown by the flowchart of Fig. 4-11.

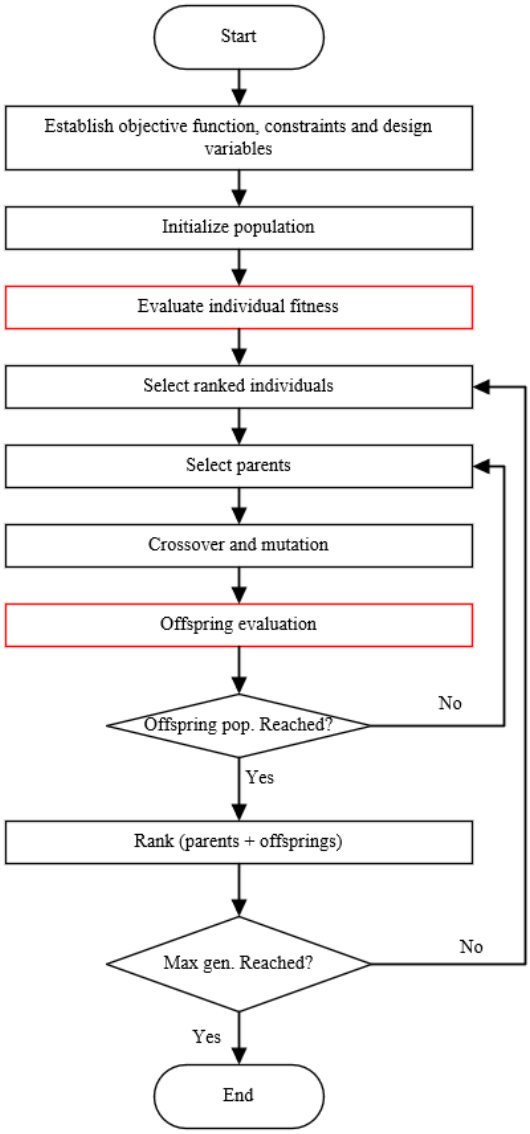

Fig. 4-11. The flowchart of modified NSGA-II for TO.

4.5.2 Design Domain of Asymmetric Rotor

The stator and the asymmetric rotor for the considered optimization problem are presented in Fig. 4-12. And the design parameters are listed in Table 4-1. A 40×46 (totaling 1840 variables) 2-D matrix was used to represent the distribution of the IPM rotor, as is shown in Fig. 4-13.

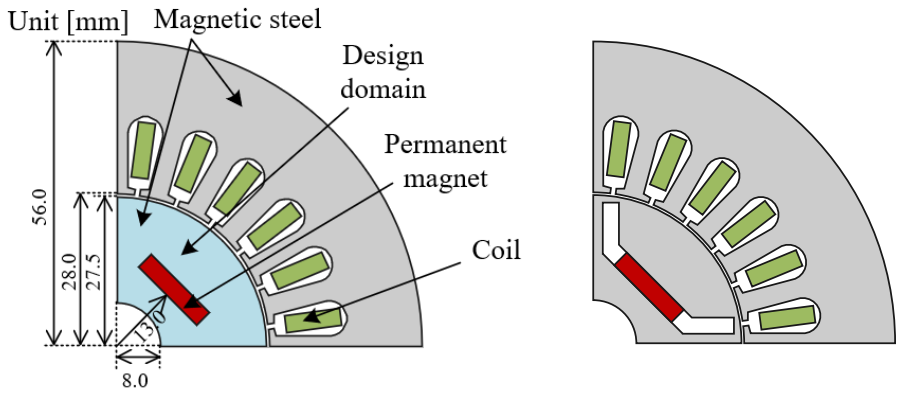

Fig. 4-12. (a) is the configuration of the 24-slot 4-pole IPM motor, and (b) is the reference model.

Table 4-1. Specification of reluctance motor

Property	**Value**
Number of Slots	24
Number of Poles	4
Type	Reluctance Motor
Design Domain Materials	Iron or Air
Speed	3600 RPM
Air Gap Length	0.5 mm
Excitation Source	Ideal Current Source

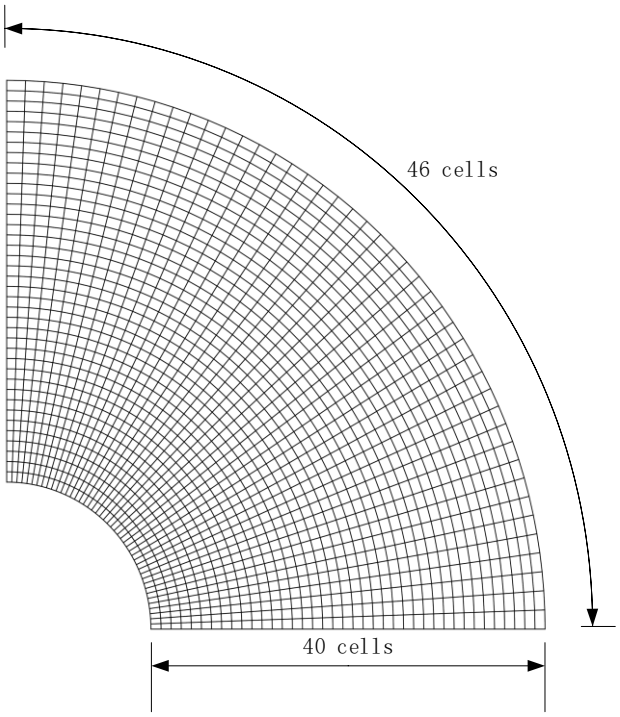

Fig. 4-13. The design domain of the rotor.

4.5.3 Experimental environments

The FE software used in this study is Ansys Maxwell, and the optimization framework is developed based on Python combined with Platypus [65] and NumPy [107].

This study shows that for the 100th generation, the computation time on two Intel Xeon Gold 6145@2.5 GHz is about 144 hours, with the number of cells and generations set to 46*40 = 1840 and 10000, respectively.

4.5.4 Optimal Solution for Asymmetric Rotor

Final optimization results are obtained by the topology optimization framework using the proposed methods. The obtained Pareto-front solution is shown in Fig. 4-14.

The strategy for selecting the optimized model from the Pareto-front solution is mainly based on the complexity of generated topology. Therefore, the optimized models with a relatively simple rotor surface and a feasible, manufacturable topology can be selected as the candidate models from the Pareto-front solution.

The values of T_{avg}, T_{ripple} of selected optimized models are shown in Fig. 4-15. It can be observed from these results that both T_{avg} and T_{ripple} are improved by the proposed method. As a result, the solution obtained by this present method has a smaller objective function value than the conventional method.

Fig. 4-17 shows the comparison of torque waves of the proposed method and the conventional method. Model 0 has lower torque and lower torque ripple, while model 1 has higher torque and higher torque ripple. Compared with the reference model, both of the selected optimized models have at least a 30% torque increment. However, the torque ripple of model 1 is 60% larger than the reference model. Therefore, regarding the topological structure's feasibility and performance, model 0 is selected for further simplification. Figure 4-18 shows the complete mechanical structure of the original model 0 and simplified model 0. Resin epoxy is used to fill the empty parts. A 0.25 mm thick carbon fiber sleeve prevents the optimized AIPMSM rotor from expanding due to

radical acceleration. The performance of simplified model 0 is slightly better than the original one. The von Mises stress distributions of the original model 0 and the simplified model 0 are shown in Fig. 4-19. The 3-D model of simplified model 0 is presented in Fig. 4-20. The simplified model can be manufactured by the low-speed wire electrical discharge machine.

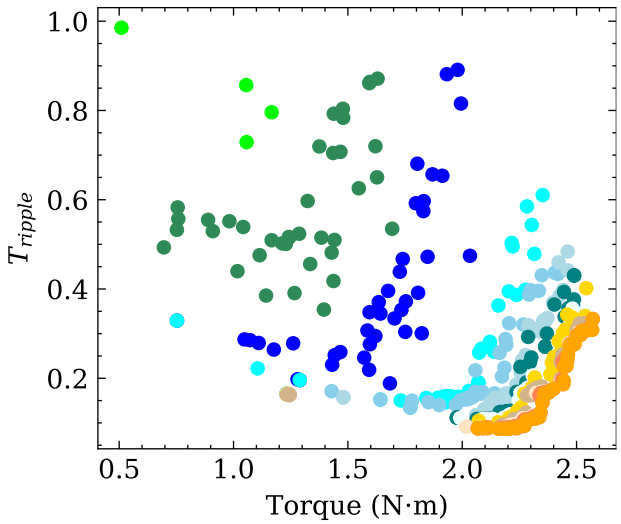

Fig. 4-14. Obtained Pareto-front solution of every ten iterations. T_{ripple} is defined by the maximum torque minus the minimum torque over the average torque.

(a) Model 0
T_{avg}=2.41Nm
T_{ripple}=0.38Nm

(b) Model 1
T_{avg}=2.57Nm
T_{ripple}=0.85Nm

(c) Reference Model
T_{avg}=1.83Nm
T_{ripple}=0.53Nm

Fig. 4-15. Comparison of torque and torque ripple between model 0 (a), model 1 (b), and reference model (c).

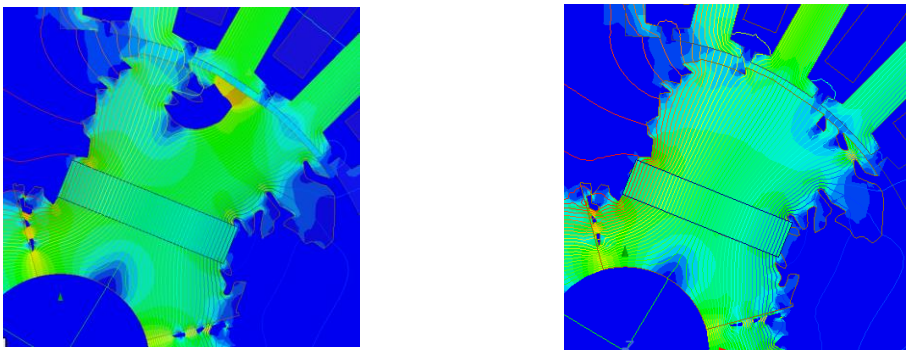

(a) (b)

Fig. 4-16. Magnetic flux line of optimal model 0 (a) and model 1 (b).

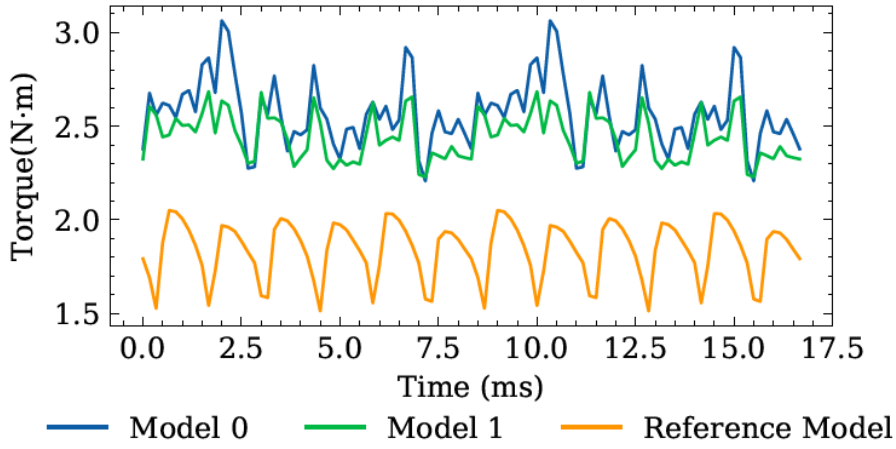

Fig. 4-17. Comparison of torque performance among Model 0, Model 1, and reference model.

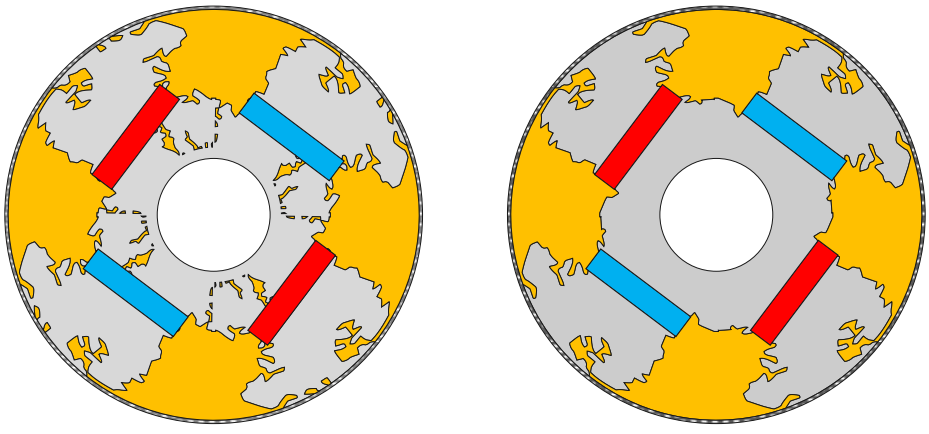

(**a**) (**b**)

Fig. 4-18. The whole model of the selected topology optimized AIPMSM rotors. The yellow parts are filled with resin epoxy, and a carbon fiber sleeve protects the whole rotor. (a) is the original model 0, the torque is 2.419 Nm, and the torque ripple is 0.308 Nm; (b) is the simplified model 0, the torque is 2.452 Nm, and the ripple is 0.366 Nm.

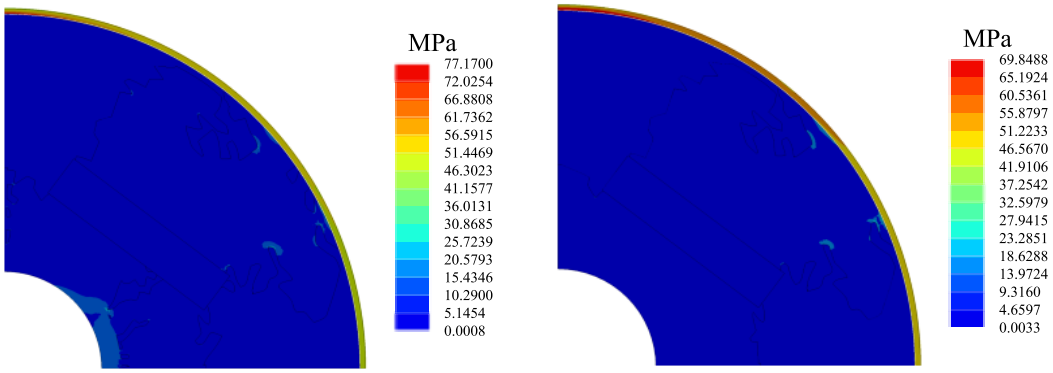

(**a**) (**b**)

Fig. 4-19. The von Mises stress distributions at 3600 rpm for topology-optimized AIPMSM rotors, (a) is distribution of the original selected model 0, and the maximum von Mises stress is 77.1700 MPa, and (b) is the distribution of the simplified model, and the maximum von Mises stress is 69.8488 MPa..

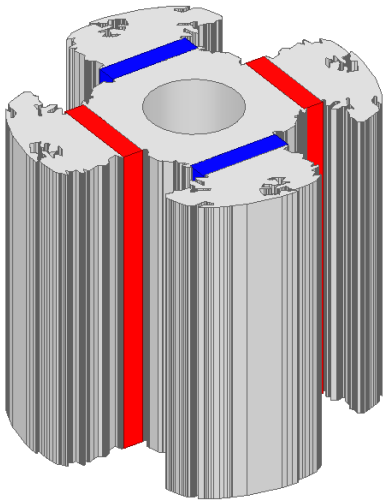

Fig. 4-20. A 3-D view of simplified model 0.

4.6 Summary

This chapter proposes a novel topology optimization method for AIPM based on two-stage simulation, high-resolution encoding, and edge smoothing. In this present method, the global search is conducted using modified binary-encoded NSGA-II. Then, the solution obtained by the global search is improved by the post-processing method to simplify the optimized model. The topology of the rotor of AIPM has been optimized to test this present method. Compared with the reference model, we have found that the performance of the optimized solutions is much improved by this method. Despite the increased computational time of the model, better results are obtained with the help of the CAD model during the TO, representing a more feasible electromagnetic structure.

Chapter 5. A Fast Magnetic Field Approximation Method for Simulation of Magnets using AI

5.1 Introduction

This chapter introduces a new concept for the magnetic performance evaluation method by approximating magnetic fields directly from a conditional generative adversarial network (cGAN). Our approach can evaluate the performance of any electromagnetic device, such as air gap flux density and transmission torque, with modest computational cost in terms of novel design. Unlike the analytical method, the model proposed in this chapter could derive the entire magnetic field distribution in the design space, which is beneficial for further analysis. In addition, we utilize a physics-based loss function to ensure that the network training is directly performance parameters. A neural network for solving the magnetic field distribution of coaxial magnetic gears (CMG) will be trained and evaluated in this study.

This study is divided into seven parts. Section 5.2 introduces the general knowledge about magnetic gear (MG) and the torque calculation method. Section 5.3 deals with the preliminary background and concept of generative adversarial networks (GANs). Section 5.4 is concerned with the methodology used for this study. This section introduces the working principle, the architecture of the proposed network, the training

process, the PM representation method, and neural network configurations. Section 5.5 presents the key parameters that influence the neural network's performance. Section 5.6 demonstrates the preliminary results obtained from the proposed network. The conclusion is drawn in Section 5.7.

5.2 Technical Preliminaries

This section formulates the magnetic gear working principle and the torque calculation using the Maxwell stress tensor method in the polar coordinate system.

5.2.1 Magnetic Gears

Magnetic gears have attracted much attention due to the advantages of free-of-contact, inherent overload capability, silent operation, and high reliability compared with mechanical gears [120], [121]. The coaxial magnetic gear (CMG), which comprises coaxial inner and outer rotors on the two sides of ferromagnetic segments, realizes a better utilization of PMs and transmits significantly higher torque density compared with other types of MGs [122], [123]. Therefore, CMGs have been employed in critical environments to meet the high requirement and harsh working conditions. For example, high-efficiency and high-performance magnetic gears have been used in electric vehicles (EVs) [2], electricity propelled ships [124], [125], and electric aircraft [126]–[128].

Many methods are developed to improve the performance of magnetic gears, such as the analytical method [121], [129], equivalent magnetic circuit method [130], finite element (FE) method, and so on [131]–[133]. However, the current calculation methods have some shortcomings. The FE method is an accurate tool for simulation but exceedingly highly time-consuming. On the contrary, the analytical method requires few computation resources, but the generalization ability is limited.

Since Magnetic gears utilize the energy exchange between magnetic field energy and mechanical energy, they have many advantages compared with traditional mechanical gears.

The first high-performance magnetic gear was proposed in 2001 [134]. The main components of this CMG are shown in Fig. 5-1.

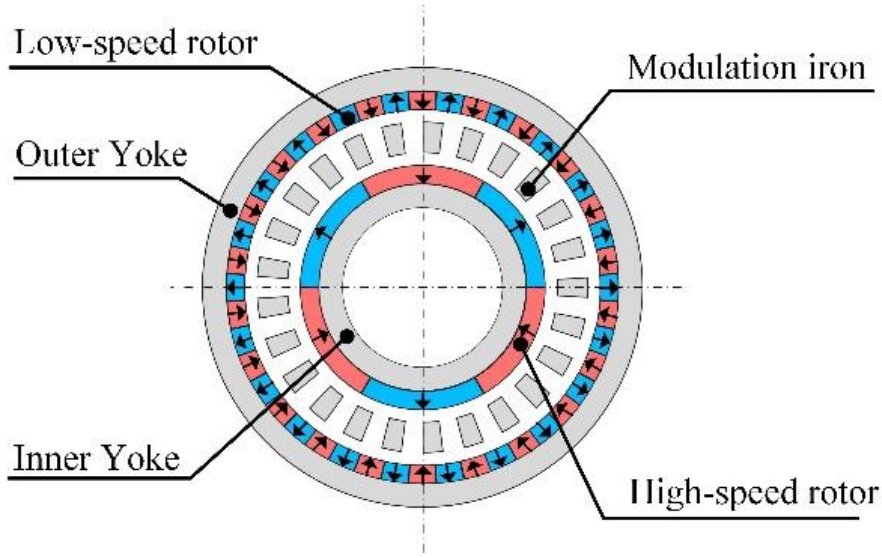

Fig. 5-1. Two-dimensional structure of surface-mounted type permanent magnet (PM) coaxial magnetic gear.

The operation of CMG is based on modulating the magnetic field produced by the rotating magnetic poles of the high-speed rotor in the iron poles of the stationary part; meanwhile, the low-speed rotor will be driven in the opposite direction by the magnetic field modulated in the modulation iron. It has been shown that the highest torque transmission is obtained with the following equality:

$$p_{out} = N_s - p_{in} \quad (5\text{-}1)$$

where p_{in} is the number of poles pair for the inner (high-speed) rotor, N_s is the number of modulation iron segments, and p_{out} is the number of outer (low speed) rotor, respectively.

The correlation between the output (ω_{out}) and input (ω_{in}) speed and the gear ratio (gr) are:

$$\omega_{out} = gr \times \omega_{in} \quad (5\text{-}2)$$

$$gr = \frac{\omega_{out}}{\omega_{in}} = -\frac{p_{in}}{p_{out}} \quad (5\text{-}3)$$

Furthermore, an optimal combination exists among p_{out}, p_{in} and N_s, which can significantly reduce the torque ripple when CMG is in operation [135]. This relationship can be defined by a coefficient k_r.

$$k_r = \frac{2p_{in} \times N_s}{LCM(2p_{in}, N_s)} \quad (5\text{-}4)$$

where LCM indicates the 'least common multiple' between p_{in} and N_s. The minimal ripple exists when the coefficient k_r reaches 1.

5.2.2 Magnetic performance of CMGs

5.2.3 Air Gap Flux Density

Air-gap flux density is one of the most critical parameters to optimize when designing permanent magnet (PM) devices.

This parameter directly indicates the performance of the PM device design in terms of torque. The air-gap flux density is typically derived from simulations during the PM device design stage.

Flux density distribution in the air gap generally reveals the performance of torque ripple and the order of harmonics of the motor. The high-order harmonics will increase cogging torque and the eddy current loss.

Therefore, it is an inevitable metric while designing a PM device. The air gap flux density can commonly be represented in the polar coordinate system in 2-D design or the cylindrical coordinate system in 3-D design to simplify the calculation process. It consists of two parts while ignoring the Z component, which can be expressed by

$$\begin{cases} B_\rho = B_x\, cos(\theta) + B_y\, sin(\theta) \\ B_\theta = -B_x\, sin(\theta) + B_y\, cos(\theta) \end{cases} \quad (5\text{-}5)$$

where B_x is x-component of the B vector, B_y is y-component of the B vector, B_ρ is radial-component of the B vector, B_θ is tangential-component of the B vector.

5.2.4 Magnetic Torque Calculation

Magnetic torque is one of the most critical performance indicators of magnetic gears. After determining the magnetic field distribution in the polar coordinate system in the two air gaps, the torque applied to the inner and outer rotors T_i and T_o can be obtained by using the Maxwell stress tensor [135], and is given by:

$$T_i = \frac{Lr_i^2}{\mu 0} \int_0^{2\pi} B_\rho(r_i, \theta) B_\theta(r_i, \theta) d\theta \quad (5\text{-}6)$$

$$T_o = \frac{Lr_o^2}{\mu 0} \int_0^{2\pi} B_\rho(r_o, \theta) B_\theta(r_o, \theta) d\theta \quad (5\text{-}7)$$

where L is the length of the model, r_i and r_o are the radius of the integration paths along the inner and outer air gaps, respectively.

5.3 GANs for Magnetic field Approximation

This section proposes a method capable of addressing the introduced problem, namely, physics-informed GAN. GAN is a machine learning framework designed by

Goodfellow et al. in 2014 [88], i.e., two neural networks compete in a zero-sum game, where the gains of one agent are the losses of the other agent.

5.3.1 Conditional GAN and Pix2Pix

Conditional GAN (cGAN) is one of GAN's earliest variants, changing the original GAN probabilities to conditional probabilities, i.e., cGANs learn a mapping from observed input x and random noise vector z, to y, $G : \{x, z\} \rightarrow y$. This condition can be pictures and annotations, making cGAN widely used in image processing and conversion.

Similar to GAN, the architecture of cGAN also consists of generator and discriminator models. The generator model can be responsible for generating new specious examples. Ideally, these examples are indistinguishable from the real examples in the dataset. The discriminator model is a classification network responsible for classifying a given input as ground-truth (extracted from the dataset) or fake (generated).

Pix2Pix is an efficient cGAN for image synthesis; it can effectively synthesize the output from labels, reconstruct objects from edge maps, and colorize images [89]. The objective function of Pix2Pix is defined as:

$$G^* = arg \min_G \max_D L_{cGAN}(G, D) + \lambda L_{L1}(G) \quad (5\text{-}8)$$

where $L_{cGAN}(G, D)$ is the loss function of PatchGAN, $L_{L1}(G)$ is the loss function of the generator (also is known as the mean absolute error (MAE)), and G^* is the final objective.

In our case, the generator network G is trained to generate the magnetic fields that match the material distribution of the input. The discriminator D is trained to determine whether the given inputs are constrained by the physical properties of magnetic fields.

5.3.2 Loss Functions for Magnetic Field Approximation

In Pix2Pix, the loss function of cGAN and L1 are:

$$L_{cGAN}(G, D) = E_{x,y}[\log D\,(x, y)] + E_{x,z}\left[\log\left(1 - D\big(x, G(x, z)\big)\right)\right] \quad (5\text{-}9)$$

$$L_{L1}(G) = E_{x,y,z}(||\mathrm{y} - G(x, z)||) \quad (5\text{-}10)$$

where *G* tries to minimize this objective against an adversarial *D* that tries to maximize it.

For the Pix2Pix model, the generator not only fools the discriminator but is also close to the ground-truth output in an L2 sense. Nevertheless, L1 distance is used rather than L2 as L1 encourages less blurring [89].

In magnetic field approximation, we have additional information on the underlying physics of magnetic fields. We not only want to generate a visually

appealing result, but we also want the generated magnetic field can be used for the performance calculation of magnetic gears.

Existing research with excellent prediction ability employs a sum of square error (SSE) to measure the squared error between the predicted field and the results obtained by using FEM [84], which usually can be written as:

$$L_{SSE} = \sum (B_{NN} - B_{FEM})^2 \tag{5-11}$$

where B_{NN} and B_{FEM} are the calculated magnitude data by the neural network and the FEM at each point.

Moreover, since torque is the critical parameter when analyzing magnetic gears, the torque can be obtained by the Maxwell stress tensor and given by (5-6) and (5-7). We can find the torque obtained by calculating the integral of the radial component times the tangential component of flux density. Therefore, minimizing the absolute error between the sum of the predicted magnetic field and the sum of the magnetic field obtained from FE simulation can be an effective method to find the solution.

The sum absolute error (SAE) of predicted results and FE simulation results is defined as:

$$L_{SAE} = \sum_{i=1}^{n} |B_{NN} - B_{FEM}| \tag{5-12}$$

where B_{NN} is the prediction, B_{FEM} is the results obtained from the FE simulation.

Our final loss function used during training is formulated as follows:

$$L = L_{cGAN} + \lambda L_{SAE} \quad (5\text{-}13)$$

where L_{cGAN} is loss of discriminator and L_{SAE} is the loss of our generator, and λ is one.

5.3.3 Neural Network Architecture

5.3.3.1 Generator

Two types of generators were implemented for the GANs in this work, and they are U-net and ResU-net

The U-net architecture does not have any fully connected layers, and they are replaced by upsampling operators that are added skip connections between each convolutional layer. An overview of this type of network is shown in Fig. 5-2, where the blue line represents the PM and iron inputs. Each blue box corresponds to a multi-channel feature map, including a convolutional layer, a batch-normalization layer, and a ReLU activation. The number of channels is denoted on top of the box. The x–y size is provided at the lower-left edge of the box. The arrows denote the different operations.

The residual block was first introduced in residual networks (ResNets) [136]. It has demonstrated significant performance across many benchmarks in the computer

vision field. Each residual block contains two convolution layers, two batch-normal layers, and two ReLU activations (c.f. Fig.5-2 (b)). The arrows denote the different operations.

ResU-net, a variant of U-net, combines the advantage of U-net and residual blocks [27]. It consists of a fine-to-coarse down-sampling path and a coarse-to-fine upsampling path with shortcut connections. Other network parameters are the same as the original U-net for every two convolutional layers at the same resolution level in U-net. The details of each block are given in Fig. 5-2 (b). Both U-net and ResU-net were tested in our work with fine-tuning.

5.3.3.2 Discriminator

The overview of the discriminator network is shown in Fig. 5-3, where the blue line on the left represents the inputs, and the gray line represents the magnetic field data obtained from the FE simulation. This discriminator tries to classify if each M×N patch in an image is real or fake using a convolutional block and averages all responses to provide the ultimate output of D.

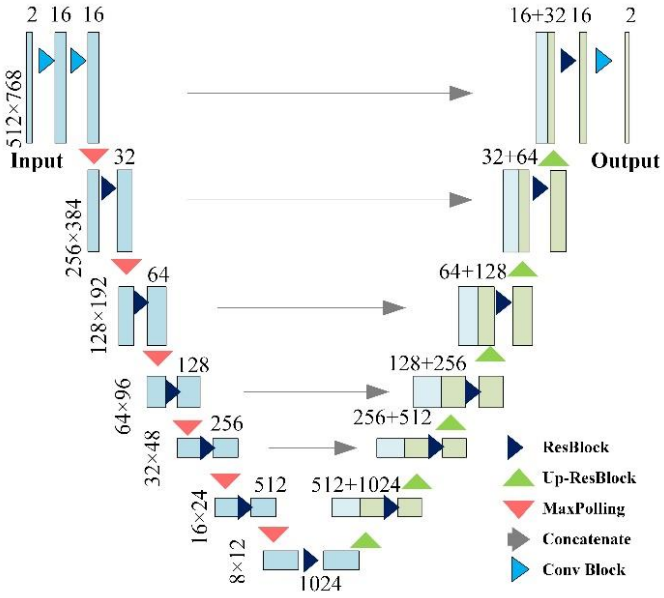

(a)

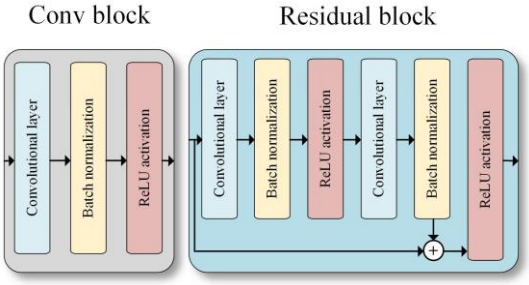

(b)

Fig. 5-2. The overview of the architecture of generator network. (a) ResU-net. (b) Details of blocks.

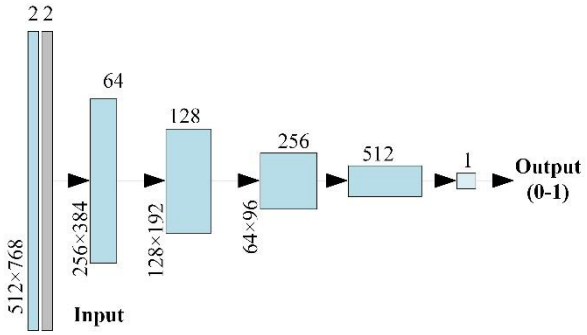

Fig. 5-3. The overview of the architecture of discriminator network.

5.4 Performance evaluation using GAN-based Magnetic field Approximation

This section presents the working principle and the training process of the proposed GAN model for magnetic field approximation in CMG.

5.4.1 Working Principle

Our model uses a ResU-net generator to approximate the magnetic field for CMG, see Fig 5-4. The detailed processes are described in the following:

Step 1: Material separation - the CMG model will be divided into two parts:

- Permeable materials – The relative permeability is greater than one and does not have a magnetization direction vector.
- Magnetic materials – The relative permeability is close to one and has a magnetization direction vector.

Step 2: Coordinate system (CS) conversion – we convert the input from the polar coordinate system into a rectangular coordinate system

Step 3: Pre-processing - we construct two tensors, namely the relative permeability tensor and the magnetization direction vector tensor. Then perform scaling and normalization operations on these two tensors, respectively. Then we do a padding

operation on the preprocessed tensor to make its shape convenient for neural network model training and processing.

Step 4: Evaluation - Feeding the input of the data into the neural network model and obtaining the output.

Step 5: Inverse data manipulation - we slice the generator's output to obtain the shape before the padding operation for post-processing.

Step 6: Inverse coordinate system conversion – we utilize coordinate system conversion on the output, i.e., convert B_x, B_y to B_ρ, B_θ.

Step 7: Performance evaluation – we post-process the output to find the air gap magnetic flux density and torque.

In this way, users no longer need to learn how to use finite elements and prepare high-performance computers for performance evaluation, significantly reducing the user's learning threshold.

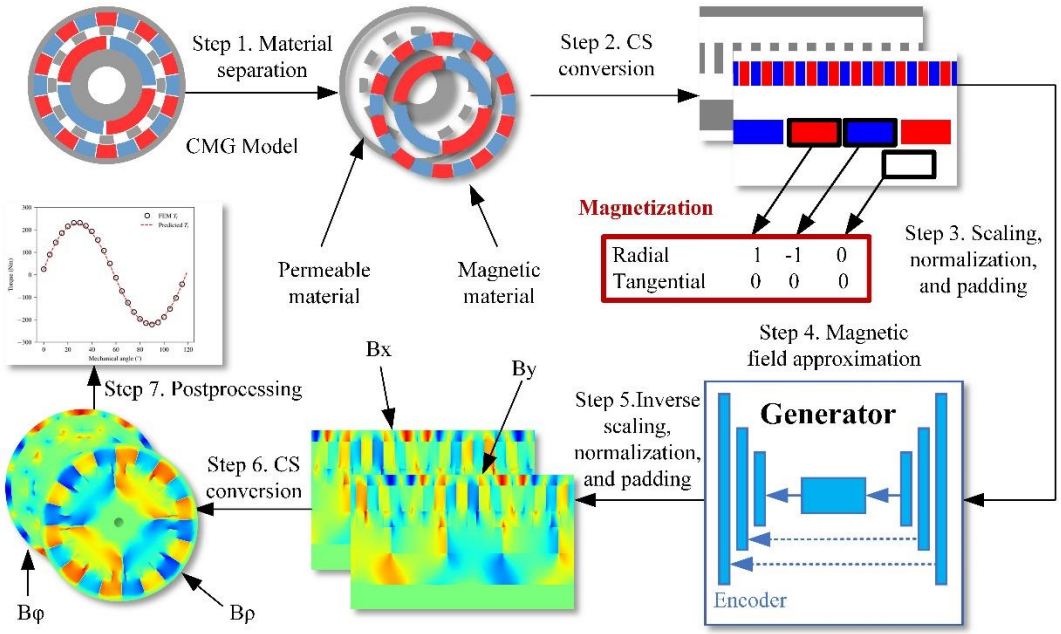

Fig 5-4. The workflow of magnetic field approximation for coaxial magnetic gears

5.4.2 Training Process

The detailed training process is demonstrated in Fig. 5-5. The FE simulation comes with a high computational cost but is executed only once. Moreover, the FE simulation can be generated in parallel and with a distributed computing platform.

First, many FE simulations are done with different random combinations of the input variables. The output data are extracted from FE solutions.

In the second step, we assemble the dataset and implement data preprocessing from extracted solution data from the FE simulation. This process is described in the following:

1. **Matrix scaling** - The output is scaled concerning the magnitude of flux density, ranging from 0 to 3 Tesla.

2. **Matrix normalization** - All the input and output variables are normalized. In this study, we use min-max normalization.

$$x' = \frac{x - min(x)}{max(x) - min(x)} \tag{5-14}$$

3. **Matrix padding** – In the process of convolution, padding is sometimes needed to avoid information loss.

Afterward, the preprocessed dataset is used for the training of the cGAN. For cGAN, the generator should be saved, and it will be used to evaluate the magnetic field of CMG.

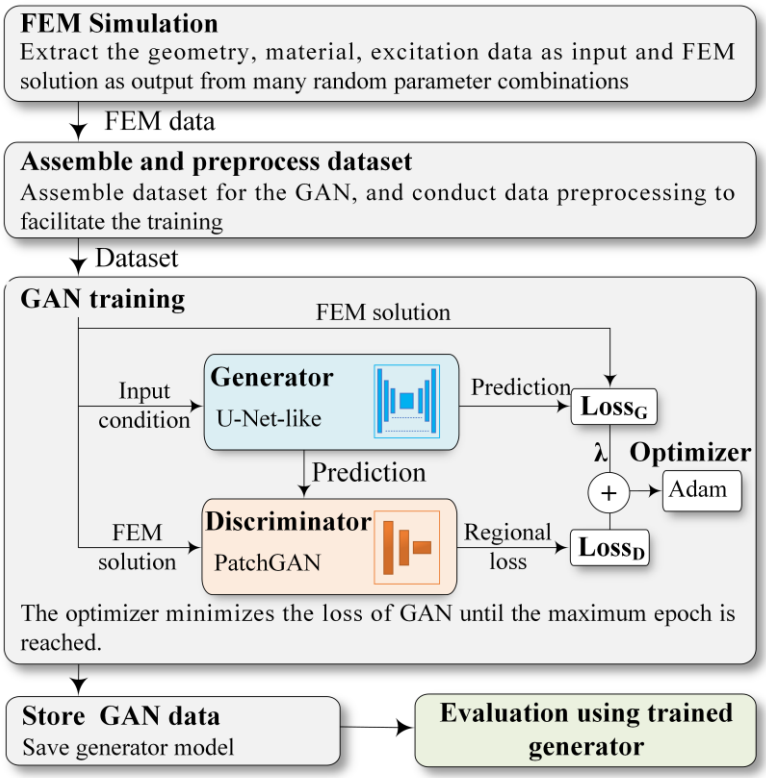

Fig. 5-5. The training process of magnetic field approximation for CMG using Pix2Pix.

5.4.3 Physical Property Representation

Magnetization of PM could influence the performance of CMG using FEM. In this study, we use a normalized vector to express the magnetization direction of the material. The first element of the vector represents the radial component, and the second element represents the tangential component. For example, (1, 0) indicates that the magnetizing direction is the positive radial direction, and (-1, 0) indicates that the magnetizing direction is the negative radial direction. (0,0) means non-magnetic material (cf. Fig 5-4).

5.4.4 Dataset Generation

Only the magneto-static problem is considered for a coaxial magnetic gear operating at low speed. The governing equation for the static magnetic field analysis, including a PM, is derived from Maxwell's equations as:

$$\nabla \times \left(\frac{1}{\mu_r \mu_0} \mathrm{B}\right) = \nabla \times H = J = 0 \tag{5-15}$$

$$\nabla \cdot B = 0 \tag{5-16}$$

$$B = \mu(H + M) \tag{5-17}$$

where μ_r denotes the relative magnetic permeability, μ_0 is the vacuum permeability (i.e., $4\pi \times 10^{-7} N/A^2$), B is the magnetic flux density, and B_r is the remanence of the PM material (i.e., the residual magnetic flux density), H stands for the magnetic field strength, M represents the magnetization strength of PM, and J represents the current density vector, which is determined as zero in this model. The parametric model of CMG is given in Fig. 5-6.

The training dataset is used to train the parameters of the GAN model, and the testing dataset is used to check the performance of the cGAN model on the unseen data. The FE simulation results produced both the training and testing datasets.

The input tensor and output tensor of our Pix2Pix model have the exact size of 512×768 pixels. The tensor, including material distribution and PM magnetization,

were interpolated from the results of the FE simulation with a spatial resolution of 0.1mm × 0.5 degree.

The magnetic field (B_x, B_y) are calculated in the 2-D FE simulation, then we use equation (5-6) to convert flux density B from Cartesian CS to Polar CS (c.f. Step 2 in Fig.5-4.).

The geometry parameters of the template CMG model are listed in Table I. Arbitrary pole pair of the high-speed and low-speed rotor, size of the yoke of the high-speed and low-speed rotor, and the open slot ratio of modulation iron segments and PM are simulated in the datasets. The rotor position was also randomly selected, as shown in Table II. The material of magnets is N35-NdFeB, the material of iron segments and two rotors is DW310, and the nonlinear B–H curve is shown in Fig. 5-7.

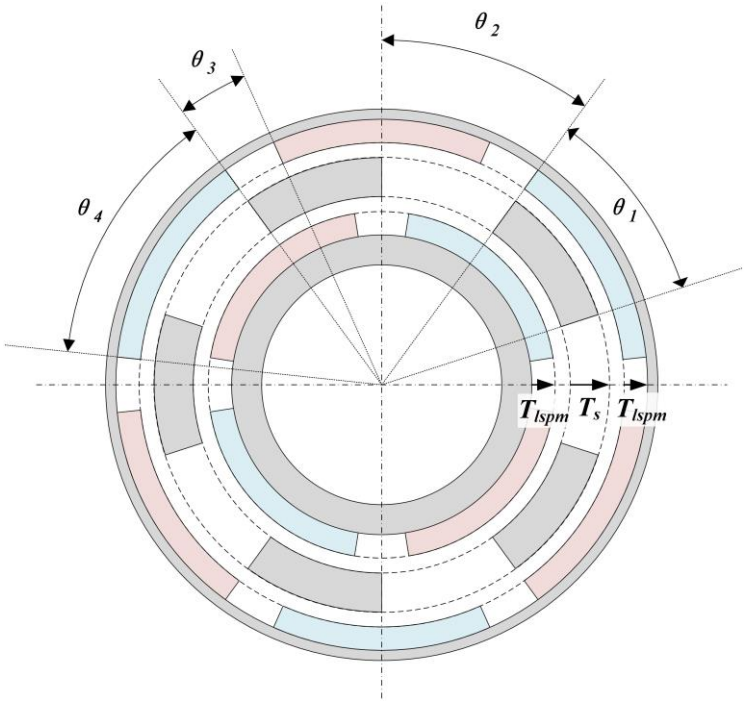

Fig. 5-6. The definition of the parametric CMG model.

We compute the resulting 2-D magnetic field and store 5,000 samples of these into the dataset, which is then used to train our neural networks. The hardware list of the training workstation is given in Table III.

Table 5-1. List of fixed parameters of the CMGs

	Parameter	Value	Unit
R_o	The outside radius of the MG	92	mm
T_{lspm}	The thickness of the PMs on the low-speed rotor	7.8	mm
T_{hspm}	The thickness of the PMs on the high-speed rotor	7.8	mm
T_s	The thickness of the modulation iron segments	13	mm
g	The length of the air gap	0.6	mm
L	Stack length	40	mm

Table 5-2. List of variables of the CMGs

	Parameter	Min.	Max.	Unit
P_{hs}	Number of pole-pairs at HS rotor	3	5	-
P_{ls}	Number of pole-pairs at LS rotor	10	25	-
N_s	Number of modulation iron segments	10	25	-
T_{oy}	The thickness of the yoke of the outer rotor	5	10	mm
T_{iy}	The thickness of the yoke of the inner rotor	5	10	mm
Ra_i	Slot open of modulation iron segments = $\theta_1/(\theta_1+\theta_2)$	0.3	0.7	-
Ra_{pm}	Ratio PM = $\theta_3/(\theta_3+\theta_4)$	0.5	1	-
φ_{ls}	Low-speed rotor position	0	360	Deg.

Table 5-3. Hardware list for magnetic field approximation

Hardware	Model	Specification
CPU	Intel Core i7-10870H	8-core @ 2.2GHz
GPU	NVIDIA GeForce RTX 3080 M	16GB RAM
RAM	DDR4 3200MHz	64GB

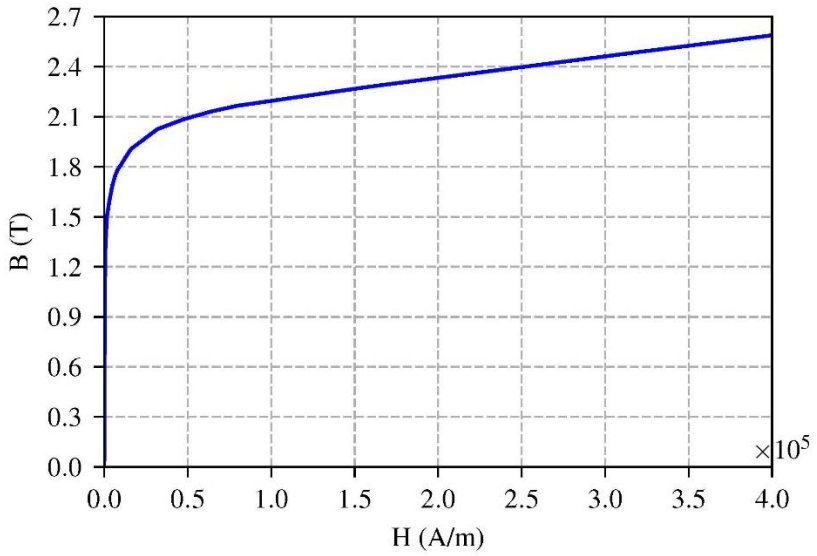

Fig. 5-7. The B-H curve of steel DW310 in the modulation iron segment and two rotors.

5.5 Influence of Key Parameters of Proposed Fast Magnetic Approximation Method

To discover the relationships between the key parameters and performances of magnetic field approximation, the influences that key parameters have on the network are investigated in this section. Except for specifically indicated parameters, design parameters of the CMG are fixed as given in Table I in the investigation of the influence of critical parameters.

The stochastic gradient-based optimization algorithm, Adam [136], is used in our network. The learning rate value determined was 2×10^{-4}. The proposed model is implemented in Python 3 with TensorFlow [137].

To objectively demonstrate the superiority of the proposed method, all the experiments were quantitatively evaluated using the structural similarity (SSIM) index

and the peak signal-to-noise ratio (PSNR). The SSIM index measures the similarity of structural information in two images, where zero indicates no similarity and 1 indicates total positive similarity. PSNR measures image distortion and noise level between two images. A higher PSNR value indicates a higher image quality. SSIM and PSNR are used for similarity verification of magnetic fields [138].

5.5.1 Layer Type of Generator

ResU-net is a fully convolutional neural network designed to get high performance with fewer parameters. It is an improvement over the existing U-net architecture. ResU-net takes advantage of both the U-net architecture and the deep residual learning.

The ResU-net consists of an encoding network, decoding network, and a bridge connecting these networks, just like a U-net. The U-net uses two 3 × 3 convolutions, where a ReLU activation function follows each. In the case of ResU-net, these layers are replaced by a pre-activated residual block.

5.5.2 MAE and SAE combined with λ

Since the difference between MAE and SAE is the number n of elements used for the computation, a comparison between SAE and MAE used for generators in Pix2Pix is conducted. For SAE, equivalent λ (i.e., 512×768 = 393,216) is used in the comparison. Also, we investigate the relationship between the indicators and the value of λ ranging from 1 to 10^8.

5.5.3 Quantitative evaluation

U-net and ResU-net are implemented by employing two different kinds of loss functions. Table 5-4 presents the performance on average MAE, SSIM, and PSNR across each method. It can be seen that the ResU-net combined with SAE demonstrates superior performance in cases compared to U-net, indicating that ResU-net works better along with the SAE in this work.

It is observed that the value λ between 10^4 and 10^6 has better performance than other values under the same generators, in which Pix2Pix, with equivalent λ value at 786,432 (512×768×2) has achieved the best MAE, PSNR, and SSIM.

Table 5-4. Comparison of metrics with different generators

Generator	Loss	λ	MAE ($\times 10^{-3}$) ↓	SSIM ↑	PSNR ↑
U-net	MAE [a]	100	19.90	0.8964	29.45
	SAE	1[b]	7.39	0.9811	39.23
ResU-net	MAE	100	13.39	0.9311	30.01
	SAE	1[b]	2.62	0.9962	47.42
ResU-net	MAE	10^0	75.67	0.7526	18.91
		10^1	85.16	0.7124	18.15
		10^2	12.73	0.9422	30.89
		10^3	6.46	0.9712	32.16
		10^4	3.55	0.9942	43.95
		10^5	2.91	0.9954	46.83
		10^6	3.59	0.9941	44.87
		10^7	3.66	0.9956	45.88
		10^8	3.65	0.9952	45.74

MAE, SSIM, and PSNR are calculated based on the mean value of the whole dataset. The arrow "↓" means lower is better, and "↑" means higher is better.

[a]U-net+MAE is the original configuration of the generator in Pix2Pix.

[b]The equivalent value of λ using MAE is 786,432 (512×768×2), which is between 10^5 and 10^6.

5.6 Experimental Verification

In the following section, we evaluate our novel method for magnetic field approximation and calculate the performance of CMG. In order to validate the proposed model, the predicted results have been compared with 2-D FE simulations obtained using ANSYS Maxwell software. The geometrical parameters given in Table V are considered.

The optimizer is Adam, with a learning rate value of 2×10^{-4}. The generator is a U-shape network (c.f. 5-2 (a)), including encoders and decoders. It consists of 12 blocks with skip connections, including six down-sampling blocks and six up-sampling blocks. The last output layer in the decoder will have a convolutional operation with a Sigmoid function, mapping the output to the number of the output channel. The discriminator architecture is an encoder, as is shown in Fig.5-3. After the last layer, a convolution is applied to map to a 1-dimensional output, followed by a Sigmoid function.

The training of our final model takes 76 hours. As for the evaluation process, the total magnetic field approximation time of the 360-step CMG model using our model is 26 seconds, of which the total neural network evaluation takes 11.65 second (the first step takes 4.4 seconds for initialization), the file read takes 10.55 seconds, and the torque calculation takes 0.44 second, the remaining time was used for preprocessing

and postprocessing. In comparison, the conventional FE simulation takes 26 minutes, and each step takes 4 seconds on average. Convergence is achieved in around 800k to 1000k iterations depending on the network configuration, as is shown in Fig.5-8.

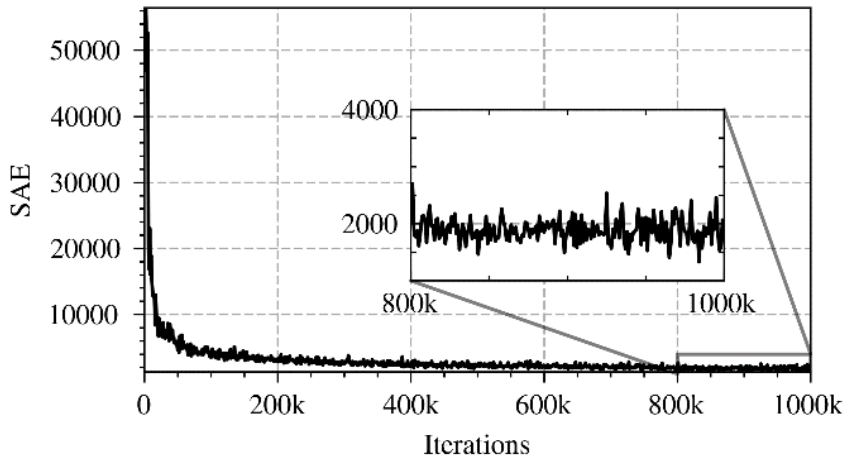

Fig. 5-8. Overview of SAE after 1000k-iteration training. The generator is the ResU-net, combined with SAE as the loss function.

Table 5-5. List of fixed parameters of the CMGs

	Parameter	Value	Unit
R_o	Outside radius of the MG	92	mm
T_{lspm}	The thickness of the PMs on the low-speed rotor	7.8	mm
T_{hspm}	The thickness of the PMs on the high-speed rotor	7.8	mm
T_s	The thickness of the modulation iron segments	13	mm
g	The length of the air gap	0.6	mm
L	Stack length	40	mm
P_{hs}	Number of pole-pairs at HS rotor	3	-
P_{ls}	Number of pole-pairs at LS rotor	22	-
N_s	Number of modulation iron segments	25	-
T_{oy}	The thickness of the yoke of the outer rotor	10	mm

T_{iy}	The thickness of the yoke of the inner rotor	3.4	mm
Ra_i	Slot open of modulation iron segment = $\theta_1/(\theta_1+\theta_2)$	0.5	-
Ra_{pm}	Ratio PM = $\theta_3/(\theta_3+\theta_4)$	0.9	-

5.6.1 Flux Density Distribution

Our model has been tested using a CMG with the parameters listed in Table V. Fig. 5-9 shows the results of predicting the magnetic field of a specific magnetic gear after using various combinations of loss functions and network structures. It can be observed that almost all the predictions are similar to the FEM solution, and the errors are hard to find visually as the mean absolute percentage error of each is less than 1%.

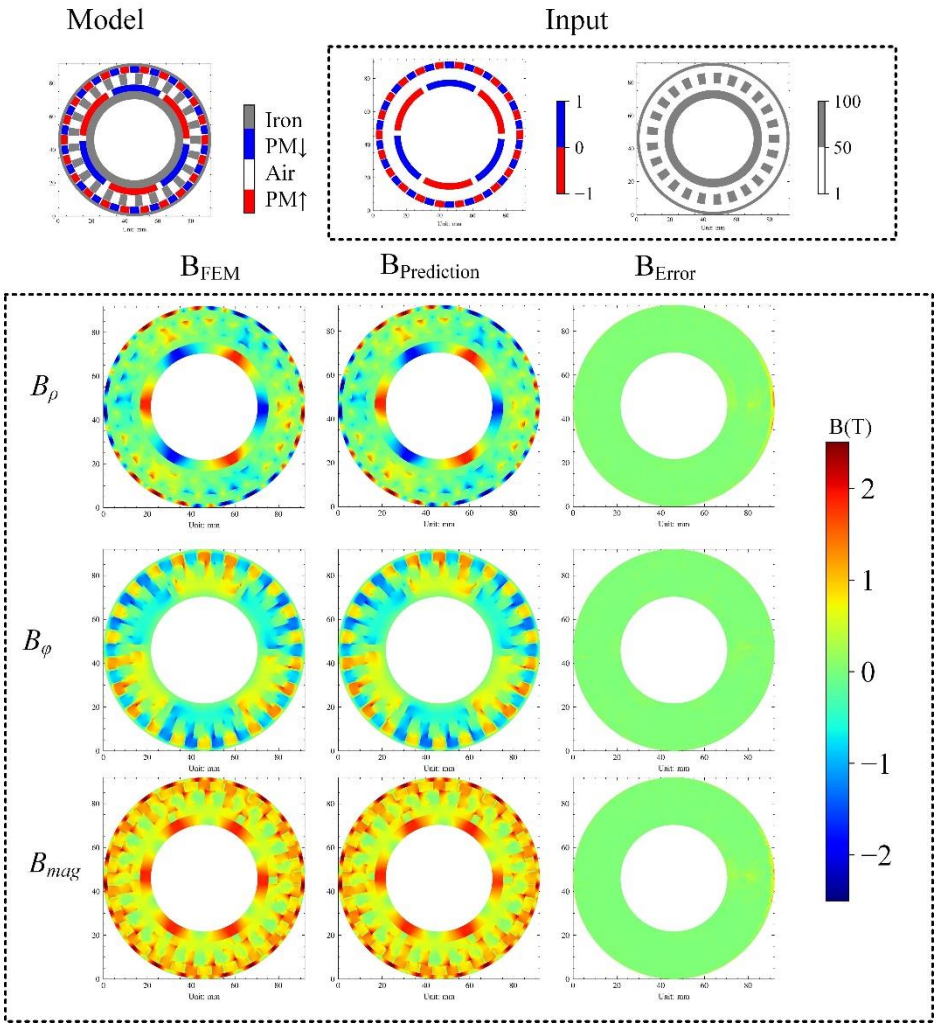

Fig. 5-9. Qualitative analysis on magnetic field prediction in the experimental 2-D setup with a generator network. The input and the predicted magnetic field of B_ρ, B_ϕ and B_{mag} are presented. Visually, our method achieves to reconstruct the magnetic field obtained by FE simulation almost perfectly.

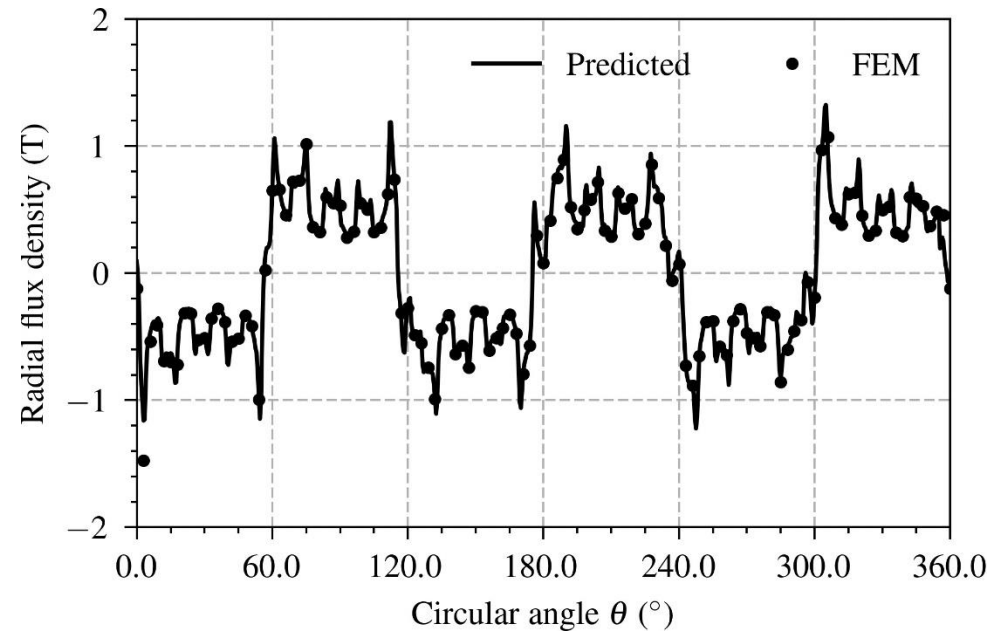

(a)

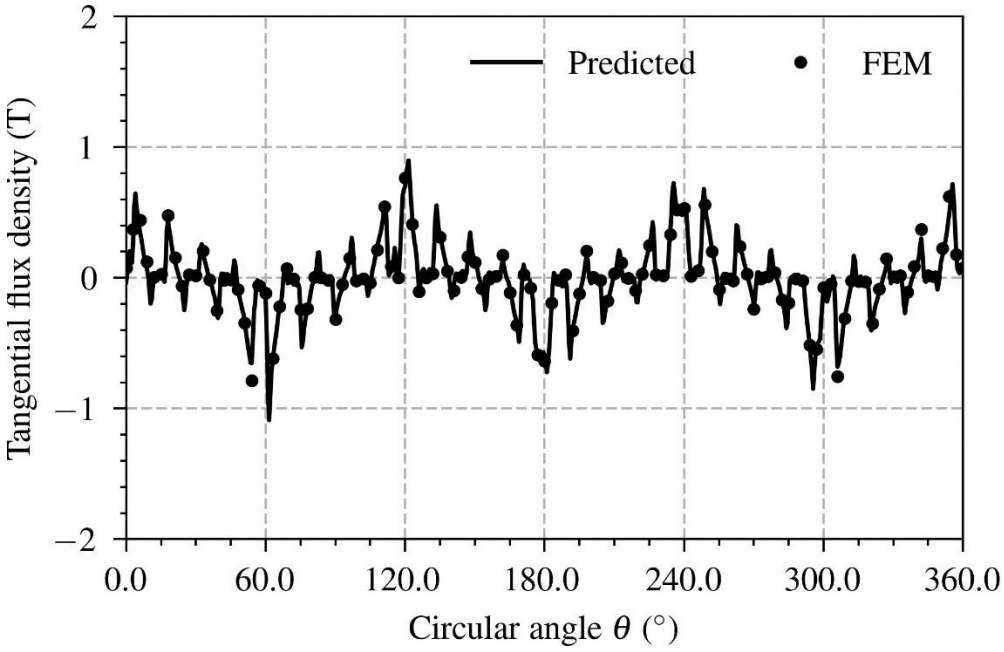

(b)

Fig. 5-10. Flux density distribution in the middle of the inner air gap (r = 66.9mm): (a) radial component and (b) tangential component.

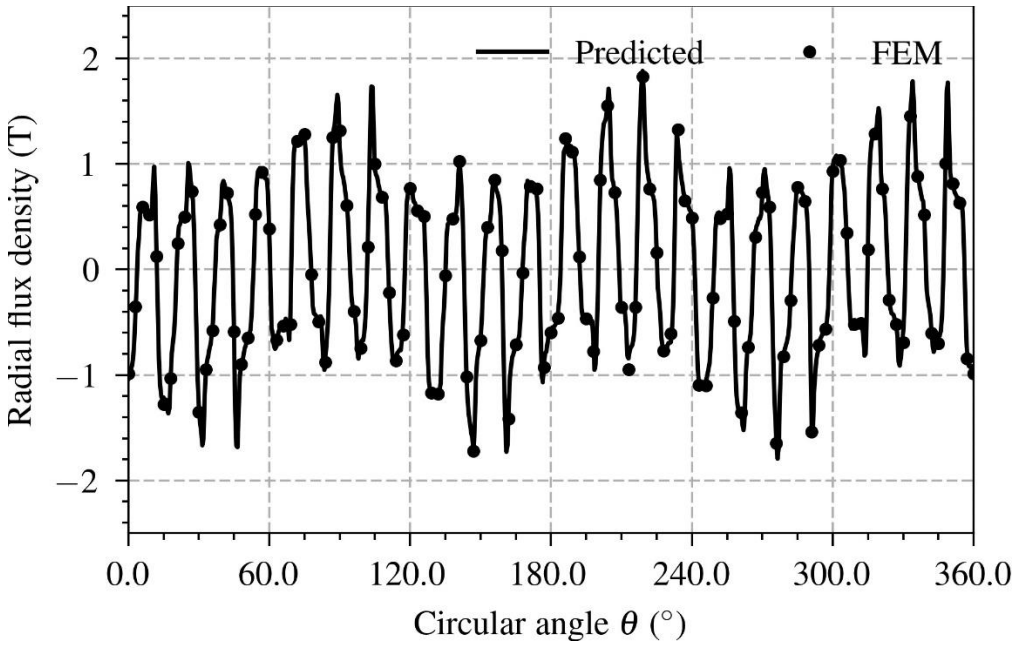

(a)

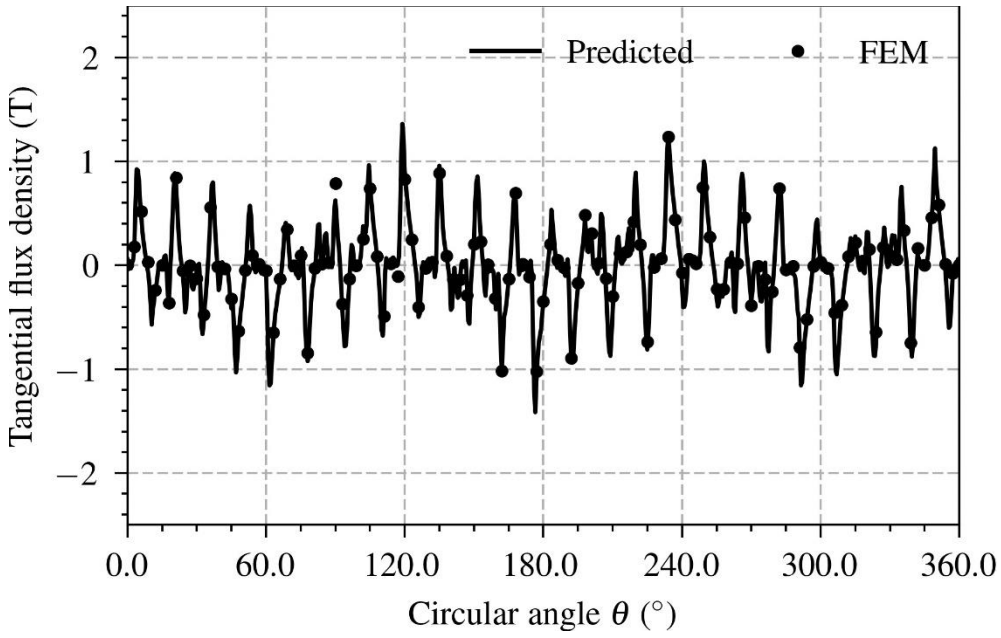

(b)

Fig. 5-11. Flux density distribution in the middle of the outer air gap (r = 80.5mm): (a) radial component and (b) tangential component.

The corresponding flux density distributions (radial and tangential components) in the middle of the inner air gap (r = 66.9mm) and in the middle of the outer air gap (r =

80.5mm) are plotted, respectively. Fig. 5-10 (a) and Fig. 5-10 (b) show the radial and tangential components of the magnetic flux density in the inner air gap of CMG. Furthermore, the radial and tangential components of the flux density distribution in the middle of the outer air gap are shown in Fig. 5-11 (a) and Fig. 5-11 (b). We can observe a very good agreement between the results predicted by our model and the results obtained from FE simulation for both radial and tangential components.

5.6.2 Torque

Fig. 5-12 shows the torque variation exerted on the inner rotor while keeping the pole-pieces ring and the outer rotor fixed. The inner rotor rotates with a phase angle varying from 0 to 120 degrees. The predicted results are in good agreement with those obtained by the FEM.

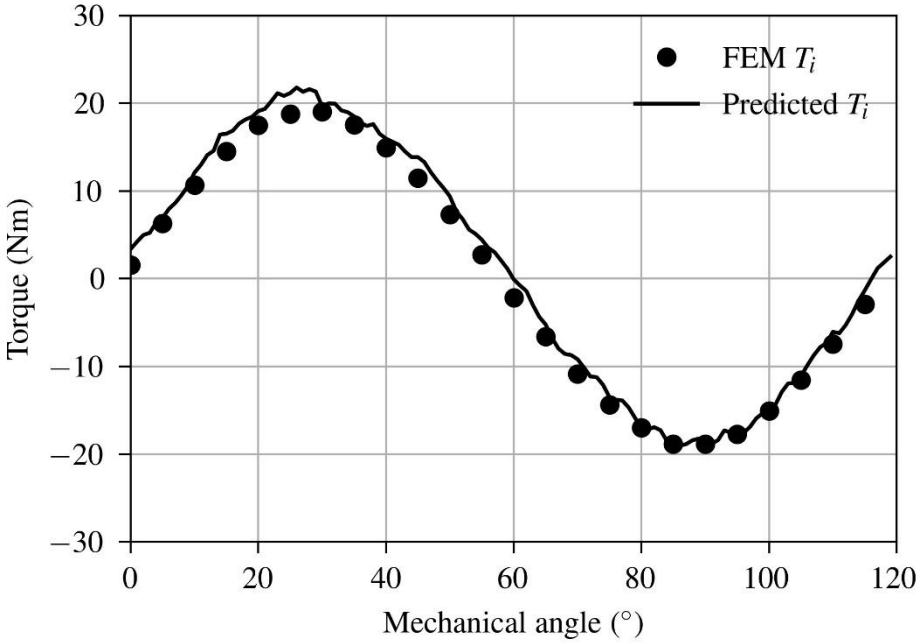

Fig. 5-12. The torque–angle curve predicted by our model (ResU-net as the generator, combined with SAE as the loss function).

5.7 Summary

This chapter proposes a fast magnetic field approximation method for CMGs using cGAN. Based on the magnetic field approximation technique in the 2-D polar coordinate system, the flux density and torque for a magnetic field produced by PMs in CMGs have been presented.

The empirical analyses showed that the cGAN model could accurately approximate the magnetic fields for CMGs, and its generalization ability is excellent, allowing various combinations of pole pairs. The predicted magnetic torque obtained by the air gap flux density and Maxwell tensor method is consistent with the FE simulation results.

In addition to improved predictive performance, our model required a significantly lower model prediction time, making neural networks more practical for adoption in optimization processes.

We note that our model performs excellent magnetic field approximation within the design space. The proposed cGAN model-based performance evaluation method can be advantageous in the real-time magnetic field approximation for the optimal design of electric machines.

Chapter 6. Physics-Informed GAN for Simulation of Electric Machines

6.1 Introduction

With the development of digital twin technology, the speed of traditional numerical calculation methods is much lower than expected, and solving physical field problems faster has become the most urgent need, especially for the optimal design of electric machines [139]–[141].

There are two main reasons for this problem in engineering, and the first is that there is no efficient algorithm implementation. The mainstream of numerical algorithms relies on iteration; hence it is almost impossible to simulate practical engineering problems in real time when the data is in a complex structure. The second reason is that numerical computing researchers in different fields are not proficient in transforming complex theories into efficient codes, resulting in many numerical calculation methods that cannot be applied well in engineering.

Many data-driven deep learning networks already lead to multi-physics simulation calculations, such as fluid field, stress, sound, and medicine. However, the application of AI in the electromagnetic field is underestimated. For example, we usually use numerical algorithms to simulate electromagnetic problems based on Maxwell equations in integral or differential form. The main algorithms include the analytical,

finite difference (FD), and finite element (FE) methods. The FE method is a general tool with a settled sequence of operations when analyzing different problems.

The FE simulation involves mesh generation, global matrix assembly, and inverse matrix solving, which is exceedingly time-consuming. On the contrary, the analytical method requires few computation resources, but its accuracy and flexibility are limited.

Therefore, we hope to use the existing electromagnetic problem dataset to promote the development of electromagnetic field approximation. Our dataset, LiM2-D, represents linear machines' two-dimension (2-D) electromagnetic field, i.e., the flux density distribution (B) of the linear machines in operation. It consists of material distribution, current density, the magnetization of permanent magnets (PMs), moving band, and flux density on the x-axis and y-axis.

The specific details are in Section 6.3. We made definitions of multiple channels for the input. Unlike the previous work, multiple channels with separated properties, such as material, vectorized magnetization field, current density direction, and motion band, achieve the dataset's scalability. Different channels of input can interact in a way that influences the prediction. Therefore, the electromagnetic field problems for a given model with appropriate channels of materials, boundaries, and source conditions over a finite region of space can be adequately solved.

Based on this dataset, some key challenges are pointed out in Section 6.5. In particular, the feasibility of dealing with large-scale problems like three-dimension (3-

D) issues is discussed. Second, a nonlinear material representation that makes the electromagnetic field approximation meet more engineering problems is concerned. Moreover, the third concern is setting boundary conditions in electromagnetic field approximation. Lastly, the integration error of prediction is conducted. Note that this chapter does not aim to thoroughly tackle these challenges but expose them to the community for future research.

Overall, our main contributions are:

a) Physics-informed loss functions.

b) A linear motor electromagnetic field dataset.

c) An in-depth study of channel definition of input and output metrics.

Some challenges faced in the electromagnetic field approximation for linear motors are highlighted, which can spark innovations in applications such as real-time electromagnetic simulation, digital twins, and optimal design for the renewable energy system.

6.2 Physics-Informed GAN

The physically informed GAN (PIGAN) is a conditional GAN. The generator can produce results almost identical to those calculated by the laws of physics through supervised learning.

The training datasets can be produced by numerical computing or measured by actual instruments. A well-trained generator can give nearly identical training results and conform to the physical properties.

For example, in Fig. 6-1, the magnetic permeability, magnetization direction, and current density of the material are used as inputs to obtain the magnetic field produced by the generator.

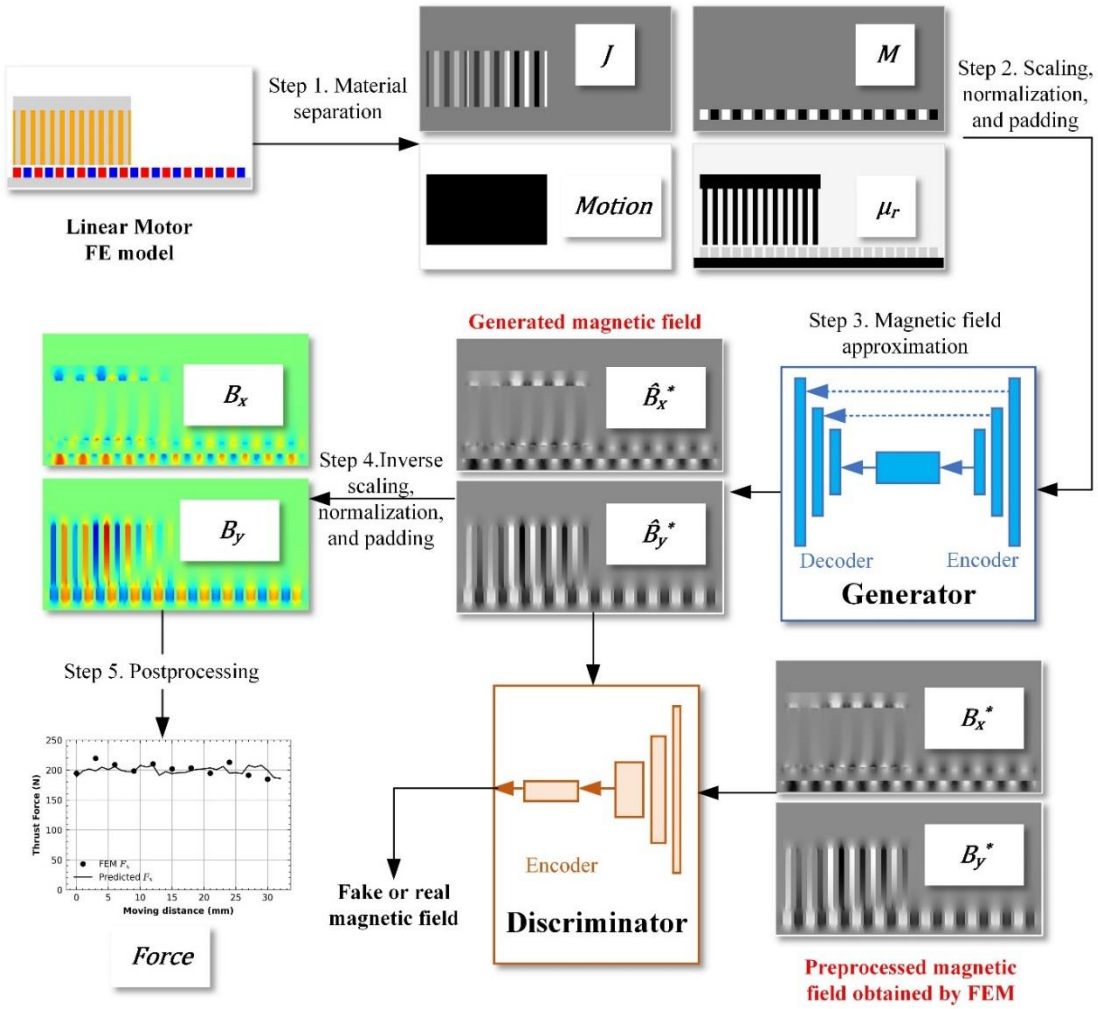

Fig. 6-1. Overview of novel DL approach for magnetic field approximation. A generator neural network is trained to predict the magnetic field values.

6.2.1 Problem definition for magnetic approximation

The induced current can be ignored for a linear motor operating at low speed; only the magneto-static problem is considered. The governing equation for the static magnetic field, including PMs, is derived from Maxwell's equations:

$$\nabla \cdot B = 0 \tag{6-1}$$

$$\nabla \times H = \nabla \times \left(\frac{1}{\mu_r \mu_0} \mathrm{B}\right) = J \tag{6-2}$$

$$B = \mu(H + M) \tag{6-3}$$

where μ_r denotes the relative magnetic permeability, μ_0 is the vacuum permeability (i.e., $4\pi \times 10^{-7} N/A^2$), B is the magnetic flux density, and B_r is the remanence of the PM material (i.e., the residual magnetic flux density), H stands for the magnetic field strength, M represents the magnetization strength of PM, and J represents the current density vector.

6.2.2 The physics-informed loss functions

This work is inspired by generative image synthesis from the research area of computer vision, where GANs are trained to synthesize the new image based on the input identified image. Ideally, the generated result $\hat{x}$ should match x0 in all the image pixels available and mimic the ground-truth full image x. Hence, a l1 loss, L_{match},

between the predicted result $\hat{x}$ and the given input image x0 and a second l1 loss is formulated:

$$L_{match} = ||x_0 - \hat{x}|| \quad (6\text{-}4)$$

For magnetic field approximation using a neural network, the rule of magnetic distribution information, i.e., Maxwell's Equation, can be embedded. The results obtained are not only numerically close to the physical results but are also bound by physical laws. By adding physical loss terms to the loss function, the proposed DL method becomes physics-informed and can be seen as a regularization for generating magnetic fields. The first physical loss term is Gauss's law for magnetism, which states that:

$$L_{div} = \nabla \cdot B = 0 \quad (6\text{-}5)$$

If we further assume the absence of electric current density J or changing electric field E over time t, Ampère's circuital law can be simplified to:

$$L_{curl} = \nabla \times B = \mu_0 J + \mu_0 \epsilon_0 \frac{\delta E}{\delta t} \quad (6\text{-}6)$$

where μ_0 is the vacuum permeability and ϵ_0 is the vacuum permittivity.

In the case of the Maxwell Stress Tensor (MST), I have to calculate the divergence of the following tensor:

$$T_{ij} = \mu_0 \left(H_i H_j - \frac{1}{2} \delta_{ij} H^2 \right) \quad (6\text{-}7)$$

With H the magnetic field given by its values in the Cartesian frame (x, y, z) $H\left(H_x H_y H_z\right)$. δ_{ij} is the Kronecker sign (δ_{ij} =1 if i=j otherwise δ_{ij} = 0).

The Maxwell Stress Tensor (MST) is performed by calculating of the force using a surface integration on Γ', over a D' domain. The force can be obtained using the following formula:

$$\begin{aligned} L_{MST} &= \int_D div\, T\, dv \\ &= \oint_\Gamma \mu_0 \left((H.n)H - \tfrac{1}{2}|H|^2 n \right) ds \end{aligned} \quad (6\text{-}8)$$

The vector n is the normal on the surface Γ'. The MST method presents several advantages:

- Linear or nonlinear cases can be evaluated.
- The choice of surface integration is undistinguished.
- Only one part of the mesh is concerned.

Our final loss function used during training is formulated as follows:

$$\begin{aligned} L = \lambda_{EMGAN} L_{EMGAN} + \lambda_{match} L_{match} + \lambda_{div} L_{div} \\ + \lambda_{curl} L_{curl} + \lambda_{MST} L_{MST} \end{aligned} \quad (6\text{-}9)$$

where λ_{EMGAN}, λ_{match}, λ_{div}, λ_{curl} and λ_{force} are the penalty coefficients for each single loss term and define their relative importance.

6.3 The Linear Electric Machine Dataset

This section describes the definition of the 2-D electromagnetic field approximation problem, the generation process, and the dataset's input. Unlike other datasets directly using pre-defined parameters, our dataset is a field-based dataset with multiple channels.

6.3.1 The PMLSM Model

To evaluate the nonlinear material property in the proposed method, we consider a permanent magnet linear synchronous machine (PMLSM) in this study. The geometry of PMLSM is shown in Fig. 6-2, the core material is Electrical Steel DW310 for simulation, and the nonlinear B–H curve is shown in Fig. 6-3.

Three-dimensional parameters, namely, the width of edge (We), the width of slot (Ws), the width of teeth (Wt), and the height of slot (h1), are chosen as the geometry design variables. In addition, the input current also varies from 1A to 16A.

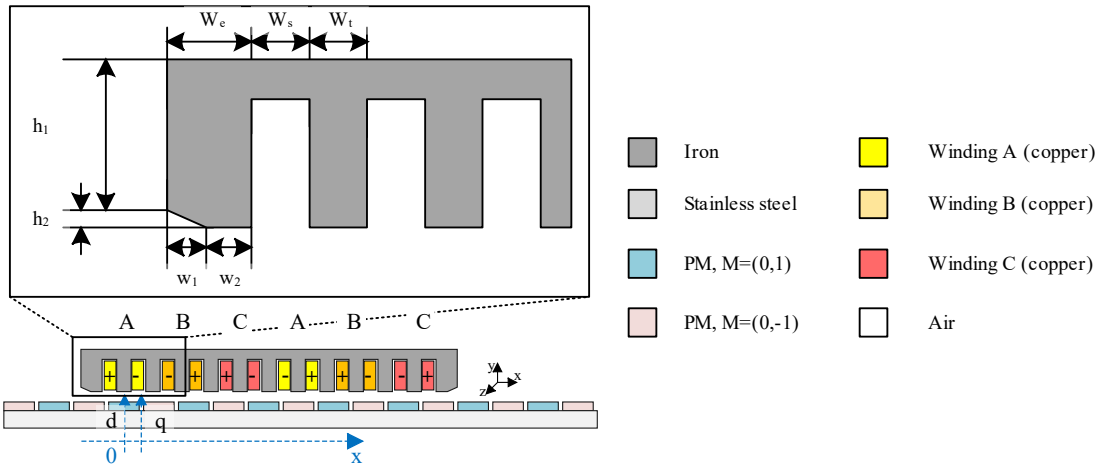

Fig. 6-2. Cutting view of the whole PMLSM

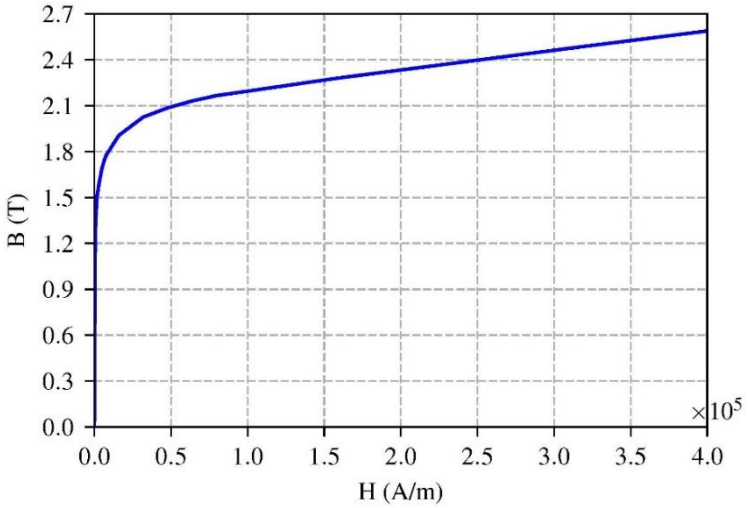

Fig. 6-3. Nonlinear B-H curve of stator material in PMLSM FE model.

6.3.2 Definition of Physics-based Channels

The definitions of each channel are based on two criteria. 1) Each channel should have a clear and unambiguous physical meaning, and it should consist of the component in each axis or direction if the property is a vector, such as 2 channels for a 45-degree magnetization vector M = (1, 1) in 2-D problem, 3 channels for a z-direction current density $J = (0, 0, 2 \times 10^6\ A/m^2)$ in 3-D problem. 2) Different channels should

have significant variance in terms of geometric structure or property. I identify these four types of channels in the dataset, as listed below. Figure 6-1 shows the examples of our annotations.

Current density – The applied current excitation of the linear motor will be converted to the current density, which is applied to the material based on the size of the mesh grid. The number of channels of current density is one in the 2-D problem and 3 in the 3-D problem.

Magnetic materials – The relative permeability of magnetic material is close to one, and this material involves channels for the magnetization direction vector. The magnetization will have two channels in the 2-D problem and three channels in the 3-D problem. We will only add one channel if the magnetization is in one direction.

Motion band – The moving part will be marked as one, and the materials and approximated fields inside the moving band will be extracted after approximation. The number of channels of motion band is one.

Permeable materials – The relative permeability of this kind of material is more significant than one and does not have a magnetization direction vector. The number of channels of permeable material is one if the material is isotropic. Anisotropy material will have two channels in the 2-D problem and three channels in the 3-D problem.

6.3.3 Generating Linear Machine Models

A 2-D PM linear motor model is selected in this study. The model consists of a series of initial condition setups. All initial conditions are implemented as the network input, including the relative magnetic permeability μr, the magnetization direction of PMs, and the current source defined in the excitation matrix. Since the input is more like a matrix, all input is determined based on density, i.e., the current (I, unit is Ampere) is converted to current density (J, unit is A/mm^2)

Then the physical properties of the field are sampled using the FE software to simulate the field and then extract the data from the solution with a structured mesh grid. An example of a test dataset is shown in Table 6-1. The three columns indicate the transient status of a linear motor when it moves at the speed of 1mm/s from the start point to the endpoint. Each column contains all status of the linear motor at a specified time. The first four rows are pre-processed input, and the last two rows are the FE solutions without scaling.

Table 6-1. Examples of our test dataset.

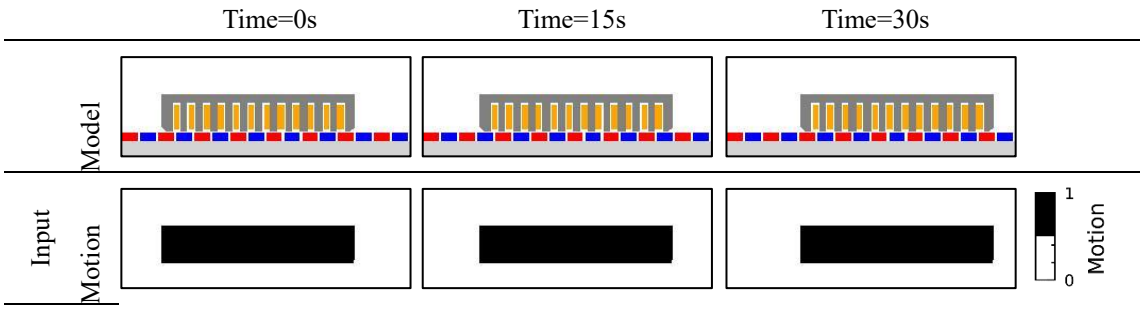

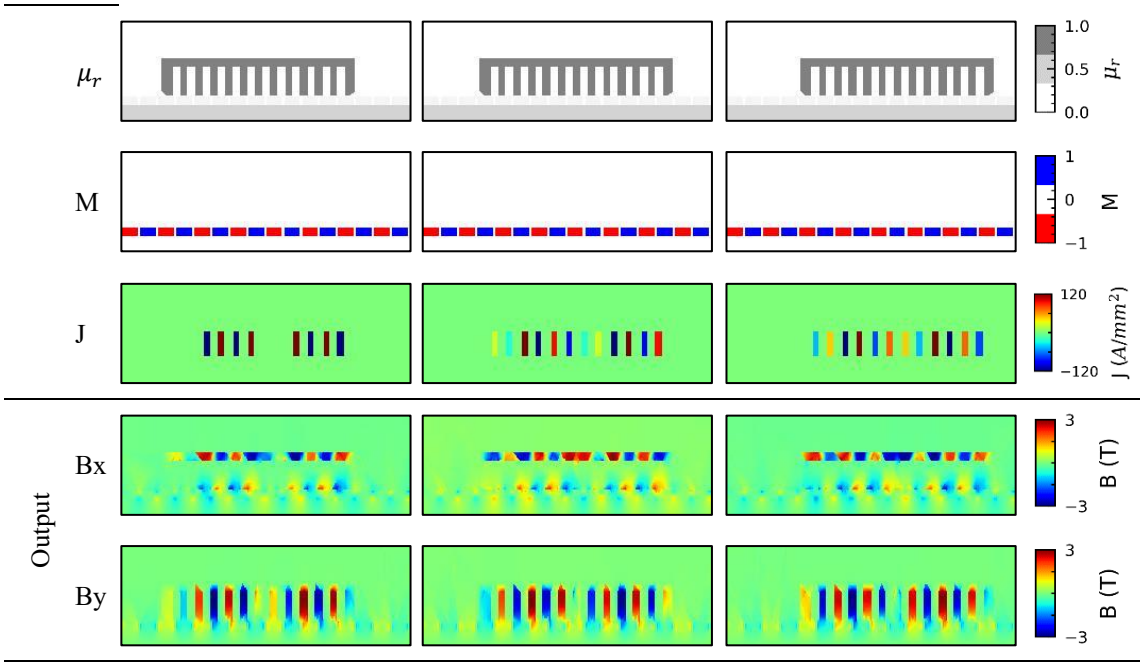

6.4 Results

6.4.1 Evaluation Metrics

Two types of evaluation metrics are considered in this study, including image synthesis metrics and Electromagnetic metrics.

6.4.1.1 Image Synthesis Metrics:

There are no existing metrics for electromagnetic field synthesis. To objectively demonstrate the superiority of the proposed method, we quantitatively evaluated all the experiments using the structural similarity (SSIM) index and the peak signal-to-noise ratio (PSNR). The SSIM index measures the similarity of structural information in two images, where zero indicates no similarity and 1 shows total positive similarity. PSNR

measures image distortion and noise level between two images. A higher PSNR value indicates a higher image quality. SSIM can be used in physics-based image restoration [138], [142], [143], and a higher SSIM index means that the synthetic fundus image is more close to the real one.

6.4.1.2 Electromagnetic Metric

Magnetic force is one of the most critical performance indicators of linear motors. It can be obtained by flux density. Flux density distribution in the air gap generally reveals the performance of force ripple and the order of harmonics of the electric machines. The high-order harmonics will increase cogging force and the eddy current loss. Besides, the air-gap flux density is one of the most critical parameters to optimize when designing permanent magnet (PM) devices. During the PM device design stage, the air-gap flux density is typically derived from simulations. Therefore, it is an inevitable metric while designing a PM device. In LiM2-D, the air gap flux density can be obtained by motion band.

After determining the magnetic field distribution in the Cartesian coordinate system, the force applied to the mover in the x direction and y direction F_x and F_y can be obtained by using the Maxwell Stress Tensor (MST) method, and is given by:

$$F_x = \frac{L}{\mu 0}\int_{gap} B_x(x_{air}, y_{air})B_y(x_{air}, y_{air})dx \qquad (6\text{-}10)$$

$$F_y = \frac{L}{2\mu 0}\int_{gap}\left[B_y(x_{air}, y_{air})^2 - B_x(x_{air}, y_{air})^2\right]dx \qquad (6\text{-}11)$$

6.4.2 Predicted results of linear machine

The investigated PMLSM is a flat iron core LMG10-050 from ETEL. Table 2-1 lists the performance of the PMLSM. This linear motor is a one-pole pair structure with a pole pitch τ_p = 16mm, and a force constant K_t of 88.8N/A. The air gap thickness is about 0.8mm, and the NdFeB permanent magnets have a residual flux density of approximately 1.23Tesla.

Table 6-2. Comparative study of magnetic field approximation for simulation of the test linear machine using FEM, Pix2Pix and proposed PIGAN

	Current(A)	FEM	Prediction	
			Pix2Pix	PIGAN
Continuous force (N)	2.23A	190	150	192
Peak force (N)	15A	950	800	980
Detent force (N)	-	12	35	20

It can be found in Fig. 6-4, Fig. 6-5, and Fig. 6-6 that the results using Pix2Pix have a higher loss in MAE, PSNR, and SSIM than that of the proposed model. Also, it can be observed that the employment of the proposed model predicts with higher precision.

The training of our final model takes 15 hours for 200k iterations. As for the evaluation process, the total magnetic field approximation time of the 30-step PMLSM model using the proposed PIGAN is 1 second; each step costs 33.3 ms on average. In comparison, the conventional 30-step FE simulation takes 45 seconds, and each step takes 1.5 seconds on average. Convergence is achieved in around 150k to 200k iterations depending on the network configuration, as is shown in Fig. 6-4, Fig. 6-5, and Fig. 6-6.

In addition, magnetic force can be obtained by calculating the integral of radial component times tangential component of flux density using the Maxwell Stress Tensor (MST) (c.f. (6-10) and (6-11)). It helps minimize the physics-informed loss function between the prediction and the ground truth and can quickly find the optimal model.

Fig. 6-9 shows the torque variation exerted on the mover while the current is 2.23 Arms. Fig. 6-12 displays the torque variation exerted on the mover while the current is 15.5 Arms. The mover translates toward a positive direction on X-axis from 0mm to 30mm. The predicted results are in good agreement with those obtained by the FEM.

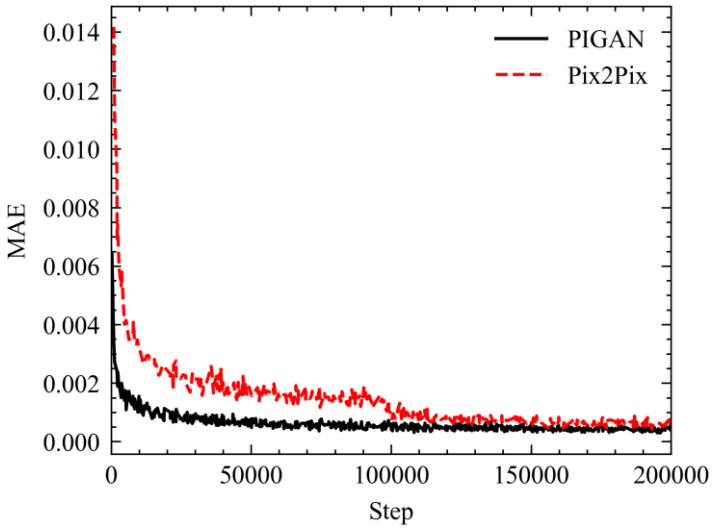

Fig. 6-4. The MAE loss curve of PIGAN and Pix2Pix.

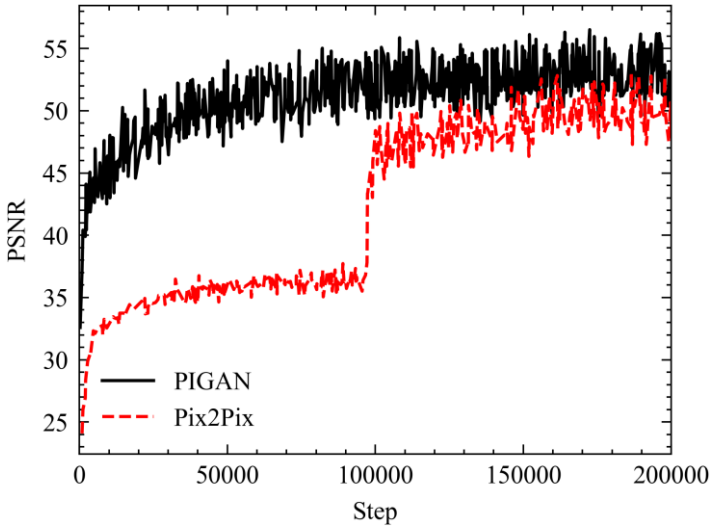

Fig. 6-5. The PSNR curve of PIGAN and Pix2Pix.

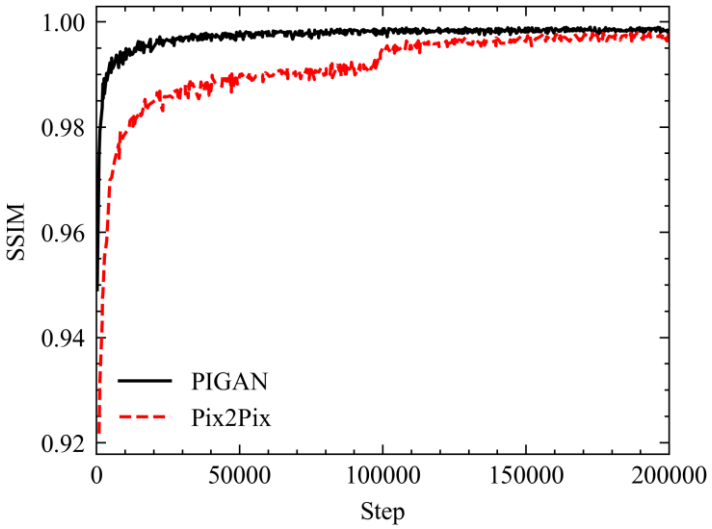

Fig. 6-6. The SSIM curve of PIGAN and Pix2Pix.

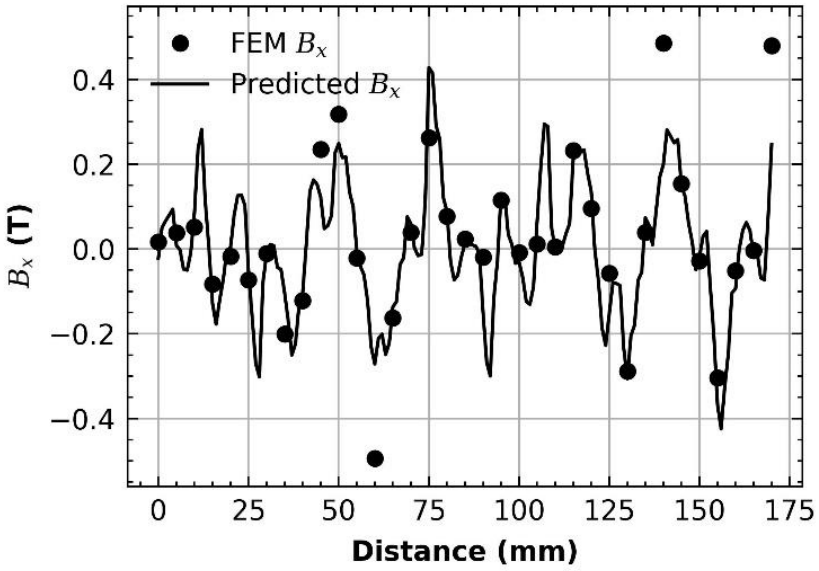

Fig. 6-7. The prediction and FEM results of x-axis air gap flux density when PMLSM works with continuous current.

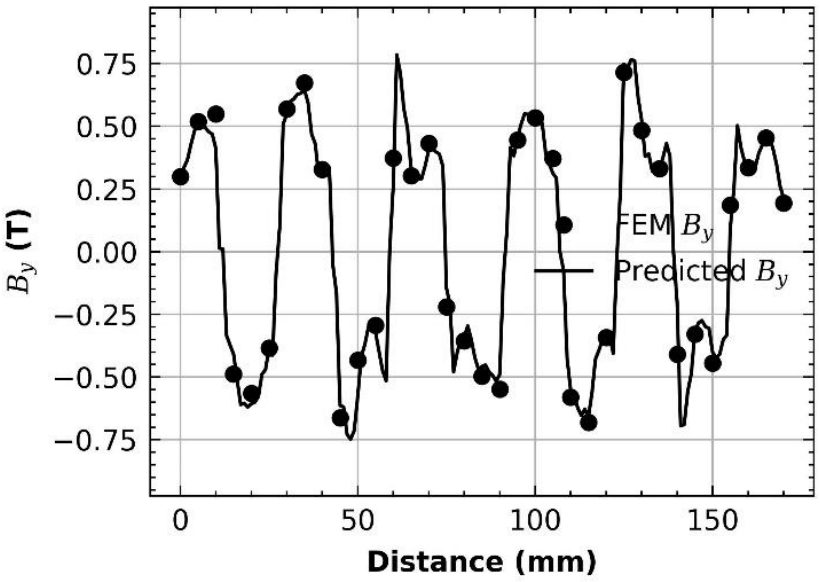

Fig. 6-8. The prediction and FEM results of y-axis air gap flux density when PMLSM works with the continuous current.

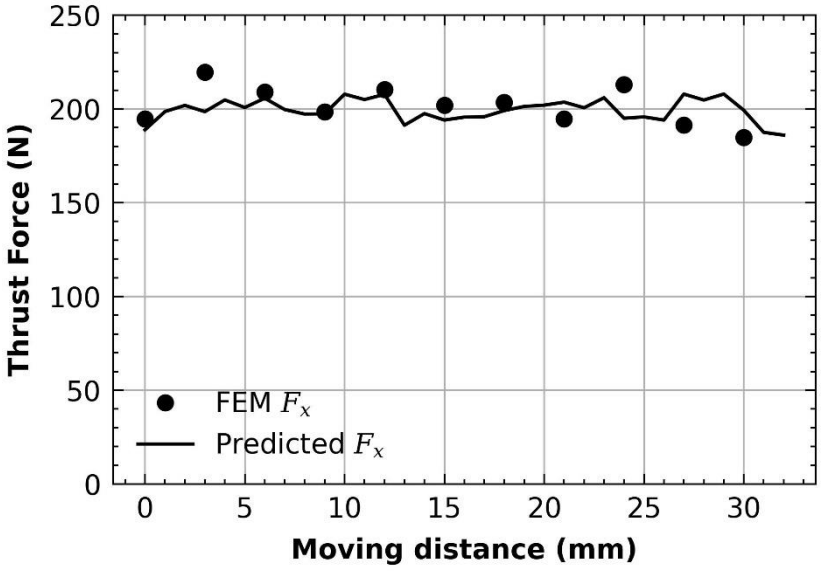

Fig. 6-9. The prediction results and FEM results of thrust force when PMLSM works with the continuous current.

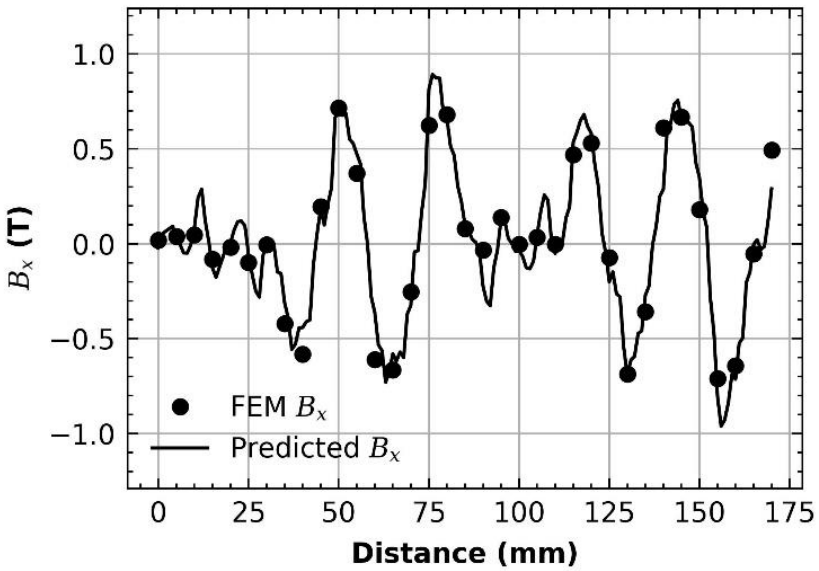

Fig. 6-10. The prediction and FEM results of x-axis air gap flux density when PMLSM works with peak current.

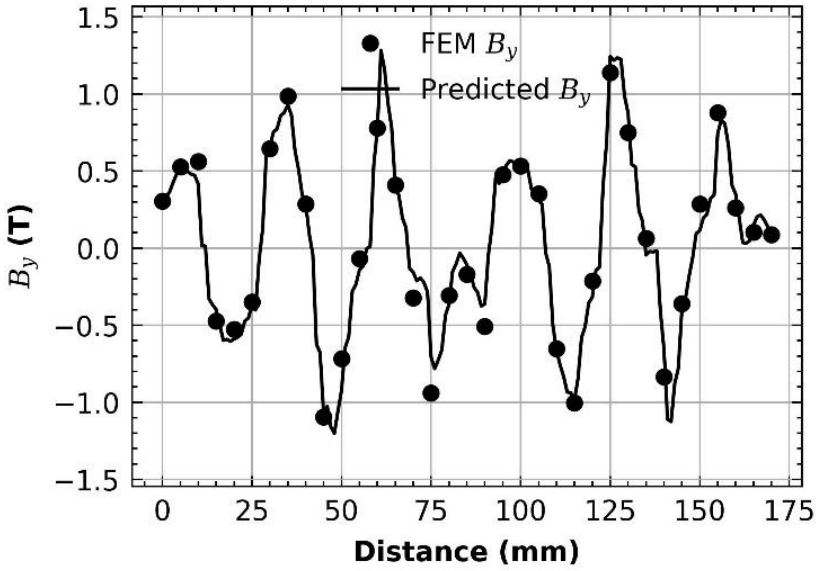

Fig. 6-11 The prediction and FEM results of y-axis air gap flux density when PMLSM works with peak current.

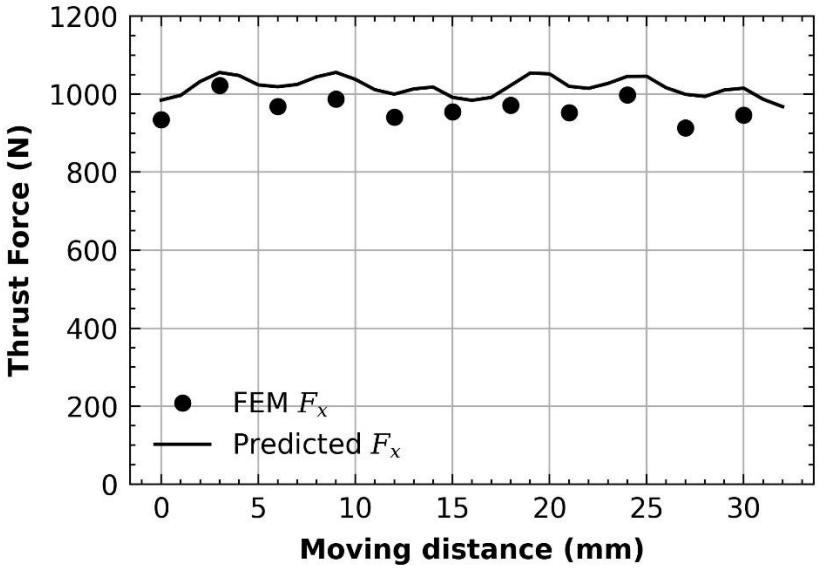

Fig. 6-12 The prediction and FEM results of thrust force when PMLSM works with peak current.

6.5 Challenges

In this section, several critical challenges revealed by our dataset are identified. Then the possible solutions are proposed to overcome the obstacles, eventually improving the performance of electromagnetic field approximation. Note that this section is not aiming to offer new algorithms. Instead, it is trying to generalize the existing pipelines from the perspective of dataset characteristics.

6.5.1 3-D Problem

For 3-D problems, the input size is at least several hundred times larger than 2-D problems. Suppose the 3-D model with structured mesh and its electromagnetic field is approximated using the image synthesis method. In this case, only the newly added axis

will cause the number of input variables to increase by several hundred times, and the number of channels will also increase.

For example, if the axis of input of a 2-D problem is [100, 512, 512, 4], then the equivalent input of the 3-D model is [100, 512, 512, 512, 6] if the length of the z-axis is 512, and two 2-D channels are converted to 3-D channels. Moreover, as for anisotropic material properties, the 3-D problem will be more complicated

In the future, it is suggested that 3-D problems can be processed as 3-D mesh segmentation or point cloud processing instead of using structured grids like pictures. The data structure will also be more complicated. It is necessary to arrange the input data structure and memory location reasonably. If it is heterogeneous computing, it is essential to consider sharing the same memory instead of the existing time-consuming and complex algorithms such as copying the memory data to the video memory.

6.5.2 Materials

Nonlinear electromagnetic material is widely used, and researchers have deeply investigated the characteristic for decades. The nonlinear material properties that need to be considered will increase the number of input channels.

In addition, nonlinear materials require proprietary databases and formulas for fitting queries. As for anisotropic materials, the material in each direction can be vectorized. The material property makes it more complicated in data preprocessing. If

a multi-physics problem is considered, the model's input will change because the input dimension, such as the channels, will be added, leading the model to be retrained.

6.5.3 Boundary conditions

Boundary conditions (b.c.) are constraints necessary to solve a boundary value problem. The significant influence of b.c. is that the input and output of the dataset cannot be cropped simply without the b.c. Our dataset uses the Dirichlet boundary condition, and the value is determined to be zero. Therefore, the initial b.c. channels are neglected in the input.

If a non-zero b.c. is considered, the channels should be added, making the problem even more complex. Some preliminary results [144] show that image inpainting techniques from computer vision can be beneficial to this issue.

6.5.4 Integration error

When calculating the magnetic torque, the integration will be performed, which will enlarge the total error even if the error of each point is small. For example, the concepts of force and torque using MST method in the electromagnetic field require producing and integrating the alternating magnetic field near the moving object, and the calculation error rises extremely fast.

Furthermore, 64-bit floating numbers (FP64) for scientific calculation are pretty common, while machine learning algorithms use 16-bit (FP16) or 32-bit (FP32) floating

numbers. The cost-performance ratio would be extremely low if the dedicated hardware trains the model.

6.6 Summary

In this chapter, a PIGAN for electromagnetic field approximation is introduced. The proposed method of generating FE model data and defining input channels achieves better electromagnetic field approximation accuracy. A physics-informed loss function outperforms the naive benchmark models through extensive benchmarking, improving forecasting performance.

Moreover, several open challenges are highlighted, including 3-D problems for electromagnetic field approximation, material property consideration, and integration error in fundamental performance estimation.

Additionally, PIGAN, as a neural network, has a standard development process. The standardized development process can significantly reduce the difficulty of software development, and it will be easier to put PIGAN into industrial applications than FE solvers. With the accumulation of data, PIGAN can evolve itself to improve its computational accuracy further. Hopefully, PIGAN can be a steppingstone towards advancing research in related areas.

Chapter 7. Conclusions

7.1 Summary and contribution

Topology optimization is a powerful tool for the optimal design of electric motors, especially for the rotor design. This section summarizes essential contributions in this thesis.

First, the study extends the limited research on topology optimization using the multi-objective genetic algorithm and its application in the optimal design of synchronous reluctance motors. A TO tool based on FE computation and a multi-objective optimization framework are developed. Meanwhile, a bitmap-encoded genetic algorithm for topology optimization is proposed. A SynRM with a complex structure was used for testing. The study employs a gaussian filter to remove the small parts in the topology matrix, thus reducing the computation time and making the optimized candidate model feasible.

Second, no previous study has explored the impact of using the vectorized model for FE simulation in the topology optimization of the asymmetric rotor of electric motors. This study proposes a novel topology optimization algorithm, including considering the control strategy, using MPTA, and using high-resolution interpolation and edge-smoothing methods. Despite the increased computational time of the model,

the research shows that results obtained with the help of the vectorized CAD model during the TO can increase the optimized model's performance.

Third, existing research on objective function evaluation methods of topology optimization of electric motors has primarily focused on FE simulation other than other methods. This study is one of the earlier studies to assess deep learning and its impact on employing AI in the objective function evaluation method. Generative networks are used for fast electromagnetic field approximation to reduce the motor's computation time. Novel network structure and several loss functions are employed, including those based on physical information. The results show that the proposed PIGAN can significantly reduce the calculation time while maintaining high precision.

7.2 Recommendations for future research

This research comprehensively studies TO applications for electric motors using the multi-objective evolutionary algorithms and the PIGAN. However, due to the limited time, the study has not combined the proposed PIGAN based on deep learning and the TO framework to optimize the electric motor. Therefore, further research can be studied in the future.

Firstly, research on combining multi-objective multi-physics topology optimization is necessary and worthwhile. Multi-physics, such as combined thermal, mechanical, and electromagnetic TO for electric machines, remains challenging.

Previous studies consider these problems separately and assume initial/final conditions associated with both these problems. These assumptions can result in a loss of optimality and flexibility to expose tradeoffs.

Secondly, a computationally efficient, PIGAN-based electromagnetic field solver can be developed to accelerate the speed of electric machine multi-physics topology optimization. As far as electric machines are concerned, the moving parts make the equivalent FE model time-consuming for multi-step simulation. An AI-based solver like PIGAN can dramatically reduce computation time, making multi-physics topology optimization feasible.

Finally, a prototype machine can be rigorously manufactured and tested to verify the final optimized IPM motor model obtained by the proposed high-resolution interpolation and edge-smoothing method.

References

[1] O. US EPA, “Explaining Electric & Plug-In Hybrid Electric Vehicles,” Aug. 17, 2015. https://www.epa.gov/greenvehicles/explaining-electric-plug-hybrid-electric-vehicles (accessed Aug. 02, 2022).

[2] T. V. Frandsen *et al.*, “Motor Integrated Permanent Magnet Gear in a Battery Electrical Vehicle,” *IEEE Trans. Ind. Appl.*, vol. 51, no. 2, pp. 1516–1525, 2015, doi: 10.1109/TIA.2014.2360016.

[3] J. Hou, X. Wu, K. Chen, and Y. Dong, “A direct optimization strategy based on field synergy equation for efficient design of battery thermal management system,” *Int. J. Heat Mass Transf.*, no. xxxx, p. 122304, 2021, doi: 10.1016/j.ijheatmasstransfer.2021.122304.

[4] “Japan may ban sales of new ICE vehicles in mid-2030s, report says | Automotive News Canada.” https://canada.autonews.com/electric-vehicles/japan-may-ban-sales-new-ice-vehicles-mid-2030s-report-says (accessed Aug. 16, 2022).

[5] N. Winton, “Greens Laud New EU ICE Ban, But Manufacturers Demand Fast Charger Action,” *Forbes*. https://www.forbes.com/sites/neilwinton/2022/06/29/greens-laud-new-eu-ice-ban-but-manufacturers-demand-fast-charger-action/ (accessed Aug. 16, 2022).

[6] S. Liu, Q. Li, J. Liu, W. Chen, and Y. Zhang, “A Realization Method for Transforming a Topology Optimization Design into Additive Manufacturing Structures,” *Engineering*, vol. 4, no. 2, pp. 277–285, 2018, doi: 10.1016/j.eng.2017.09.002.

[7] T. Pham, P. Kwon, and S. Foster, “Additive Manufacturing and Topology Optimization of Magnetic Materials for Electrical Machines—A Review,” *Energies*, vol. 14, no. 2, p. 283, Jan. 2021, doi: 10.3390/en14020283.

[8] J. Zhu, H. Zhou, C. Wang, L. Zhou, S. Yuan, and W. Zhang, “A review of topology optimization for additive manufacturing: Status and challenges,” *Chin. J. Aeronaut.*, vol. 34, no. 1, pp. 91–110, Jan. 2021, doi: 10.1016/j.cja.2020.09.020.

[9] G. Allaire, L. Cavallina, N. Miyake, T. Oka, and T. Yachimura, “The homogenization method for topology optimization of structures: old and new.” arXiv, Jun. 14, 2019. Accessed: Aug. 14, 2022. [Online]. Available: http://arxiv.org/abs/1901.09336

[10] Y. Okamoto, R. Hoshino, S. Wakao, and T. Tsuburaya, “Improvement of torque characteristics for a synchronous reluctance motor using MMA-based topology optimization method,” *IEEE Trans. Magn.*, vol. 54, no. 3, pp. 1–4, 2018, doi: 10.1109/TMAG.2017.2762000.

[11] H. A. Eschenauer and N. Olhoff, “Topology optimization of continuum structures: A review*,” *Appl. Mech. Rev.*, vol. 54, no. 4, pp. 331–390, Jul. 2001, doi: 10.1115/1.1388075.

[12] O. Sigmund and K. Maute, “Topology optimization approaches: A comparative review,” *Struct. Multidiscip. Optim.*, vol. 48, no. 6, pp. 1031–1055, Dec. 2013, doi: 10.1007/s00158-013-0978-6.

[13] H. A. Eschenauer, V. V. Kobelev, and A. Schumacher, “Bubble method for topology and shape optimization of structures,” *Struct. Optim.*, vol. 8, no. 1, pp. 42–51, Aug. 1994, doi: 10.1007/BF01742933.

[14] J. Rodriguez and A. A. Seireg, “Algorithmic rule-based methodology for shape synthesis: 2D cases,” *Comput.-Aided Des.*, vol. 24, no. 8, pp. 411–424, Aug. 1992, doi: 10.1016/0010-4485(92)90009-Y.

[15] B. Lequesne and E.-M. Consulting, “Electric machines for automotive propulsion: History and future,” p. 28.

[16] T. A. Burress *et al.*, “Evaluation of the 2010 Toyota Prius Hybrid Synergy Drive System,” ORNL/TM-2010/253, 1007833, Mar. 2011. doi: 10.2172/1007833.

[17] T. Burress, “Electrical Performance, Reliability Analysis, and Characterization,” p. 25.

[18] S. Bakker, “Tesla Model 3 Powertrain Fun. From Carburetors To Carborundum. You’ve Come A Long Way, Baby!,” *CleanTechnica*, May 28, 2018. https://cleantechnica.com/2018/05/28/more-tesla-model-3-powertrain-fun-from-carburetors-to-carborundum-youve-come-a-long-way-baby/ (accessed Aug. 22, 2022).

[19] T. Jahns, “Getting Rare-Earth Magnets Out of EV Traction Machines: A review of the many approaches being pursued to minimize or eliminate rare-earth magnets from future EV drivetrains,” *IEEE Electrification Mag.*, vol. 5, no. 1, pp. 6–18, Mar. 2017, doi: 10.1109/MELE.2016.2644280.

[20] E. Agamloh, A. von Jouanne, and A. Yokochi, “An overview of electric machine trends in modern electric vehicles,” *Machines*, vol. 8, no. 2, pp. 1–17, 2020, doi: 10.3390/MACHINES8020020.

[21] M. P. Bendsøe and N. Kikuchi, “Generating optimal topologies in structural design using a homogenization method,” *Comput. Methods Appl. Mech. Eng.*, vol. 71, no. 2, pp. 197–224, Nov. 1988, doi: 10.1016/0045-7825(88)90086-2.

[22] M. P. Bendsøe, “Optimal shape design as a material distribution problem,” *Struct. Optim.*, vol. 1, no. 4, pp. 193–202, Dec. 1989, doi: 10.1007/BF01650949.

[23] L. Lamberti and C. Pappalettere, “Comparison of the numerical efficiency of different sequential linear programming based algorithms for structural optimisation problems,” *Comput. Struct.*, vol. 76, no. 6, pp. 713–728, Jul. 2000, doi: 10.1016/S0045-7949(99)00185-6.

[24] P. D. Dunning and H. A. Kim, “Introducing the sequential linear programming level-set method for topology optimization,” *Struct. Multidiscip. Optim.*, vol. 51, no. 3, pp. 631–643, Mar. 2015, doi: 10.1007/s00158-014-1174-z.

[25] K. Svanberg, “MMA and GCMMA – two methods for nonlinear optimization,” p. 15.

[26] J. Yoo and N. Kikuchi, “Topology optimization in magnetic fields using the homogenization design method,” *Int. J. Numer. Methods Eng.*, vol. 48, no. 10, pp. 1463–1479, Aug. 2000, doi: 10.1002/1097-0207(20000810)48:10<1463::AID-NME952>3.0.CO;2-5.

[27] J. S. Choi and J. Yoo, “Structural optimization of ferromagnetic materials based on the magnetic reluctivity for magnetic field problems,” *Comput. Methods Appl. Mech. Eng.*, vol. 197, no. 49–50, pp. 4193–4206, Sep. 2008, doi: 10.1016/j.cma.2008.04.019.

[28] O. Sigmund, “On the usefulness of non-gradient approaches in topology optimization,” *Struct. Multidiscip. Optim.*, vol. 43, no. 5, pp. 589–596, May 2011, doi: 10.1007/s00158-011-0638-7.

[29] E. Sayed, M. H. Bakr, B. Bilgin, and A. Emadi, “Adjoint-Based Design Optimization of Nonlinear Switched Reluctance Motors,” *Electr. Power Compon. Syst.*, vol. 47, no. 19–20, pp. 1705–1716, Dec. 2019, doi: 10.1080/15325008.2020.1731864.

[30] C. Lee and I. G. Jang, “Topology Optimization Framework for Simultaneously Determining the Optimal Structural Design and Current Phase Angle of the IPMSMs for the MTPA Control,” *IEEE Trans. Ind. Electron.*, pp. 1–1, 2022, doi: 10.1109/TIE.2022.3174240.

[31] K.-T. Zuo, L.-P. Chen, Y.-Q. Zhang, and J. Yang, “Study of key algorithms in topology optimization,” *Int. J. Adv. Manuf. Technol.*, vol. 32, no. 7, pp. 787–796, Apr. 2007, doi: 10.1007/s00170-005-0387-0.

[32] K. Svanberg, “The method of moving asymptotes—a new method for structural optimization,” *Int. J. Numer. Methods Eng.*, vol. 24, no. 2, pp. 359–373, 1987, doi: 10.1002/nme.1620240207.

[33] F. Guo and I. P. Brown, “Simultaneous Magnetic and Structural Topology Optimization of Synchronous Reluctance Machine Rotors,” *IEEE Trans. Magn.*, vol. 56, no. 10, 2020, doi: 10.1109/TMAG.2020.3014289.

[34] A. Manninen, J. Keränen, J. Pippuri-Mäkeläinen, S. Metsä-Kortelainen, T. Riipinen, and T. Lindroos, *Topology Optimization for Additive Manufacturing of Switched Reluctance Machines*. 2018.

[35] A. N. A. Hermann, N. Mijatovic, and M. L. Henriksen, "Topology optimisation of PMSM rotor for pump application," in *2016 XXII International Conference on Electrical Machines (ICEM)*, Sep. 2016, pp. 2119–2125. doi: 10.1109/ICELMACH.2016.7732815.

[36] C. Lee, J. Lee, and I. G. Jang, "Topology Optimization for the Manufacturable and Structurally Safe Synchronous Reluctance Motors with Multiple Iron Webs and Bridges," *IEEE Trans. Ind. Electron.*, pp. 1–1, 2022, doi: 10.1109/TIE.2022.3148751.

[37] S. Osher and J. A. Sethian, "Fronts propagating with curvature-dependent speed: Algorithms based on Hamilton-Jacobi formulations," *J. Comput. Phys.*, vol. 79, no. 1, pp. 12–49, 1988.

[38] J. A. Sethian and P. Smereka, "Level Set Methods for Fluid Interfaces," *Annu. Rev. Fluid Mech.*, vol. 35, no. 1, pp. 341–372, Jan. 2003, doi: 10.1146/annurev.fluid.35.101101.161105.

[39] Chunming Li, Rui Huang, Zhaohua Ding, J. C. Gatenby, D. N. Metaxas, and J. C. Gore, "A Level Set Method for Image Segmentation in the Presence of Intensity Inhomogeneities With Application to MRI," *IEEE Trans. Image Process.*, vol. 20, no. 7, pp. 2007–2016, Jul. 2011, doi: 10.1109/TIP.2011.2146190.

[40] Chunming Li, Chenyang Xu, Changfeng Gui, and M. D. Fox, "Distance Regularized Level Set Evolution and Its Application to Image Segmentation," *IEEE Trans. Image Process.*, vol. 19, no. 12, pp. 3243–3254, Dec. 2010, doi: 10.1109/TIP.2010.2069690.

[41] K. Zhang, L. Zhang, K.-M. Lam, and D. Zhang, "A Level Set Approach to Image Segmentation With Intensity Inhomogeneity," *IEEE Trans. Cybern.*, vol. 46, no. 2, pp. 546–557, Feb. 2016, doi: 10.1109/TCYB.2015.2409119.

[42] Y. Hidaka, T. Sato, and H. Igarashi, "Topology optimization method based on on-off method and level set approach," *IEEE Trans. Magn.*, vol. 50, no. 2, pp. 617–620, 2014, doi: 10.1109/TMAG.2013.2285379.

[43] S. H. Heo, M. K. Baek, K. H. Lee, S. G. Hong, and I. H. Park, "Shape and topology optimization of rotor in synchronous reluctance motor using continuum sensitivity and adaptive level set method," *2013 Int. Conf. Electr. Mach. Syst. ICEMS 2013*, vol. 20, no. 3, pp. 129–133, 2013, doi: 10.1109/icems.2013.6754538.

[44] Young Sun Kim and Il Han Park, "Topology Optimization of Rotor in Synchronous Reluctance Motor Using Level Set Method and Shape Design Sensitivity," *IEEE*

Trans. Appl. Supercond., vol. 20, no. 3, pp. 1093–1096, Jun. 2010, doi: 10.1109/TASC.2010.2040725.

[45] J. S. Choi and J. Yoo, "Structural topology optimization of magnetic actuators using genetic algorithms and ON/OFF sensitivity," *IEEE Trans. Magn.*, vol. 45, no. 5, pp. 2276–2279, 2009, doi: 10.1109/TMAG.2009.2016297.

[46] C. D. Chapman, "STRUCTURAL TOPOLOGY OPTIMIZATION VIA THE GENETIC ALGORITHM," p. 190.

[47] C. D. Chapman, K. Saitou, and M. J. Jakiela, "Genetic algorithms as an approach to configuration and topology design," *J. Mech. Des. Trans. ASME*, vol. 116, no. 4, pp. 1005–1012, 1994, doi: 10.1115/1.2919480.

[48] M. Çunkaş and R. Akkaya, "Design optimization of induction motor by genetic algorithm and comparison with existing motor," *Math. Comput. Appl.*, vol. 11, no. 3, pp. 193–203, 2006, doi: 10.3390/mca11020193.

[49] C. H. Im, H. K. Jung, and Y. J. Kim, "Hybrid Genetic Algorithm for Electromagnetic Topology Optimization," *IEEE Trans. Magn.*, vol. 39, no. 5 I, pp. 2163–2169, 2003, doi: 10.1109/TMAG.2003.817094.

[50] T.-H. Lee, J.-H. Lee, K.-P. Yi, and D.-K. Lim, "Optimal Design of a Synchronous Reluctance Motor Using a Genetic Topology Algorithm," *Processes*, vol. 9, no. 10, p. 1778, Oct. 2021, doi: 10.3390/pr9101778.

[51] S. Ruzbehi and I. Hahn, "Two-level topology optimization of an electromagnetic actuator based on genetic algorithm and neighbourhood method," *Proc. IEEE Int. Conf. Ind. Technol.*, vol. 2020-Febru, pp. 230–233, 2020, doi: 10.1109/ICIT45562.2020.9067305.

[52] C. H. Im, H. K. Jung, and Y. J. Kim, "Hybrid Genetic Algorithm for Electromagnetic Topology Optimization," *IEEE Trans. Magn.*, vol. 39, no. 5 I, pp. 2163–2169, 2003, doi: 10.1109/TMAG.2003.817094.

[53] S. Xue and V. Acharya, "Topology optimization empowers the design of Interior Permanent Magnet (IPM) motors," *2020 IEEE Transp. Electrification Conf. Expo ITEC 2020*, no. c, 2020, doi: 10.1109/ITEC48692.2020.9161718.

[54] K. Watanabe, T. Suga, and S. Kitabatake, "Topology optimization based on the on/off method for synchronous motor," *IEEE Trans. Magn.*, vol. 54, no. 3, pp. 1–4, 2017.

[55] A. Deetman, "GCMMA-MMA-Python." Jul. 01, 2022. Accessed: Aug. 24, 2022. [Online]. Available: https://github.com/arjendeetman/GCMMA-MMA-Python

[56] M. Wall, "GAlib : A C ++ Library of Genetic Algorithm Components," *Statistics*, no. August, 1996.

[57] S. Bleuler, M. Laumanns, L. Thiele, and E. Zitzler, “PISA - A platform and programming language independent interface for search algorithms,” *Lect. Notes Comput. Sci. Subser. Lect. Notes Artif. Intell. Lect. Notes Bioinforma.*, vol. 2632, pp. 494–508, 2003, doi: 10.1007/3-540-36970-8_35.

[58] J. J. Durillo and A. J. Nebro, “JMetal: A Java framework for multi-objective optimization,” *Adv. Eng. Softw.*, vol. 42, no. 10, pp. 760–771, 2011, doi: 10.1016/j.advengsoft.2011.05.014.

[59] M. Lukasiewycz, M. Glaß, F. Reimann, and J. Teich, “Opt4J - A modular framework for meta-heuristic optimization,” *Genet. Evol. Comput. Conf. GECCO11*, pp. 1723–1730, 2011, doi: 10.1145/2001576.2001808.

[60] F. A. Fortin, F. M. De Rainville, M. A. Gardner, M. Parizeau, and C. Gagńe, “DEAP: Evolutionary algorithms made easy,” *J. Mach. Learn. Res.*, vol. 13, pp. 2171–2175, 2012.

[61] D. Izzo, “PyGMO and PyKEP: open source tools for massively parallel optimization in astrodynamics (the case of interplanetary trajectory optimization),” *Proceed Fifth Int. Conf Astrodyn. Tools Tech. ICATT*, 2012, [Online]. Available: https://scholar.google.com.br/citations?view_op=edit_citation&hl=en&citation_for_view=ykp4zwQAAAAJ:OU6Ihb5iCvQC&continue=/scholar%3Fhl%3Den%26as_sdt%3D0,5%26scilib%3D1%26scioq%3Dpygmo&citilm=1

[62] D. Hadka, “MOEA Framework, a Java library for multiobjective evolutionary algorithms.” http://moeaframework.org/ (accessed Nov. 16, 2020).

[63] A. Tonda, “Inspyred: Bio-inspired algorithms in Python,” *Genet. Program. Evolvable Mach.*, vol. 21, no. 1–2, pp. 269–272, 2020, doi: 10.1007/s10710-019-09367-z.

[64] Y. Tian, R. Cheng, X. Zhang, and Y. Jin, “PlatEMO: A MATLAB platform for evolutionary multi-objective optimization,” *IEEE Comput. Intell. Mag.*, vol. 12, no. 4, pp. 73–87, 2017.

[65] D. Hadka, “Platypus.” Dec. 2021. [Online]. Available: https://github.com/Project-Platypus/Platypus

[66] Y. Duan and D. M. Ionel, “A Review of Recent Developments in Electrical Machine Design Optimization Methods With a Permanent-Magnet Synchronous Motor Benchmark Study,” *IEEE Trans. Ind. Appl.*, vol. 49, no. 3, pp. 1268–1275, May 2013, doi: 10.1109/TIA.2013.2252597.

[67] K. Deb, A. Pratap, S. Agarwal, and T. Meyarivan, “A fast and elitist multiobjective genetic algorithm: NSGA-II,” *IEEE Trans. Evol. Comput.*, vol. 6, no. 2, pp. 182–197, 2002.

[68] M. Malinen and P. Råback, “Elmer finite element solver for multiphysics and multiscale problems,” vol. 19, 2013, pp. 101–113.

[69] M. E. R. M. S. Alnaes J. Blechta, J. Hake, A. Johansson, B. Kehlet, A. Logg, C. Richardson, J. Ring and G. N. Wells, “The FEniCS Project Version 1.5,” *Arch. Numer. Softw.*, vol. 3, 2015, doi: 10.11588/ans.2015.100.20553.

[70] P. Dular and C. Geuzaine, “GetDP reference manual: the documentation for GetDP, a general environment for the treatment of discrete problems.”

[71] F. Hecht, “New development in FreeFem++,” *J. Numer. Math.*, vol. 20, no. 3–4, pp. 251–265, 2012.

[72] “OpenFOAM | Free CFD Software | The OpenFOAM Foundation.” https://openfoam.org/ (accessed Aug. 24, 2022).

[73] D. Arndt *et al.*, “The \textttdeal.II Library, Version 9.4,” *J. Numer. Math.*, 2022, doi: 10.1515/jnma-2022-0054.

[74] “CalculiX: A Three-Dimensional Structural Finite Element Program.” http://www.dhondt.de/ (accessed Aug. 24, 2022).

[75] J.-M. Jin, *The Finite Element Method in Electromagnetics, 3rd Edition*. 2014. Accessed: Jul. 23, 2020. [Online]. Available: https://www.wiley.com/en-hk/The+Finite+Element+Method+in+Electromagnetics,+3rd+Edition-p-9781118571361

[76] “What Are Boundary Conditions? Numerics Background | SimScale.” https://www.simscale.com/docs/simwiki/numerics-background/what-are-boundary-conditions/ (accessed Aug. 24, 2022).

[77] J. Coulomb and G. Meunier, “Finite element implementation of virtual work principle for magnetic or electric force and torque computation,” *IEEE Trans. Magn.*, vol. 20, no. 5, pp. 1894–1896, Sep. 1984, doi: 10.1109/TMAG.1984.1063232.

[78] A. Khan, V. Ghorbanian, and D. Lowther, “Deep learning for magnetic field estimation,” *IEEE Trans. Magn.*, vol. 55, no. 6, pp. 1–4, 2019, doi: 10.1109/TMAG.2019.2899304.

[79] S. L. Brunton, M. Budišić, E. Kaiser, and J. N. Kutz, “Modern Koopman Theory for Dynamical Systems,” 2021.

[80] A. Essien and C. Giannetti, “A Deep Learning Model for Smart Manufacturing Using Convolutional LSTM Neural Network Autoencoders,” *IEEE Trans. Ind. Inform.*, vol. 16, no. 9, pp. 6069–6078, 2020, doi: 10.1109/TII.2020.2967556.

[81] B. Lusch, J. N. Kutz, and S. L. Brunton, “Deep learning for universal linear embeddings of nonlinear dynamics,” *Nat. Commun.*, vol. 9, no. 1, 2018, doi: 10.1038/s41467-018-07210-0.

[82] M. H. Mohammadi, V. Ghorbanian, and D. A. Lowther, “A Data-Driven Approach for Design Knowledge Extraction of Synchronous Reluctance Machines Using Multi-Physical Analysis,” *Proc. - 2018 23rd Int. Conf. Electr. Mach. ICEM 2018*, pp. 479–485, 2018, doi: 10.1109/ICELMACH.2018.8506851.

[83] D. Kochkov, J. A. Smith, A. Alieva, Q. Wang, M. P. Brenner, and S. Hoyer, “Machine learning – accelerated computational fluid dynamics,” 2021, doi: 10.1073/pnas.2101784118/-/DCSupplemental.y.

[84] S. Qi, Y. Wang, Y. Li, X. Wu, Q. Ren, and Y. Ren, “Two-Dimensional Electromagnetic Solver Based on Deep Learning Technique,” *IEEE J. Multiscale Multiphysics Comput. Tech.*, vol. 5, pp. 83–88, 2020, doi: 10.1109/JMMCT.2020.2995811.

[85] R. Gong and Z. Tang, “Training Sample Selection Strategy applied to CNN in Magneto-Thermal coupled Analysis,” *IEEE Trans. Magn.*, vol. 9464, no. c, pp. 8–11, 2021, doi: 10.1109/TMAG.2021.3058131.

[86] S. Pollok, R. Bjork, and P. S. Jorgensen, “Inverse Design of Magnetic Fields using Deep Learning,” *IEEE Trans. Magn.*, 2021, doi: 10.1109/TMAG.2021.3082431.

[87] S. Doi, H. Sasaki, and H. Igarashi, “Multi-objective topology optimization of rotating machines using deep learning,” *IEEE Trans. Magn.*, vol. 55, no. 6, pp. 1–5, 2019, doi: 10.1109/TMAG.2019.2899934.

[88] I. Goodfellow *et al.*, “Generative adversarial networks,” *Commun. ACM*, vol. 63, no. 11, pp. 139–144, Jun. 2020, doi: 10.1145/3422622.

[89] P. Isola, J. Y. Zhu, T. Zhou, and A. A. Efros, “Image-to-image translation with conditional adversarial networks,” *Proc. - 30th IEEE Conf. Comput. Vis. Pattern Recognit. CVPR 2017*, vol. 2017-Janua, pp. 5967–5976, 2017, doi: 10.1109/CVPR.2017.632.

[90] S. Arora, R. Ge, Y. Liang, T. Ma, and Y. Zhang, “Generalization and equilibrium in generative adversarial nets (GANs),” *34th Int. Conf. Mach. Learn. ICML 2017*, vol. 1, pp. 322–349, 2017.

[91] H. Sasaki and H. Igarashi, “Topology optimization of IPM motor with aid of deep learning,” *Int. J. Appl. Electromagn. Mech.*, vol. 59, no. 1, pp. 87–96, 2019, doi: 10.3233/JAE-171164.

[92] H. Sasaki and H. Igarashi, “Topology optimization accelerated by deep learning,” *IEEE Trans. Magn.*, vol. 55, no. 6, pp. 1–5, 2019, doi: 10.1109/TMAG.2019.2901906.

[93] J. Asanuma, S. Doi, and H. Igarashi, “Transfer Learning through Deep Learning: Application to Topology Optimization of Electric Motor,” *IEEE Trans. Magn.*, vol. 56, no. 3, pp. 18–21, 2020, doi: 10.1109/TMAG.2019.2956849.

[94] A. Khan, C. Midha, and D. Lowther, “Reinforcement Learning for Topology Optimization of a Synchronous Reluctance Motor,” *IEEE Trans. Magn.*, pp. 8–11, 2022, doi: 10.1109/TMAG.2022.3184246.

[95] S. Hanke, O. Wallscheid, and J. Böcker, “Data Set Description: Identifying the Physics Behind an Electric Motor -- Data-Driven Learning of the Electrical Behavior (Part I),” no. Part I, 2020.

[96] S. Hanke, O. Wallscheid, and J. Böcker, “Data Set Description: Identifying the Physics Behind an Electric Motor -- Data-Driven Learning of the Electrical Behavior (Part I),” no. Part II, 2020.

[97] W. Kirchgassner, O. Wallscheid, and J. Bocker, “Estimating Electric Motor Temperatures with Deep Residual Machine Learning,” *IEEE Trans. Power Electron.*, vol. 36, no. 7, pp. 7480–7488, 2021, doi: 10.1109/TPEL.2020.3045596.

[98] S. Mcgregor, D. Dhuri, A. Berea, and A. Muñoz-Jaramillo, “FlareNet: A Deep Learning Framework for Solar Phenomena Prediction,” no. Dlps, pp. 1–5, 2017.

[99] H. Jiang, Z. Nie, R. Yeo, A. B. Farimani, and L. B. Kara, “StressGAN: A generative deep learning model for two-dimensional stress distribution prediction,” *J. Appl. Mech. Trans. ASME*, vol. 88, no. 5, 2021, doi: 10.1115/1.4049805.

[100] Z. Ma, K. Xu, R. Song, C.-F. Wang, and X. Chen, “Learning-Based Fast Electromagnetic Scattering Solver Through Generative Adversarial Network,” *IEEE Trans. Antennas Propag.*, vol. 69, no. 4, pp. 2194–2208, 2020, doi: 10.1109/tap.2020.3026447.

[101] R. Gong and Z. Tang, “Investigation of convolutional neural network U-net under small datasets in transformer magneto-thermal coupled analysis,” *COMPEL - Int. J. Comput. Math. Electr. Electron. Eng.*, vol. 39, no. 4, pp. 959–970, 2020, doi: 10.1108/COMPEL-12-2019-0491.

[102] D. Jha *et al.*, “ResUNet++: An Advanced Architecture for Medical Image Segmentation,” *Proc. - 2019 IEEE Int. Symp. Multimed. ISM 2019*, pp. 225–230, 2019, doi: 10.1109/ISM46123.2019.00049.

[103] T. Weinkauf and H. Theisel, “Streak lines as tangent curves of a derived vector field,” *IEEE Trans. Vis. Comput. Graph.*, vol. 16, no. 6, pp. 1225–1234, 2010, doi: 10.1109/TVCG.2010.198.

[104] Gerris, “Free Computational Fluid Dynamics Reference,” vol. 2, no. 6, pp. 2–8.

[105] D. Kochkov, J. A. Smith, A. Alieva, Q. Wang, M. P. Brenner, and S. Hoyer, “Machine learning accelerated computational fluid dynamics,” pp. 1–13, 2021.

[106] S. Doi, H. Sasaki, and H. Igarashi, “Multi-objective topology optimization of rotating machines using deep learning,” *IEEE Trans. Magn.*, vol. 55, no. 6, pp. 1–5, 2019, doi: 10.1109/TMAG.2019.2899934.

[107] C. R. Harris *et al.*, “Array programming with NumPy,” *Nature*, vol. 585, no. 7825, Art. no. 7825, Sep. 2020, doi: 10.1038/s41586-020-2649-2.

[108] G. Remy, G. Krebs, A. Tounzi, and P. Barre, “Finite Element Analysis of a PMLSM (part 2) - Cogging force and end-effect force calculations -,” *Engineering*, no. part 2, pp. 2–5, 2007.

[109] G. Remy, G. Krebs, A. Tounzi, and P. Barre, “Finite Element Analysis of a PMLSM (part 1) - Meshing techniques and thrust computations -,” *Work*, vol. 0, no. part 1, pp. 2–5.

[110] J. Gomand, G. Remy, A. Tounzi, P. J. Barre, and J. P. Hautier, “Impact of permanent magnet field on inductance variation of a PMLSM,” *2007 Eur. Conf. Power Electron. Appl. EPE*, no. May 2014, 2007, doi: 10.1109/EPE.2007.4417589.

[111] G. Remy, G. Krebs, A. Tounzi, and P. J. Barre, “Detent force calculations of a PMLSM using the Finite Element method,” *IEEJ Trans. Ind. Appl.*, vol. 129, no. 5, 2009, doi: 10.1541/ieejias.129.462.

[112] H. Wu, S. Niu, Y. Zhang, X. Zhao, and W. Fu, “Fast Magnetic Field Approximation Method for Simulation of Coaxial Magnetic Gears using AI,” *IEEE J. Emerg. Sel. Top. Ind. Electron.*, pp. 1–9, 2022, doi: 10.1109/jestie.2022.3185558.

[113] A. N. Wignall, A. J. Gilbert, and S. J. Yang, “Calculation of forces on magnetised ferrous cores using the Maxwell stress method,” *IEEE Trans. Magn.*, vol. 24, no. 1, pp. 459–462, 1988, doi: 10.1109/20.43956.

[114] J. Bu, M. Zhou, X. Lan, and K. Lv, “Optimization for Airgap Flux Density Waveform of Flywheel Motor Using NSGA-2 and Kriging Model Based on MaxPro Design,” *IEEE Trans. Magn.*, vol. 53, no. 8, pp. 1–7, 2017, doi: 10.1109/TMAG.2017.2702758.

[115] G. Bramerdorfer and A.-C. Zăvoianu, “Surrogate-Based Multi-Objective Optimization of Electrical Machine Designs Facilitating Tolerance Analysis,”

IEEE Trans. Magn., vol. 53, no. 8, pp. 1–11, 2017, doi: 10.1109/TMAG.2017.2694802.

[116] Z. Q. Zhu and Y. Xiao, "Novel Magnetic-field-shifting Techniques in Asymmetric Rotor Pole Interior PM Machines with Enhanced Torque Density," *IEEE Trans. Magn.*, vol. 9464, no. 1, 2021, doi: 10.1109/TMAG.2021.3076418.

[117] R. Ni, D. Xu, G. Wang, L. Ding, G. Zhang, and L. Qu, "Maximum Efficiency Per Ampere Control of Permanent-Magnet Synchronous Machines," *IEEE Trans. Ind. Electron.*, vol. 62, no. 4, pp. 2135–2143, Apr. 2015, doi: 10.1109/TIE.2014.2354238.

[118] J. P. Cohoon and W. D. Paris, "Genetic Placement.," *IEEE Trans. Comput.-Aided Des. Integr. Circuits Syst.*, vol. 6, no. 6, pp. 956–964, 1987, doi: 10.1109/TCAD.1987.1270337.

[119] C. A. Anderson, K. F. Jones, and J. Ryan, "A two-dimensional genetic algorithm for the Ising problem," *Complex Syst.*, vol. 5, pp. 327–333, 1991.

[120] D. Fodorean, "State of the Art of Magnetic Gears, their Design, and Characteristics with Respect to EV Application," *Model. Simul. Electr. Veh. Appl.*, vol. 3, 2016, doi: 10.5772/64174.

[121] K. H. Shin, H. Il Park, H. W. Cho, and J. Y. Choi, "Parametric analysis and optimized torque characteristics of a coaxial magnetic gear based on the subdomain analytical model," *AIP Adv.*, vol. 7, no. 5, 2017, doi: 10.1063/1.4973798.

[122] A. Al-Qarni, F. Wu, and A. Ei-Refaie, "High-torque-density low-cost magnetic gear utilizing hybrid magnets and advanced materials," *2019 IEEE Int. Electr. Mach. Drives Conf. IEMDC 2019*, no. i, pp. 225–232, 2019, doi: 10.1109/IEMDC.2019.8785338.

[123] X. Zhao and S. Niu, "Design and Optimization of a New Magnetic-Geared Pole-Changing Hybrid Excitation Machine," *IEEE Trans. Ind. Electron.*, vol. 64, no. 12, pp. 9943–9952, 2017, doi: 10.1109/TIE.2017.2716879.

[124] N. W. Frank, S. Pakdelian, and H. A. Toliyat, "A magnetic gear with passive transient suppression capability," *2011 IEEE Electr. Ship Technol. Symp. ESTS 2011*, no. c, pp. 326–329, 2011, doi: 10.1109/ESTS.2011.5770891.

[125] N. W. Frank and H. A. Toliyat, "Gearing ratios of a magnetic gear for marine applications," *IEEE Electr. Ship Technol. Symp. ESTS 2009*, pp. 477–481, 2009, doi: 10.1109/ESTS.2009.4906554.

[126] J. J. Scheidler, V. M. Asnani, and T. F. Tallerico, "NASA's Magnetic Gearing Research for Electrified Aircraft Propulsion," *2018 AIAAIEEE Electr. Aircr. Technol. Symp. EATS 2018*, pp. 1–12, 2018, doi: 10.2514/6.2018-4988.

[127] H. Y. Wong, J. Z. Bird, D. Barnett, and W. Williams, “A high torque density halbach rotor coaxial magnetic gear,” *2019 IEEE Int. Electr. Mach. Drives Conf. IEMDC 2019*, pp. 233–239, 2019, doi: 10.1109/IEMDC.2019.8785188.

[128] X. Liu and H. Wang, “Analytical calculation and analysis of air gap magnetic field for electromechanical integrated toroidal drive,” *Adv. Mech. Eng.*, vol. 11, no. 12, pp. 1–13, 2019, doi: 10.1177/1687814019895925.

[129] T. Lubin, S. Mezani, and A. Rezzoug, “Analytical computation of the magnetic field distribution in a magnetic gear,” *IEEE Trans. Magn.*, vol. 46, no. 7, pp. 2611–2621, 2010, doi: 10.1109/TMAG.2010.2044187.

[130] Y. C. Wu and B. S. Jian, “Magnetic field analysis of a coaxial magnetic gear mechanism by two-dimensional equivalent magnetic circuit network method and finite-element method,” *Appl. Math. Model.*, vol. 39, no. 19, pp. 5746–5758, 2015, doi: 10.1016/j.apm.2014.11.058.

[131] X. Zhang, X. Liu, C. Wang, and Z. Chen, “Analysis and design optimization of a coaxial surface-mounted permanent-magnet magnetic gear,” *Energies*, vol. 7, no. 12, pp. 8535–8553, 2014, doi: 10.3390/en7128535.

[132] N. Misron, L. M. Saini, I. Aris, C. A. Vaithilingam, and H. Tsuyoshi, “Simplified design of magnetic gear by considering the maximum transmission torque line,” *Appl. Sci. Switz.*, vol. 10, no. 23, pp. 1–14, 2020, doi: 10.3390/app10238581.

[133] X. Yin, P. Pfister, and Y. Fang, “A novel magnetic gear: Towards a higher torque density,” *2015 IEEE Int. Magn. Conf. INTERMAG 2015*, no. 2013, p. 4095, 2015, doi: 10.1109/INTMAG.2015.7157676.

[134] K. Atallah and D. Howe, “A novel high-performance magnetic gear,” *IEEE Trans. Magn.*, vol. 37, no. 4 I, pp. 2844–2846, Jul. 2001, doi: 10.1109/20.951324.

[135] B. Praslicka, M. C. Gardner, M. Johnson, and H. A. Toliyat, “Review and Analysis of Coaxial Magnetic Gear Pole Pair Count Selection Effects,” *IEEE J. Emerg. Sel. Top. Power Electron.*, vol. 10, no. 2, pp. 1813–1822, 2021, doi: 10.1109/JESTPE.2021.3053544.

[136] K. He, X. Zhang, S. Ren, and J. Sun, “Deep residual learning for image recognition,” *Proc. IEEE Comput. Soc. Conf. Comput. Vis. Pattern Recognit.*, vol. 2016-Decem, pp. 770–778, 2016, doi: 10.1109/CVPR.2016.90.

[137] M. Abadi *et al.*, “TensorFlow: A system for large-scale machine learning,” 2016.

[138] M. Le, C. T. Pham, and J. Lee, “Deep neural network for simulation of magnetic flux leakage testing,” *Meas. J. Int. Meas. Confed.*, vol. 170, no. November, p. 108726, 2021, doi: 10.1016/j.measurement.2020.108726.

[139] Y. Li, G. Lei, G. Bramerdorfer, S. Peng, X. Sun, and J. Zhu, “Machine Learning for Design Optimization of Electromagnetic Devices: Recent Developments and Future Directions,” *Appl. Sci.*, vol. 11, no. 4, p. 1627, 2021, doi: 10.3390/app11041627.

[140] H. Wang, C. Zhang, Y. Yang, R. H. W. Liang, and S. Y. Hui, “A Comparative Study on Overall Efficiency of 2-Dimensional Wireless Power Transfer Systems Using Rotational and Directional Methods,” *IEEE Trans. Ind. Electron.*, 2021, doi: 10.1109/TIE.2020.3048317.

[141] H. Yang *et al.*, “A Novel Asymmetric-Magnetic-Pole Interior PM Machine with Magnet-Axis-Shifting Effect,” *IEEE Trans. Ind. Appl.*, vol. 57, no. 6, pp. 5927–5938, 2021, doi: 10.1109/TIA.2021.3111153.

[142] J. Pan *et al.*, “Physics-Based generative adversarial models for image restoration and beyond,” *arXiv*, no. 1, pp. 1–14, 2018, doi: 10.1109/tpami.2020.2969348.

[143] A. Horé and D. Ziou, “Image quality metrics: PSNR vs. SSIM,” *Proc. - Int. Conf. Pattern Recognit.*, pp. 2366–2369, 2010, doi: 10.1109/ICPR.2010.579.

[144] S. Pollok, N. Olden-Jørgensen, P. S. Jørgensen, and R. Bjørk, “Magnetic Field Prediction Using Generative Adversarial Networks,” pp. 1–10, 2022.